AN ABSTRACT OF THE THESIS OF

Anasuya Erin Krishnaswamy for the degree of Doctor of Philosophy in Electrical and Computer Engineering presented on March 15, 1999.

Title: Nonequilibrium Electron Transport in Quantum Dot and Quantum Point Contact Systems .

Redacted for Privacy

Abstract approved:

Stephen M. Goodnick

Much experimental research has been performed in the equilibrium regime on individual quantum dots and quantum point contacts (QPCs). The focus of the research presented here is electron transport in the nonequilibrium regime in coupled quantum dot and QPC systems fabricated on AlGaAs/GaAs material using the split gate technique.

Near equilibrium magnetoconductance measurements were performed on a quantum dot and a QPC. Oscillations were seen in the conductance of the sensor which corresponded to Aharonov-Bohm oscillations in the quantum dot, to our knowledge the first such observation. Sudden jumps in the conductance of the QPC were observed under certain gate biases and under certain magnetic fields. When the gate biases and magnetic field were held constant and the conductance was observed over time, switching was observed with the form of a random telegraph signal (RTS). RTS switching is usually attributed to charging of a single impurity. However, in this case switching may have been due to tunneling via edge states in the dot.

Nonequilibrium transport in single quantum dots was investigated. A knee or kink was observed in the current-voltage characteristics of two dots on different

material. The bias conditions under which the knee occurred point to electron heating as the physical mechanism for the observed behavior. However, the data can not be fit accurately over all bias ranges with an energy balance hot electron model. Modifications to the model are needed to accurately represent the devices studied here.

Finally, the effect of nonlinear transport through a one dimensional (1D) QPC on the equilibrium conductance of an adjacent 0D quantum dot was explored. This was the first attempt to observe Coulomb drag between a 0D and 1D system. It was observed that the equilibrium conductance peaks in the quantum dot were broadened as the current in the QPC increased. This apparent electron heating effect in the dot can be explained by a simple ballistic phonon model. However, reasonable phase coherence times can be estimated from peak fitting using a Breit-Wigner formula which points to a Coulomb interaction. More detailed numerical calculations should illuminate the dominant scattering processes.

Nonequilibrium Electron Transport in Quantum Dot and Quantum Point Contact Systems

by

Anasuya Erin Krishnaswamy

A THESIS

submitted to

Oregon State University

in partial fulfillment of
the requirements for the
degree of

Doctor of Philosophy

Completed March 15, 1999
Commencement June 1999

Doctor of Philosophy thesis of Anasuya Erin Krishnaswamy presented on March 15, 1999

APPROVED:

Redacted for Privacy

Major Professor, representing Electrical and Computer Engineering

Redacted for Privacy

Chair of the Department of Electrical and Computer Engineering

Redacted for Privacy

Dean of the Graduate School

I understand that my thesis will become part of the permanent collection of Oregon State University libraries. My signature below authorizes release of my thesis to any reader upon request.

Redacted for Privacy

Anasuya Erin Krishnaswamy, Author

ACKNOWLEDGMENT

There is no way to adequately thank my loved ones for all their support during this process. Thanks, Sheila and Narendra Krishnaswamy (Mom and Dad). Thanks, Tom Cooney. Thanks to Robyn Mutobe, Kate Remley, Laura Clarke, Ann Brown and Anita Stelling.

I would not have been able to complete this research without learning from other students and post docs. Thank you to Chris Berven, Kris Johnson, Jolinda Smith, Laura Clarke, Ramasubramaniam Rajagopal, and David Pivin. Special thanks to kindred spirits in Arizona who also would have rather been in Oregon, Manfred Dür and Allen Gunther. Thanks to Nathan Harff for meaningful discussions and swapping stories about Steve.

I greatly appreciated and found invaluable the support and encouragement of my advisor, Steve Goodnick, and the additional guidance and advice of one of my committee members, Martin Wybourne.

Thank you to Jerry Simmons at Sandia National Laboratories for providing the material and optical lithography and to Jon Bird for allowing me the use of his dilution refrigerator system. This research was in large part funded by a grant from the Office of Naval Research.

TABLE OF CONTENTS

TABLE OF CONTENTS (Continued)

TABLE OF CONTENTS (Continued)

TABLE OF CONTENTS (Continued)

LIST OF FIGURES

LIST OF FIGURES (Continued)

LIST OF FIGURES (Continued)

LIST OF FIGURES (Continued)

LIST OF FIGURES (Continued)

LIST OF TABLES

NONEQUILIBRIUM ELECTRON TRANSPORT IN QUANTUM DOT AND QUANTUM POINT CONTACT SYSTEMS

1. INTRODUCTION

The trend over the last three decades in the electronics industry has been a reduction in the size of devices in order to make faster chips in a smaller area and at a reduced cost. As the electronics industry continues to reduce the minimum feature size of the devices under its current technology, it is approaching physical limits which will require new methods of device fabrication and modeling that takes into account the nature of matter on the mesoscopic scale (less than a micron but larger than an atom). It is at this crossroads that the interests of the scientific community in understanding fundamentals about electron transport in solid state materials and the interests of the industrial community meet. The study of quantum devices is necessary in order to lay the ground work for the implementation of future technology. In addition, it provides the solid state research scientist with rich transport phenomena to explore.

The fabrication of memory, switches, and low power amplifiers in silicon is dominated by the industry standard metal oxide semiconductor (MOS) device illustrated in Fig. 1.1 or complementary metal oxide semiconductor (CMOS) inverter [1]. In order to shrink these devices, the channel length, L_{eff}, in Fig. 1.1 must be made shorter, the source and drain junctions shallower, and the oxides thinner. As these components are reduced, physical phenomena appear which severely alter the device behavior. For instance, when the channel length is reduced, the electric field across the channel increases creating high energy carriers, or hot electrons (hot e^- in Fig. 1.1), which bombard the oxide. Some of these carriers remain in the oxide and permanently alter the threshold voltage (the gate voltage required to turn on

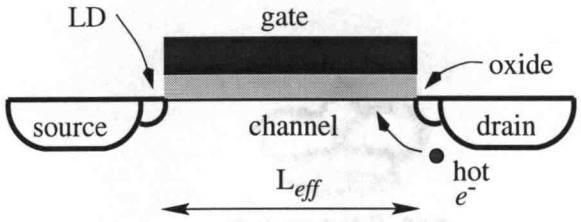

Figure 1.1: Cross section of an MOS device

the device) shown in Fig. 1.2. In this case a device that is designed to be turned off, might turn on. Lightly doping at the corners of the source and drain (LD in Fig. 1.1) reduces the electric field strength and thus the leakage current, but increases the complexity of the processing and difficulty of scaling the process.

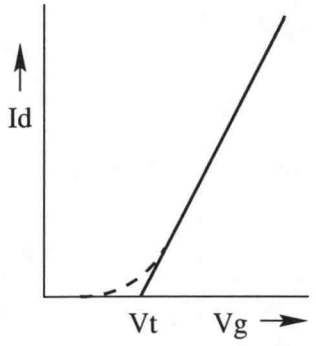

Figure 1.2: Source/drain current as a function of the gate voltage with the threshold voltage, Vt, shown

Some of the short channel effects can be reduced by making the oxides thinner. This also reduces the threshold voltage which is an advantage for low power operations. However, thinner oxides lead to an increased leakage current due to tunneling and therefore less control over the device turn on. In addition the thinner the oxide, the greater the chance of dielectric breakdown which renders the device

completely inoperable [2].

A smaller but important portion of the semiconductor industry is devoted to ICs and optical devices in GaAs systems. The modulation doped field effect transistor (MODFET) and metal semiconductor transistor (MESFET) are common transistors used in high speed circuit operation. The MODFET is fabricated on a heterostructure such as AlGaAs/GaAs (discussed in Chapter 2) and is the predecessor to the devices studied in this research. While problems with thinner oxides are avoided in MODFET systems, short channel effects are present and cause the I-V characteristics to deviate from the desired behavior [3].

There are many device physics issues and remedies related to shrinking electronic devices [1], and only a small sampling has been given here. The semiconductor industry invests great effort into finding fabrication techniques to avert these problems and employs to a large degree classical physics to model these phenomena. The semiclassical Boltzmann Transport Equation (BTE) and simplifications such as the drift-diffusion equation are currently used to model electron transport. Assuming that fabrication technology continues to allow the scaling of feature sizes to nanometer dimensions, there is a limit at which these modeling techniques will breakdown, and a new paradigm in device technology will inevitably emerge. This limit will be reached when device dimensions approach certain length scales.

Before describing these length scales, it is helpful to briefly review the assumptions inherent in the BTE [4]–[6]. First, the system is assumed to be in the form of a dilute gas: a large enough number of particles to use statistical methods but a small enough density that particle interaction is minimal. Scattering processes are considered to be weak, non-interacting, and localized in space and time. This implies that the time between collisions is much greater than the duration of a collision, and the mean de Broglie wavelength of the particle is small compared to the mean separation between scatterers. Consequently the behavior can be described by a wave

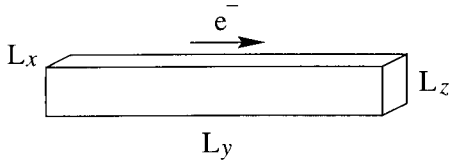

Figure 1.3: Conductor of width, L_x, length, L_y, and height, L_z

packet which follows a classical particle trajectory between collisions. In addition, the probability of a collision is considered to be independent of past history; i.e., a collision is a random, uncorrelated event, and no phase memory is preserved. As devices are scaled to nanometer proportions, some or all of these assumptions may be violated.

In the conductor shown in Fig. 1.3, when the width, L_x, height, L_z, or the length, L_y, approach the Fermi wavelength, $\lambda_f = 2\pi/k_f$, of an electron, the energy and momentum in that direction are quantized. When the length, L_y, is less than the scattering length of an electron, the electron motion will be ballistic. When L_y is less than the phase coherence length of an electron, the electron motion will be coherent [7]. If the Fermi wavelength is on the order of the device dimensions, one can no longer treat the electron as a wave packet localized in space and following a classical particle trajectory between collisions. And if the phase coherence length is on the order of the device dimensions and electron motion is coherent, a collision can no longer be considered as a random, uncorrelated event.

Furthermore, when L_z, L_x, or L_y are reduced, the capacitance of the system is reduced, and the charging energy of one electron, e^2/C, where C is the capacitance of the system, increases. When the charging energy becomes larger than the thermal energy and larger than any noise generated in the system, single electron charging may be observed and charge granularity becomes important. In these few particle systems the meaning of a momentum and position distribution function is blurred.

In general, a reduction of any one of the above parameters, L_z, L_x, or L_y, below the corresponding length scale leads to a reduction in the dimensionality of the device, and into the realm of quantum devices.

Quantum devices may roughly be grouped into two large categories: electronic devices and optoelectronic devices. For a brief overview of the area of quantum optical devices, see reference [8]. Quantum electronic devices can be further subdivided into two categories. *Quantum wave* devices make use of the wave nature of the electron and include electron interferometers [8] and electron wave interference filters [9]. In addition quantum computing has been proposed and quantum bits or q-bits are being implemented. For a recent experiment see [10]. *Single electron* devices take advantage of the granular nature of the electronic charge and include quantum dots [11]–[13], cellular automata devices [14, 15], and devices related to the capacitance standard [16]. The devices mentioned above operate under near equilibrium bias conditions, however devices have been demonstrated which operate under large bias, far from equilibrium conditions. Examples are the lateral hot electron device [17, 18] and the lateral hot electron transistor (LHET) [19]. As the fundamental limit of current fabrication and modeling techniques is approached, researchers are studying these quantum devices to characterize their behavior, and in the future it may be applied to the electronics industry in a creative and useful way.

In the first part of Chapter 2, the physics of low dimensional systems will be discussed. The extensive work that has already been done in the near equilibrium regime on semiconductor quantum dots is reviewed at the end of Chapter 2. Chapter 3 provides an overview of the fabrication and experimental techniques used to create these semiconductor quantum dots and investigate their transport properties. In addition, a brief review of alternative fabrication techniques is given.

The main focus of this work is the study of nonequilibrium transport in AlGaAs/GaAs quantum dot devices. However, in order to characterize nonequilib-

rium effects, the equilibrium behavior must be first be characterized. Chapter 4 discusses equilibrium measurements performed on single quantum dots and on a coupled quantum dot and quantum point contact system. Novel magneto-transport measurements are presented using a noninvasive probe which showed switching behavior. The far from equilibrium transport characteristics of single quantum dots with and without a perpendicular magnetic field was investigated and is the subject of Chapter 5. In addition, the noninvasive voltage probe design was employed to determine the interaction between nonequilibrium current flow through a one dimensional (1D) channel and the equilibrium characteristics of a zero dimensional (0D) quantum dot. Finally, conclusions and proposals for future work are presented in Chapter 6.

2. PHYSICS AND TRANSPORT OF LOW DIMENSIONAL SYSTEMS

This chapter is an overview of some of the physics of low dimensional systems needed to understand the theory of electron transport through nanostructures. Transport through a quantum dot and quantum point contact (QPC) will be discussed including 1D conductance steps and single electron charging phenomena.

2.1 Physics in Two Dimensions

In order to create a quantum box, or dot, of electrons one must be able to confine the electrons in three dimensions. One can begin by creating a two dimensional (2D) sheet of electrons. The emergence of the fabrication of ultra thin semiconductor structures which began roughly 25 years ago has allowed for the fairly routine production of physically real 2D systems in various semiconductor materials. For instance, by growing a heterostructure semiconductor material such as GaAs/$Al_xGa_{1-x}As$, where x is the mole fraction of Al, electron confinement in the growth direction can be achieved as shown in Fig. 2.1.

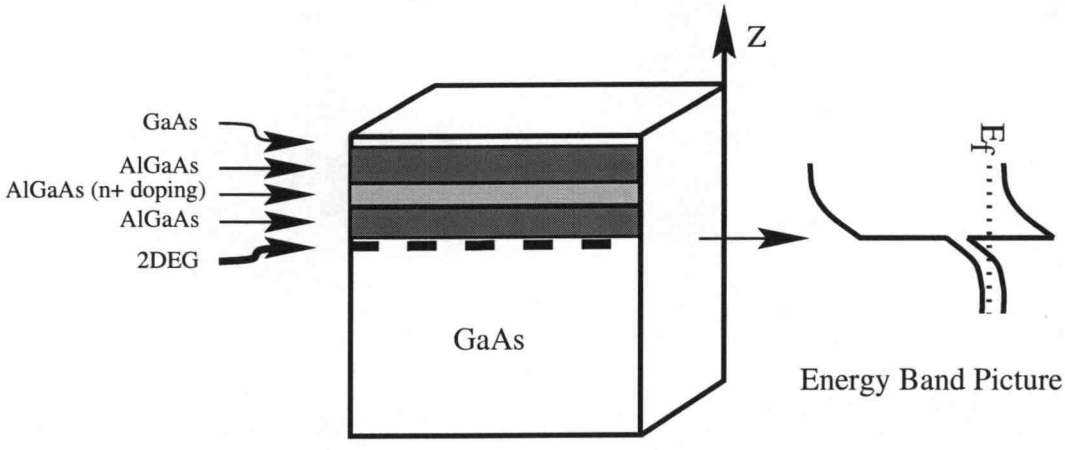

Figure 2.1: Crossection of GaAs/AlGaAs heterostructure material with corresponding energy band diagram.

The difference in the energy band gaps between the two materials produces a potential well at the interface and dopants such as Si provide a source for a two dimensional sheet of electrons or two dimensional electron gas (2DEG) to form at the interface. If a spacer layer is introduced between the dopant and the interface, ionized impurity scattering due to the dopants is greatly reduced and the mobility of the electrons increases as well as the likelihood of observing quantum effects. This technique is known as modulation doping [8].

A structure with a thicker spacer layer results in a higher electron mobility but a lower electron density. A higher density of carriers will help to screen out inhomogeneities in the background potential which also helps in observing quantum effects, but at very high densities carriers begin to be transferred into the AlGaAs layer reducing the mobility. Thus the thickness of the spacer layer must be chosen to accommodate the optimum combination of electron mobility and density.

High mobility heterostructure material can be fabricated using many different growth methods, but the most preferred are metal organic chemical vapor deposition (MOCVD) and molecular beam epitaxy (MBE). Both techniques can produce high mobility material with an abrupt interface which enhances confinement. However, the highest mobility material has been grown using MBE (10,000,000 cm^2/Vs in MBE [20, 21] compared to 1,000,000 cm^2/Vs in MOCVD [22]). Typically the mole fraction of Al, x, is 0.3. As the mole fraction is increased, the difference in band gaps increases, resulting in better confinement of the electrons. However, deep level defects in the $Al_xGa_{1-x}As$ layer known as DX centers (discussed in Appendix 1) also increase, and above $x = 0.3$ they present undesirable effects. The value of $x = 0.3$ is an optimum value which allows for increased confinement while keeping lattice defects at a tolerable level.

In a 2DEG electron motion is confined in the z-direction but not in the x-y plane where the electrons can be treated as plane waves. For electrons close

to the conduction band minimum the Schrödinger equation in the effective mass approximation [23] may be written,

$$\left[\frac{-\hbar^2}{2m^*}\left(\frac{\partial^2}{\partial x^2}+\frac{\partial^2}{\partial y^2}+\frac{\partial^2}{\partial z^2}\right)+V(z)\right]\Psi(z)=E_n\Psi(z). \tag{2.1}$$

The wave function can be separated into two parts, the free electron part and the wave function in the z direction, $\zeta(z)$,

$$\Psi(x,y,z)=\frac{1}{\sqrt{L_yL_x}}\zeta(z)e^{ik_yy}e^{ik_xx}. \tag{2.2}$$

By substituting Eq. 2.1 into the Schrödinger equation and separating, the problem is reduced to solving the Schrödinger equation in the z direction.

$$\left[\frac{-\hbar^2}{2m*}\left(\frac{\partial^2}{\partial z^2}\right)+V(z)\right]\zeta(z)=E_n\zeta(z), \tag{2.3}$$

where $V(z)$ is the potential due to the conduction band discontinuity at the interface between the GaAs and AlGaAs layers and as well as band bending due to ionized impurities and free electrons. The potential must obey Poisson's equation,

$$\frac{d^2}{dz^2}V_H(z)=\frac{-\rho(z)}{\varepsilon}, \tag{2.4}$$

where $V_H(z)$ is the potential due to electron-electron interactions and ionized impurities. $\rho(z)$ is the charge density and equal the electron charge times the magnitude squared of wave function obtained from the Schrödinger equation

$$\rho(z)=e|\ \Psi(z)\ |^2 \tag{2.5}$$

Thus both the Schrödinger and Poisson equation must be solved simultaneously to render the correct energy band profile. This is done numerically using an iterative technique.

The potential profile is often approximated as a triangular well, $V=eFz$, where e is the electron charge, F is a constant, and z is the distance from the

interface in the growth direction. Solutions to Eq. 2.1 are in the form of Airy functions with approximate energy levels in the z direction given by [8],

$$E_n \cong \left(\frac{\hbar^2}{2m*}\right)^{\frac{1}{3}} \left(\frac{3\pi eF}{2}\left(n+\frac{3}{4}\right)\right)^{\frac{2}{3}} \tag{2.6}$$

where $n = 0, 1....$ The complete expression for the energy takes the form

$$E = E_n + \frac{\hbar^2({k_x}^2 + {k_y}^2)}{2m*}, \tag{2.7}$$

where k_x and k_y are the free electron wave vectors in the plane of the 2DEG and the energies E_n are the bottom of 2D subbands. Electron transport is not only dependent on the available energy levels of the system but the density of the energy states. The expression for the 2D density of states for a given energy is [8]

$$\rho_{2D} = \sum_{n=0}^{\infty} \Theta(E_0 - E_n)\frac{m^*}{\pi\hbar^2}, \tag{2.8}$$

where $\Theta(E_0 - E_n)$ is a step function, n is the number of subbands below the given energy. The above expression tells us that in the ground state the density of states is finite and does not tend toward zero as in the expression for the 3D density of states

$$\rho_{3D} = \frac{2^{\frac{1}{2}}{m^*}^{\frac{3}{2}}}{\pi^2\hbar^3}E^{\frac{1}{2}}. \tag{2.9}$$

Electron transport is dependent on various scattering mechanisms which in turn are dependent on the density of states. Thus, electron transport in 2D systems at low temperatures and low electron density varies significantly from that in 3D systems. In addition to the quantization of energy levels in the growth direction, a significant feature of 2D systems which is relevant to the devices studied in this research is the high mobility of the electrons mentioned previously. The combination of modulation doping, and a step like density of states at low electron density and at low temperatures serves to decrease the probability of electron scattering and therefore increase the mobility. In addition, relaxation of hot electrons which may

be generated under high field conditions will be dependent on 2D electronic features. For a complete review of the physics of electron transport in 2D systems see [24] or for a brief overview see Chapter 4 of [8].

2.2 Physics in One Dimension

Once a 2DEG is formed, the gas can be "squeezed" further into a 1D channel or wire by various methods. For instance, in AlGaAs/GaAs Thornton *et al.* used the split gate technique (discussed in Chapter 3) to create long tunable 1D wires [25], and H. van Houten *et al.* used a shallow mesa etch to create narrow 1D channels [26]. For a summary of fabrication methods of 1D wires see Ref. [27].

2.2.1 Solution to the Schrödinger equation

The Schrödinger equation in the effective mass approximation for a 1D line is

$$\left[\frac{-\hbar^2}{2m*}\left(\frac{\partial^2}{\partial x^2}+\frac{\partial^2}{\partial y^2}+\frac{\partial^2}{\partial z^2}\right)+V(x,z)\right]\Psi(x,y,z)=E\Psi(x,y,z). \tag{2.10}$$

The potential is now a function of x and z, and the wave function can be separated into a function of x and z and a plane wave in the y direction,

$$\Psi(x,y,z)=\frac{1}{\sqrt{L_y}}\zeta(x,z)e^{ik_y y}, \tag{2.11}$$

where

$$\left(\frac{{p_x}^2+{p_z}^2}{2m*}+V(x,z)\right)\zeta_n(x,z)=E_n\zeta_n(x,z). \tag{2.12}$$

The expression for the energy is

$$E=E_n+\frac{\hbar^2{k_y}^2}{2m*}. \tag{2.13}$$

Energy quantization occurs in the x and z directions, but not in the y direction which means that there will be 1D subbands in the conductor. The energy at the bottom edges of the 1D subbands will be determined by the shape of the confining potential.

2.2.2 Equilibrium Transport in a Quantum Point Contact

The split gate technique can also be used to define short narrow constrictions called quantum point contacts (QPCs) through which an electron may pass without undergoing any collisions. The 1D physics described above can be applied to these structures, and if the 1D conductor is connected to 2D electron reservoirs at each end, the transport of electrons through the QPC can be investigated.

A semiclassical approach to the transport through the 1D conductor gives us an expression for the current due to one subband [7],

$$I = qn\nu = e\nu_n\rho_n\delta E, \tag{2.14}$$

where ν_n is the group velocity, ρ_n is the density of states, and $\delta E/e$ is the incremental voltage bias across the channel. Near equilibrium conditions are met when the voltage bias across the QPC is smaller than the spacing between energy subbands and large enough to detect a small current. Looking at the expressions for the group velocity and the density of states in 1D

$$\nu_n = \frac{dE_n(k)}{\hbar dk},\ \rho_n = \sum_n n\Theta(E_0 - E_n)(\frac{\pi dE_n(k)}{dk})^{-1}, \tag{2.15}$$

we can see that the derivative of the energy with respect to the wave vector, k, cancels out in the current equation. Therefore we are left with the expression

$$I = (\frac{2e}{h})N\delta E, \tag{2.16}$$

where N is the number of subbands in the channel. Converting to conductance we obtain

$$G = \frac{2e^2}{h}N. \tag{2.17}$$

This means that the conductance will be quantized in the fundamental units of e^2/h.

A completely quantum mechanical approach considers the transmission probability amplitudes from one reservoir to another. In this Landauer-Büttiker formalism

the potential barrier is considered to be a scatterer through which current is forced. In the multichannel (subband) case the expression for the conductance is [28]

$$G = \frac{2e^2}{h} N \sum_{n,m=1} |t_{nm}|^2, \tag{2.18}$$

Where n and m are the subbands in the left and right reservoirs respectively and t_{nm} is the transmission coefficient from subband n to subband m. It is equivalent to the semiclassical equation (2.17) if there is no intersubband scattering or if any intersubband scattering that occurs results in the electrons being transmitted to the exit reservoir rather than reflected back to the entry reservoir. The transmission coefficient, t_{nm}, is determined by the shape of the lateral confining potential profile in the quantum point contact. This confining potential is often assumed to be a hard wall or a saddle point potential, but is probably somewhere in between. As the gate voltage is increased negatively, the number of subbands available for transport decreases in integer steps. If the conductance is plotted as a function of gate voltage applied to the QPC under near equilibrium conditions, a step like structure is predicted. A schematic of the behavior at T=0 K is shown in Fig. 2.2. This phenomena was first seen experimentally by Van Wees *et al.* [29] and Wharam *et al.* [30] in 1988.

2.3 0D Physics and Single Electron Phenomena

The split gate technique can also be used to confine electrons into a 0D structure or quantum dot. In a quantum dot electrons are confined in three dimensions. The density of states of the dot are discrete and determined by the shape of the confining potential V(x,y,z). The energy levels can be obtained analytically for a 3D infinite potential well or harmonic oscillator, but for the structures considered here, and in general, must be solved numerically.

A central phenomena in the near equilibrium transport characteristics of quan-

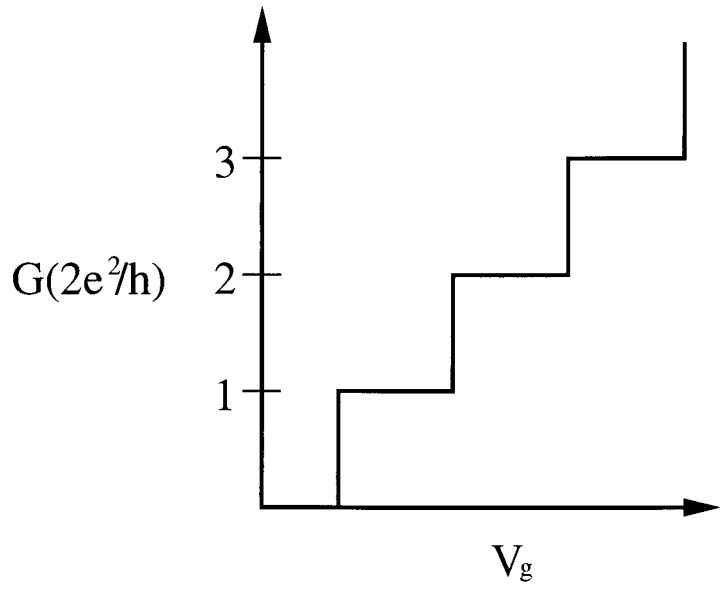

Figure 2.2: Equilibrium conductance steps in an ideal quantum point contact at T=0K.

tum dots is the Coulomb blockade effect. Coulomb blockade can be explained semi-classically. For a complete quantum mechanical description see [31, 32, 6]. In a classical, lumped capacitance model, the electrostatic energy stored or work done in building up charge Q on a capacitor, with capacitance C, is

$$E_s = \frac{Q^2}{2C}. \tag{2.19}$$

A simple model for the quantum dot is a disk above a conducting plane shown in Fig. 2.3. The capacitance is given as a problem in the classical electrodynamics book by Jackson [33], is solved in the book on electricity by Smythe [34], and is given by,

$$C = 8\epsilon R, \tag{2.20}$$

where ϵ is the permittivity of the material (GaAs in this case) and R is the radius of the disk. This approximation is for the distance from the disk to the plane larger than the disk radius, $d \gg R$. While this is not the most accurate capacitance estimate, it is useful for experimental purposes and back of the envelope calculations.

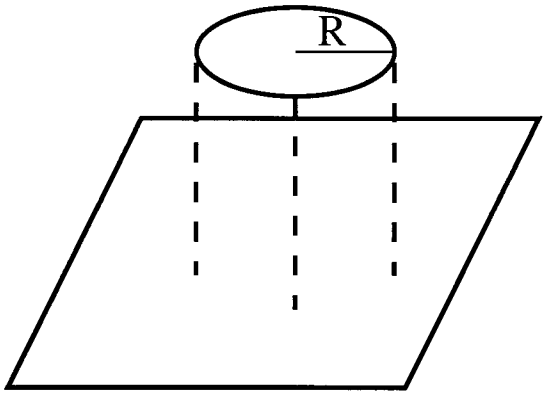

Figure 2.3: A metallic disk above a conducting plane.

Thus the energy needed to add one electron to the quantum dot is

$$E_s = \frac{e^2}{2(8\epsilon R)}. \tag{2.21}$$

For a very small dot with a charging energy,

$$\frac{e^2}{2C} \gg kT_{room}, \tag{2.22}$$

single electron effects may be seen at room temperature. At room temperature

$$kT_{room} = 25\ meV = \frac{e^2}{2C} \tag{2.23}$$

$$C = 3 \times 10^{-18} F = 8\epsilon R, \tag{2.24}$$

which implies the size of the dot should be R_{dot} =3 nm to see room temperature effects. This small size is not attainable with available fabrication techniques and equipment used in this research, and the minimum dot radius achieved in the present work was approximately 200 nm. This yields a charging energy of 430 μeV which corresponds to the thermal energy at T=5 K. Therefore, in order to observe single electron charging in these dots, the temperature of the system has to be reduced well below 5 K.

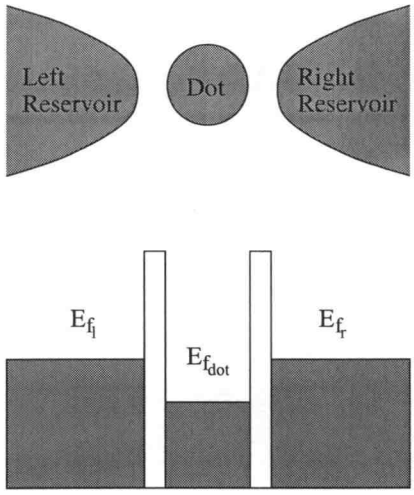

Figure 2.4: Schematic of the a dot weakly coupled to electron reservoirs and corresponding energy band diagram.

2.3.1 Coulomb Staircase

To understand how single electron charging may be observed it is helpful to look at a picture of the 2DEG depicting a puddle of electrons isolated from the 2DEG by tunnel barriers, and to look at the corresponding energy diagram under equilibrium conditions shown in Fig. 2.4. The energy diagram represents a metallic dot (continuum of states below the Fermi energy) for illustrative purposes. In a semiconductor the states below the Fermi energy would be discrete, however the metallic system is somewhat simpler than a semiconductor system and can model the semiconductor system if the energy level spacing of the semiconductor dot is much smaller than the charging energy, $\Delta E \ll e^2/C$.

A circuit model of this system is shown in Fig. 2.5 with double boxes representing a tunnel junction and a small bias voltage applied across the device. A lumped capacitance and tunnel resistance is associated with the tunnel junction barriers. Although the tunnel junction symbol is commonly used in the literature, the double box may also be represented by a capacitance and voltage controlled current source in parallel for circuit simulation purposes. The number of electrons

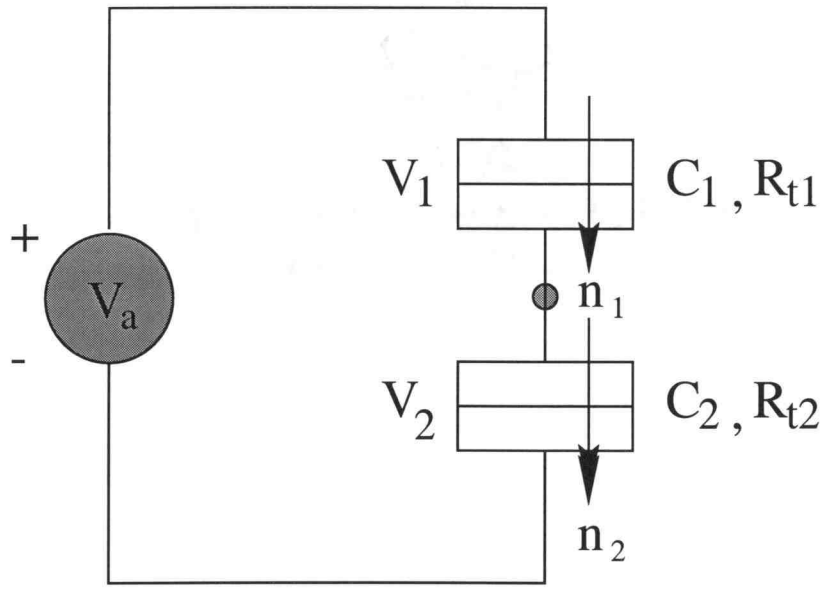

Figure 2.5: Circuit diagram of a quantum dot with a small applied bias.

that tunnel into and out of the dot are n_1 and n_2, respectively. The energy of the system is the electrostatic energy stored in the capacitors plus the work done by the voltage source to tunnel electrons in and out of the island [6].

$$E_{system} = E_s - W_s = \frac{1}{2C_{eq}}\left(C_1 C_2 {V_a}^2 + Q^2\right) - \frac{eV}{C_{eq}}\left(C_1 n_2 + C_2 n_1\right) \tag{2.25}$$

where $Q = -e(n_1 - n_2)$ is the net charge on the island and $C_{eq} = C_1 + C_2$. If an electron tunnels out of or into the dot,

$$n_2 = n_2 \pm 1 \tag{2.26}$$

$$n_1 = n_1 \pm 1. \tag{2.27}$$

The change in the energy of the system due to the movement of a single electron can then be calculated by substituting Eq. 4.27 into the expression for the energy of the system and subtracting the initial energy. The change in energy to accommodate an electron tunneling through junction two is given by

$$\Delta {E_2}^{\pm} = E\left(n_1, n_2\right) - E\left(n_1, n_2 \pm 1\right) \tag{2.28}$$

$$\Delta E_2{}^{\pm} = \frac{e}{C_{eq}}\left[\frac{-e}{2} \mp (en - V_a C_1)\right] \tag{2.29}$$

And, similarly, the energy to accommodate an electron tunneling through junction one is given by

$$\Delta E_1 = \frac{e}{C_{eq}}\left[\frac{-e}{2} \pm (en + V_a C_2)\right] \tag{2.30}$$

If n=0, that is initially no electrons have tunneled into the dot, then the requirement for a nonnegative change in energy is

$$\Delta E_{1,2}{}^{\pm} = \frac{-e^2}{2C_{eq}} \pm \frac{eV_a C_{2,1}}{C_{eq}} \geq 0. \tag{2.31}$$

And the applied voltage required is

$$\mid V_a \mid \geq \frac{e}{C_{eq}}. \tag{2.32}$$

In Fig. 2.6 the Coulomb gap is shown in the energy band diagrams under no applied bias and a small applied bias. When a bias greater than e/C_{eq} is applied, an electron can tunnel into the dot. If the tunneling resistance $R_{t1} \gg R_{t2}$, tunneling is limited by junction one and as soon as the electron tunnels out of the dot via junction one, another electron will tunnel into the dot via junction two. If $n = 1$ in the energy expression of equation 2.31,

$$\Delta E = \frac{-e^2}{2C_{eq}} - \frac{e^2}{C_{eq}} + \frac{eV_a C_1}{C_{eq}} \geq 0, \tag{2.33}$$

the voltage required for a nonnegative change in energy is

$$V_a \geq \frac{3e}{2C_1} = \frac{3e}{C_{eq}}. \tag{2.34}$$

Therefore, when V_a is between e/C_{eq} and $3e/C_{eq}$ no more than one electron can tunnel into the dot at a time. When the voltage is increased past $3e/C_{eq}$, two electrons can tunnel into the dot, and so on. A schematic of the predicted current versus applied voltage is shown in Fig. 2.7. This phenomena is known as the Coulomb staircase and the relevant capacitance in this bias configuration is the

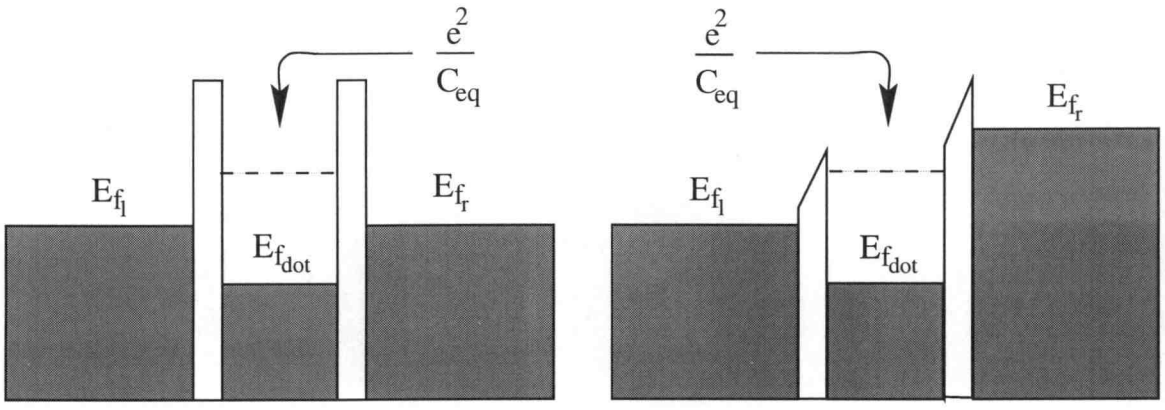

Figure 2.6: Energy band diagrams of (a) Coulomb blockade and (b) Tunneling through the dot.

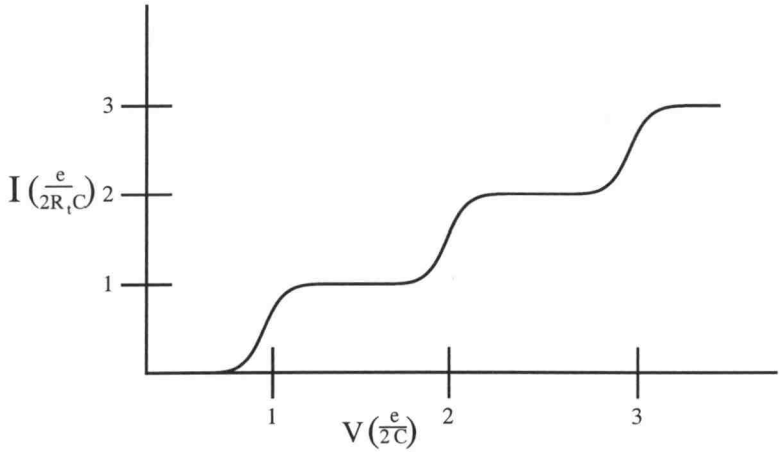

Figure 2.7: Sketch of the Coulomb staircase, where R_t and C are the tunnel junction resistance and capacitance.

tunnel capacitance of the junctions. The region of zero current below $V = e/C_{eq}$ is the Coulomb gap region where near equilibrium Coulomb blockade measurements are performed in this research. In measurements performed in this gap region a gate electrode is coupled to the quantum dot which alters the energy equations.

2.3.2 Coulomb Blockade Peaks

If a gate electrode is coupled to the dot as shown in the circuit diagram in Fig. 2.8 the potential in the dot and therefore tunneling into and out of the dot

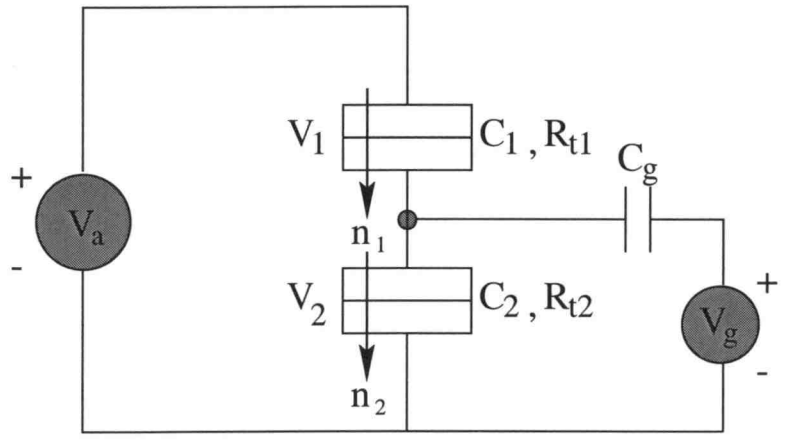

Figure 2.8: Circuit diagram of a quantum dot with a capacitively coupled gate bias.

may be varied by changing the gate bias. This is the circuit configuration used in the equilibrium quantum dot experiments presented in this research. The allowed energy expressions are

$$\Delta E_1{}^{\pm} = \frac{e}{C_{eq}}\left(\frac{-e}{2} \pm [en - Q_p + (C_g + C_2)V_a - C_g V_g]\right) \tag{2.35}$$

$$\Delta E_2{}^{\pm} = \frac{e}{C_{eq}}\left(\frac{-e}{2} \mp [en - Q_p - C_1 V_a - C_g V_g]\right) \tag{2.36}$$

where Q_p is the unintentional polarization charge due to the background impurities.

If only a small source drain bias is applied (relative to the energy level spacings in a semiconductor dot and relative to the Coulomb gap), then the relevant capacitance becomes the capacitance from the gate to the dot as in our picture of a disk coupled to a ground plane (Fig. 2.3). Keeping V_a constant and varying V_g allows the energy levels in the dot to be shifted relative to the Fermi energy in the reservoir. When the level in the dot lines up with the Fermi energy, the electron

can tunnel out of the dot and a non-zero conductance can be observed. As the gate bias is made more negative the level in the dot eventually rises above the Fermi energy of both reservoirs and can no longer contribute to the current. However, in the dot, which now contains one fewer electron, a new level appears at an energy e/C_{eq} above the new Fermi level. As this new energy level rises with gate voltage and lines up with Fermi energy in the reservoirs, an electron is again able to tunnel out of the dot. The level then rises above the Fermi energy, and the process repeats itself until no electrons are left in the dot. The conductance of the dot as a function of gate voltage will then show peaks as illustrated in the sketch of Fig. 2.9 for a metallic dot.

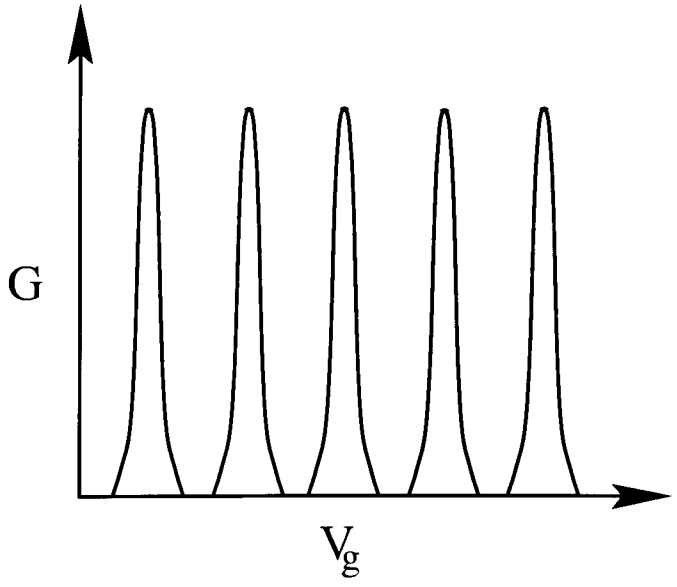

Figure 2.9: Sketch of Coulomb blockade peaks.

An additional condition must be met in order to observe CB. The conductance of the tunnel junctions must be less than a quantum conductance fluctuation [6] otherwise the barriers will not be true tunnel barriers, the charge will not be well localized in the dot and the CB will be obscured. From the uncertainty principle,

$\Delta E \Delta t > \hbar$. The energy gap, $\Delta E \approx e^2/C_{eq}$, and the tunneling time, $\Delta t \approx R_t C_{eq}$. Thus the tunneling resistance R_t determined by the gate bias on the QPC must be greater than h/e^2 or 25 $k\Omega$.

2.3.3 Coulomb Blockade Peaks in a Semiconductor Quantum Dot

Coulomb blockade peaks will appear in a slightly different form in semiconductor quantum dots. In a semiconductor quantum dot the confinement of the electrons will produce larger energy level spacing due to the smaller effective mass and the longer mean free path. A mean free path longer than the dimensions of the quantum dot will allow an electron to reflect back and forth coherently in the dot and build up the standing waves which produce quantization. Scattering can is a level broadening process, where the level broadening is $\hbar/\tau$ due to a scattering time τ. If the level broadening is equal to the level spacing, then the levels will be smeared out. Thus a longer mean free path will lead to a reduced level broadening in semiconductor dots. In addition the smaller effective mass in the semiconductor creates larger energy level spacings which are less likely to be smeared out completely by level broadening.

As an example we can look at the energy levels of a harmonic oscillator potential.

$$V_{ho}(x,y) = \frac{1}{2} m^* {\omega_x}^2 x^2 + \frac{1}{2} m^* {\omega_y}^2 y^2 \tag{2.37}$$

The energy levels can be derived [35] as

$$E_{n_x n_y} = \hbar\omega_x \left(n_x + \frac{1}{2} \right) + \hbar\omega_y \left(n_y + \frac{1}{2} \right) \tag{2.38}$$

The energy level spacing is on the order of $\hbar\omega$ where ω is related to the curvature of the confining potential, which is dependent on the gate biasing. For a smaller effective mass, ω will be larger and the energy level spacing will also be larger.

2.4 Determining 2D Electron Density and Mobility From Experiments

Previously the importance of 2D electron density and mobility to the electron transport in a 2DEG and therefore 1D and 0D devices constructed from 2DEGs was discussed. The experimental determination of these quantities is described below.

When a perpendicular magnetic field is applied to the 2DEG, the effective mass equation in 2D becomes

$$\left[\frac{1}{2m^*}\left(\left(\frac{\hbar}{i}\frac{\partial}{\partial x}+\frac{\partial}{\partial y}\right)-e\vec{A}\right)^2+V(x,y)\right]\Psi(x,y)=E\Psi(x,y), \tag{2.39}$$

where $\vec{A}$ is a vector potential and in the commonly used Landau gauge $A_x = -yB$. Electron transport is in the x direction. This equation is solved in references [6] and [36] where the energy levels for the system are given by,

$$E_n = \hbar\omega_c\left(n+\frac{1}{2}\right), \tag{2.40}$$

where $\omega_c = eB/m^*$ is the cyclotron frequency. In a magnetic feld the 2D subbands of the 2DEG collapse into discrete degenerate energy levels. These discrete levels are broadened due to electron scattering and the density of states will have a Gaussian shape as depicted in Fig. 2.10.

When the Fermi energy is equal to the ideal Landau level energy $E_n = (n + \frac{1}{2})\hbar\omega_c$, there will be a peak in the conductance due to the high density of states. These conductance peaks are known as Shubnikov de Haas oscillations, and can be observed experimentally. As the magnetic field is increased, the energy level spacing increases and the number of levels below the Fermi energy decreases until there are none below the Fermi energy and the resistance goes to infinity. In reality, there will be some states in the tail of the broadened Landau level which will contribute a small amount to the current. The resistance will then be finite, but very large.

As the magnetic field is swept, the Fermi level sweeps between two conductance peaks. The energy at each level $\hbar\omega_c(n + \frac{1}{2})$ is equal to the Fermi level

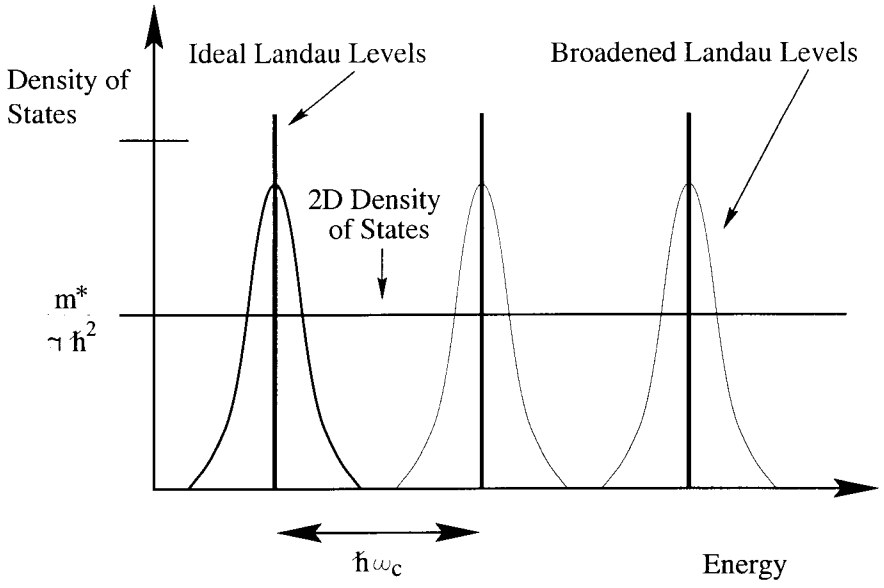

Figure 2.10: Density of states of a 2DEG with a perpendicular magnetic field applied.

$E_f = 2\pi\hbar^2 n_s/m^*$. Therefore,

$$\hbar\omega_c(n+\frac{1}{2}) = \frac{2\pi\hbar^2 n_{2D}}{m^*} \tag{2.41}$$

$$\frac{1}{B_n} = \frac{e(n+\frac{1}{2})}{2\pi\hbar n_{2D}} \tag{2.42}$$

$$\Delta\frac{1}{B} = \frac{e}{2\pi\hbar n_{2D}}. \tag{2.43}$$

In a magnetic field sweep the conductance peaks will be periodic in $1/B$ and the spacing is proportional to the two dimensional density of states. A plot of the measured resistance versus magnetic field for the material G1135 is shown in Fig. 2.11. The 2D density obtained from this data is $\sim 2 \times 10^{11}\ cm^{-2}$. Since data was obtained from a two terminal measurement, included in the curve is the hall resistance which is the resistance perpendicular to the direction of transport in the plane of the 2DEG. The plateau at the first conductance step $e^2/h \sim 12.5$ $k\Omega$. The resistance reaches plateaus when the Landau level energy is equal to the Fermi energy. This is known as the quantum Hall effect and was discovered by

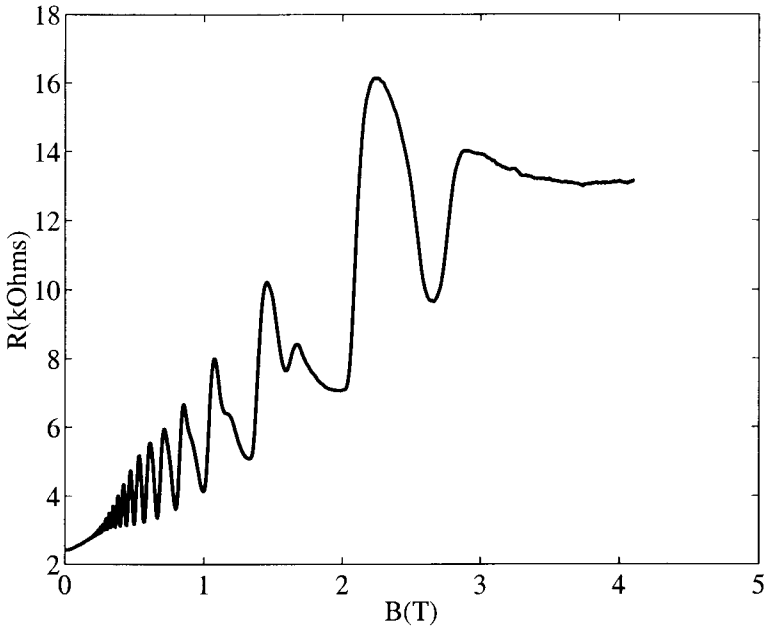

Figure 2.11: Shubnikov de Haas oscillations with the second integer Hall plateau $(2e^2/h)$ for material G1135.

von Klitzing *et, al.* in 1980 [37]. For a review of this phenomenon see [36] or [38].

The mobility can be determined from the measurement of the resistance parallel to the direction of transport at $\mathbf{B}$=0 T. The resistivity, ρ_{2D}, is the resistance per square and the mobility can be determined from $\rho_{2D} = (\mu ne)^{-1}$. In a Hall bar configuration the number of squares is equal to the channel length over the channel width. A Hall bar configuration is shown in Fig. 2.12. The Van der Pauw method can be used to determine the mobility in samples without a square geometry and is discussed in Ref. [39].

2.5 Aharonov-Bohm Oscillations

The Aharonov-Bohm (A-B) effect observed expermentally demonstrates the phase coherence of electrons on the mesoscopic scale. A ring like 1D mesoscopic structure (see Fig. 2.13) with only a few modes conducting acts as an electron

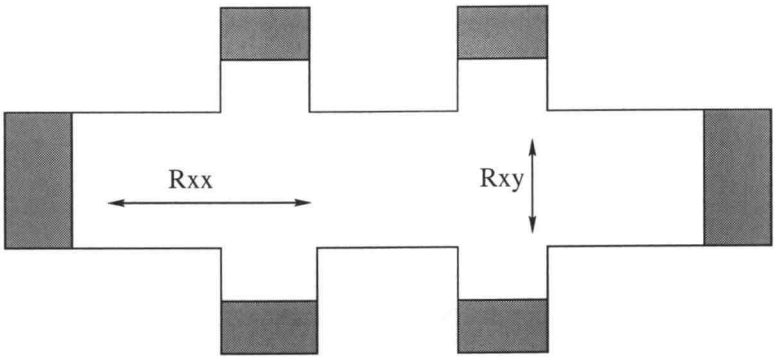

Figure 2.12: A symmetric Hall bar configuration where the longitudinal resistance R_{xx} is in the direction of electron transport, the transverse resistance R_{xy} is measured via voltage probes to determine the location in magnetic field of the quantum Hall plateaus. The magnetic field is applied perpendicular to transport into the page.

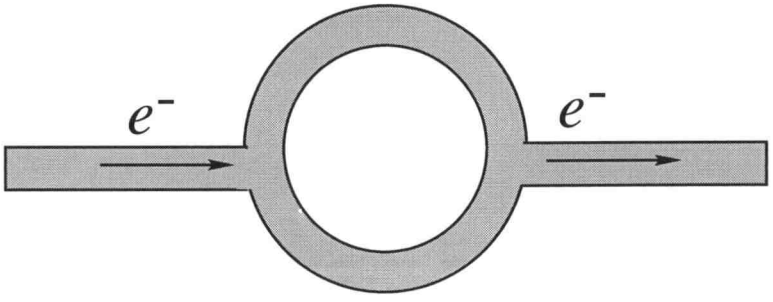

Figure 2.13: A 1D ring structure. Electron waves are split as they enter the ring and recombine at the exit.

waveguide, and splits the wave of the electron as it enters the ring. The split waves propagate separately around each side of the ring and then recombine at the exit. Depending on the size of the ring (length of propagation), the waves will interfere constructively or destructively and the overall transmission will depend on this interference. A magnetic field applied perpendicular to the plane of the ring will produce a vector potential parallel to the ring and perpendicular to the direction of electron transport. Therefore a phase difference will be introduced between waves propagating on either side of the ring. The transmission through the ring can be

modulated by sweeping the magnetic field. This phenomena was first observed in etched heterostructures by Webb [40], Ishibashi [41], and Mankiewich [42] and in split gate structures by Ford *et al.* [43] and Van Wees *et al.* [44].

In a similar vein, when a magnetic field is applied to a quantum dot, edge states form which provide spatially separate paths of wave propagation. Sweeping the magnetic field will produce oscillations in the conductance of the dot. These oscillations will be periodic in magnetic (**B**) field and are related to the area of the dot, A,

$$A = h/e\Delta B. \tag{2.44}$$

2.6 Literature Review

Coulomb blockade or single electron tunneling was predicted as early as 1951 and was first observed in metallic systems [45]. Since the fabrication technology became available, many experiments have been performed on semiconductor quantum dots. Coulomb blockade was first seen in semiconductors in the experiment by Scott-Thomas *et al.* [46] on a MOSFET structure, and Meirav *et al.*, Kowenhoven *et al.* and Staring *et al.*[47]–[49] subsequently observed the effect in AlGaAs/GaAs structures. The properties of single dot systems have been studied extensively and include probing the electronic states with a magnetic field and probing with higher source/drain biases for systems where the intrinsic energy level spacing is much less than the charging energy and is negligible and for systems where it is not negligible [50]–[54]. A split gate structure with a noninvasive voltage probe was used to observe Coulomb charging by indirectly measuring the potential on the dot with out destroying the charge state [13]. Most recently a similar structure was used to determine the path of en electron in an "electron interferometer" [55].

In addition, measurements have been made on symmetric multiple dot systems (artificial molecules) where peak splitting occurs when interdot coupling is increased

[56, 57]. Peak splitting occurs due to a lifting of the degeneracy of the individual dot states and a suppression of internal polarization. Both the tunneling and interdot capacitances were seen to play a role in the peak splitting. These were the first experiments where the dot coupling, and therefore peak splitting, could be controlled via tunable gates.

Molenkamp *et al.* used the conductance of one dot of a double dot system to probe the potential on the second dot and observed the charging energy scaling quadratically with the reflection probability of the barriers in agreement with theory [58]. Van der Vaart *et al.* observed Lorentzian shaped resonances in coupled dots when discrete energy levels of each individual dot were aligned [59]. Hofmann *et al.* observed switching in parallel quantum dots due to single electron charging and interdot capacitance [60]. Asymmetric double dots have also been investigated. See for instance Blick *et al.* [61] Experiments have also been carried out on arrays of dots consisting of more than two dots in series [62, 63]

In other measurements the behavior of the Coulomb oscillations as a function of the coupling to the leads [64]–[66] was investigated. In the experiments by Van der Vaart *et al.*, Coulomb oscillations are suppressed when the conductance to one lead is $g_q = 2e^2/h$, whereas in the experiments by Pasquier *et al.*, the oscillations persist up to a lead conductance of several g_q. In the experiments by Crouch *et al.* the oscillations disappear when the conductance to one lead is equal to g_q and reappear above $2e^2/h$. Intersubband scattering due to disorder is proposed to explain the persistence of scillations above g_q. The effect of interdot coupling on Coulomb oscillations was explored and the double dot ground state charge configuration was determined [67]–[70]. The affect of interdot coupling on the peak positions and shapes was studied and the results were shown to agree with a many body charge fluctuation theory showing quantum mechanical charge sharing between dots.

Other measurements on quantum dot transport in magnetic fields include the

experiments by van Wees *et al.* in which they observed Aharonov-Bohm oscillations in the equilibrium conductance of a quantum dot [44] and very recent experiments by Tarucha *et al.* [71] and Kouwenhoven *et al.* [72] on the excitation spectra of a symmetric few electron quantum dot. In a similar fashion Stewart and collaborators [73] observed the evolution of excited state spectra in an irregularly shaped dot containing many electrons. For a comparison and contrast of the experiments on the few electron and many electron systems see the accompanying article in *Science* by Paul McEuen [74].

In contrast to most of the experiments previously discussed where the coupling of the quantum dot to the leads is weak, experiments on open quantum dots where the coupling to the leads is strong have been extensively studied by Jon Bird and colleagues. They looked at the the nature of the transport in a magnetic field through the 1D-0D-1D coupled system and investigated the phase coherence of electron waves in these systems [75, 76]. Ochiai *et al.* have examined phase breaking in open dot arrays [77]. And Linke *et al.* have examined phase breaking of nonequilibrium electrons in open quantum dots [78].

Most of the aforementioned measurements were performed in the near equilibrium regime. In the nonequilibrium regime the Coulomb staircase was observed by Kouwenhoven *et al.* for symmetric and anti-symmetric barriers [79] and a quantum dot turnstile was demonstrated to operate at frequencies up to 25 MHz [80]. Dixon *et al.* examined the nonlinear transport properties of a double dot system and observed overstructure on the linear Coulomb oscillations due to alignment and misalignment of the energy levels in the two dots [81].

Far from equilibrium transport has been explored in vertical heterostructures in which switching behavior was observed and attributed to electron heating [82], and in laterally defined double barrier systems in 2DEGs where ballistic hot electron transport was investigated [83] . Wu *et al.* observed switching behavior in

a semiconductor quantum dot [84] which was explained by a hot electron model [85]. Subsequent measurements of quantum point contacts on the same material also exhibited switching behavior [86, 87]. Switching phenomena in a dot is further explored in the research presented here.

3. FABRICATION AND MEASUREMENT

3.1 Shrinking Dimensions

This section contains a description of the steps involved in making a semiconductor quantum dot, a description of the device design, and a survey of alternative fabrication techniques.

As discussed in Chapter 2, confinement in one dimension can be achieved by growing a heterostructure material such as GaAs/AlGaAs. Further confinement of electrons in the 2DEG to one dimensional (1D) channels or zero dimensional (0D) dots can be achieved by using the split gate technique illustrated in Fig. 3.1. In the split gate technique, a metal gate is formed on the surface of the material using electron beam lithography as discussed in Section 3.3. The distance from the 2DEG to the surface ranges from approximately 300 Åto 1200 Å. Applying a negative voltage to the gate pattern shown in Fig. 3.9 will deplete electrons underneath the gate and leave a small island of electrons isolated from the rest of the 2DEG reservoir, forming a quantum dot.

3.2 Material Growth and Photolithography

Sandia National Laboratories in Albuquerque, N.M. provided the material, material characterization, and photolithography for the devices studied here. At Sandia, molecular beam epitaxy (MBE) and metal organic chemical vapor deposition (MOCVD) were used to grow the heterostructures shown in Fig. 3.2. In the MBE material the 2DEG was 1180 Åbelow the surface and had a density of $2 \times 10^{11}\ cm^{-2}$ and mobility of 6×10^5-$1 \times 10^6\ cm^2/Vs$ at 4.2 K. In the MOCVD material the 2DEG was 975 Åbelow the surface and had a density of $3 \times 10^{11}\ cm^{-2}$ and a mobility of 6×10^5-$1 \times 10^6\ cm^2/Vs$ at 4.2 K.

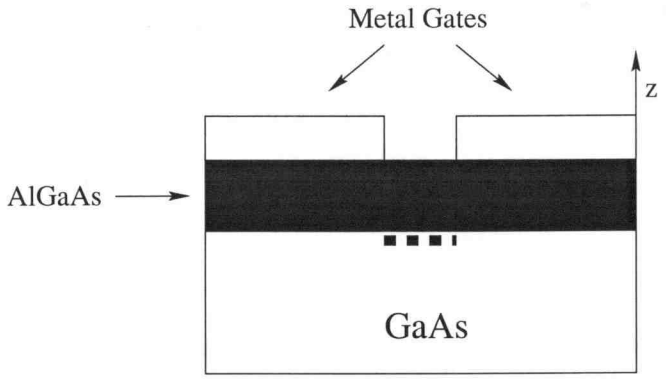

Figure 3.1: Cross section of split gates on the surface of a GaAs/AlGaAs heterostructure.

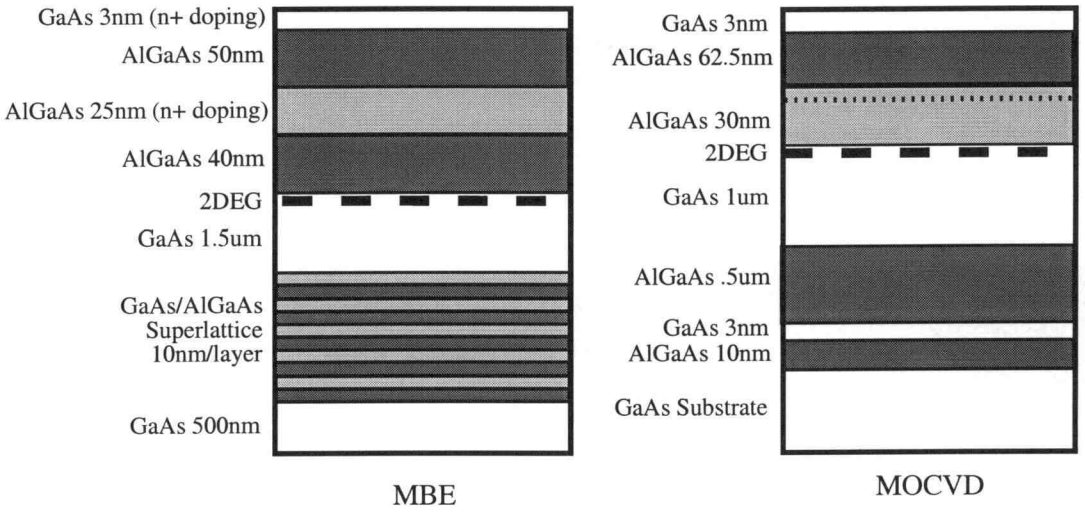

Figure 3.2: Layer structures of material used in this research.

Photolithography, or optical processing, was needed to define a gate pattern to transition from the very small dimensions of the nanostructure device being studied to a pattern large enough to connect wires from the chip to a sample holder, and finally to a coaxial cable in order to make transport measurements. Gold wire bonding, a standard technique used in IC packaging was employed. The optical processing performed at Sandia involved three main stages: mesa etching, ohmic

contact definition and deposition, and interconnect definition and deposition. Each stage began with a masking step which involved spinning on a photoresist (5000 *rpm* for 30 *s*) and soft baking (90 °C for 90 *s*), exposing the resist with ultraviolet light through a patterned mask (3.3 *s*), and removing (developing) the exposed resist (1:5 400k:H_2O for 60 *s*) to leave the desired pattern on the substrate shown in Fig. 3.3 [88].

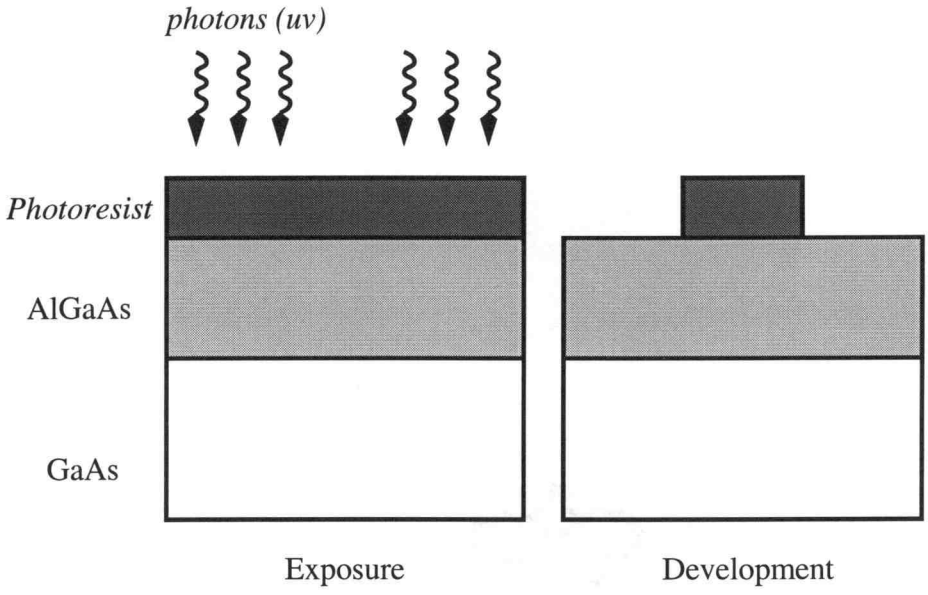

Figure 3.3: The masking step for the optical processing.

A mesa was patterned to isolate a portion of the 2DEG from the rest of the chip as shown in Fig. 3.4. After the masking step, an oxygen plasma descum (5W for 90 *s* at 650 mTorr) removed any leftover organic material in the exposed areas. Then a wet etch of phosphoric acid (1:4:45 H_3PO_4:H_2O_2:H_2O for 90 sec. at 50 Å/sec.) removed the exposed area down to the thick buffer layer of GaAs. The remaining photoresist was dissolved in acetone, and the AlGaAs mesa with the desired pattern remained

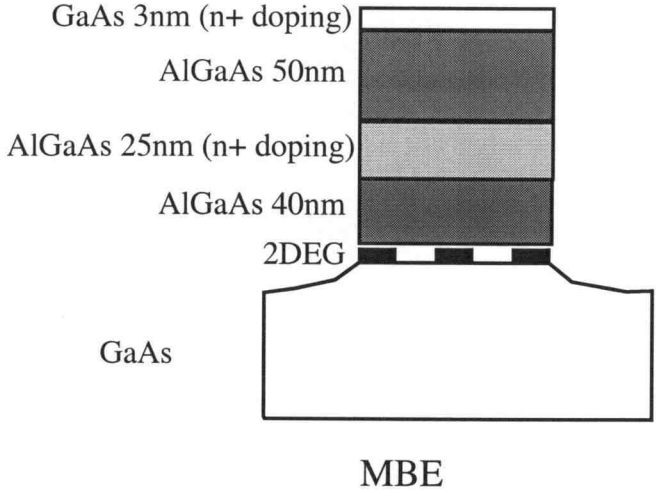

Figure 3.4: Cross section depicting the mesa.

Ohmic contacts are needed to connect to the 2DEG source and drain of the device and were fabricated at Sandia. After a masking step to define the contacts and a plasma descum, a light etch was done (20:1 H_20:NH_4OH for 30 s) to remove any native oxide (leaving the oxide results in poor ohmic contacts). Then, the sample was immediately placed in the vacuum evaporator and four layers of metal were deposited in the following order (1)Ge- 270 Å(2)Au-540 Å(3)Ni-140 Å(4)Au-2000 Å. Finally the photoresist was dissolved and the excess metal lifted off. The contacts were annealed (420 °C for 90 s) to promote diffusion of the Ge and the first layer of Au into the semiconductor and 2DEG layer. The Ni layer provided a barrier to prevent the top layer of Au from diffusing so that a solid contact pad remained on the surface to which gold wires could be bonded.

Interconnects on the surface of the mesa linked the split gates of the device to 100 μm^2 bonding pads. Again a masking step defined the pattern and 200 Åof Ti and 2000 Åof Au were deposited to form the interconnects. A layout of the mesa, ohmic, and interconnect pattern is shown in Fig. 3.5.

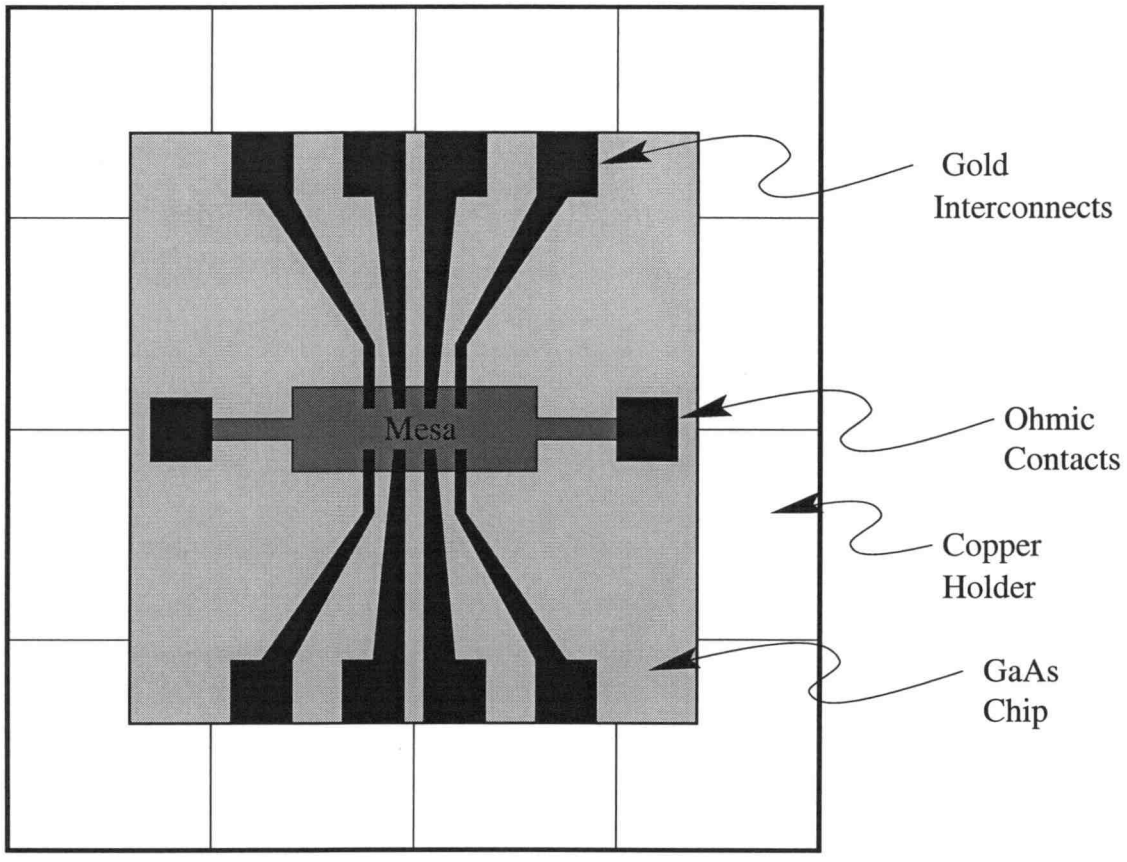

Figure 3.5: Layout of the mesa structure, ohmic contacts, and interconnects.

3.3 Electron Beam Lithography

Electron beam lithography at the University of Oregon was employed to pattern the split gates of the quantum dot devices on the substrate material provided by Sandia. The gate metal consisted of a combination of Au and Ti. Au is used for its high conductivity and Ti used to help the Au stick to the surface of the material. The electron beam processing included two lithography stages. One stage to pattern the device and one stage to pattern patches to securely connect the device to the optically defined interconnects. There were five basic steps to deposit a gate pattern. These steps are shown in Fig. 3.6 with steps one and two combined in the first picture. First a polymer resist sensitive to exposure to high energy electrons

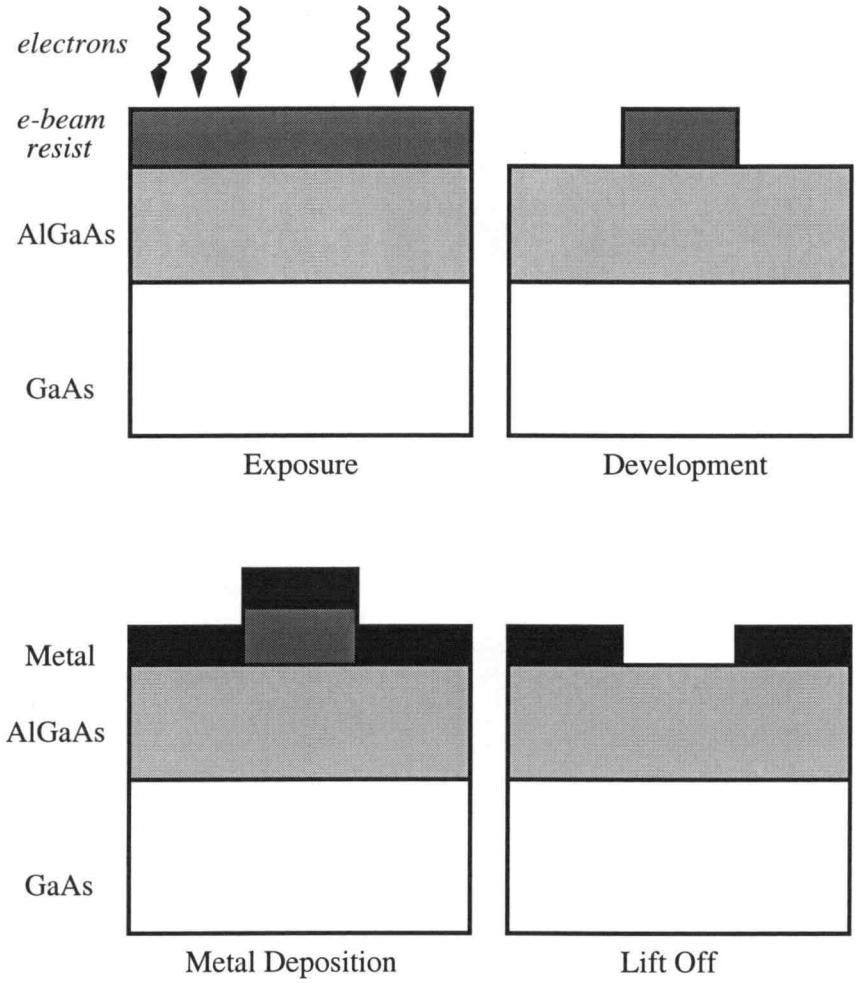

Figure 3.6: The steps of electron beam processing.

(positive e-beam resist) was spun onto the sample. Then the e-beam resist was exposed to an electron beam using a scanning electron microscope (SEM). When a polymer resist is exposed to electron radiation, chain scission occurs. The scission process lowers the molecular weight causing the exposed area to become soluble [89]. The exposed resist was then developed, metal deposition was performed, and lift off of the resist left the desired split gate pattern.

3.3.1 SEM Resolution

The resolution of the SEM is a crucial component to achieving the small device dimensions required. In general, for a given substrate and well focused beam, a higher magnification and accelerating voltage leads to a higher microscope resolution, a smaller beam size, a smaller backscattering area (Fig. 3.7), and, therefore, smaller achievable split gate dimensions [90, 91, 92]. Beam focusing is dependent on aperture centering in the microscope column and astigmatism adjustment (electromagnetic rather than optical lenses) [93]. Initial attempts to reach these small dimensions were made at Oregon State University using a Hitachi SEM with a maximum magnification of 200,000X and an accelerating voltage of 30 kV. The minimum line width achieved with the Hitachi SEM was 0.5 μm. Further attempts were made at Oregon State University on a JEOL SEM with a maximum magnification of 300,000X and accelerating voltage of 40 kV. However, this SEM was located on the fourth floor of the building and incurred vibration problems which permitted a resolution of only .2 μm, still too large for the designed dot pattern. In addition this minimum line width was not reliably reproducible as the vibrations in the building were constantly changing. Finally, at the University of Oregon, another JEOL SEM with similar specifications located in the basement of Willamette Hall on an isolated concrete slab was used to obtain easily reproducible line widths of 0.1 μm. With this SEM the desired device pattern was achieved.

3.3.2 Exposing With Electrons

A difficulty encountered in the fabrication process was determining the correct exposure necessary for the specific device pattern and particular substrate. The electron beam exposure depends on the substrate material on which the electron beam resist is spun. It is the scattering of the electrons from the substrate back into the resist (backscattering, Fig. 3.7), rather than the initial pass of the electrons

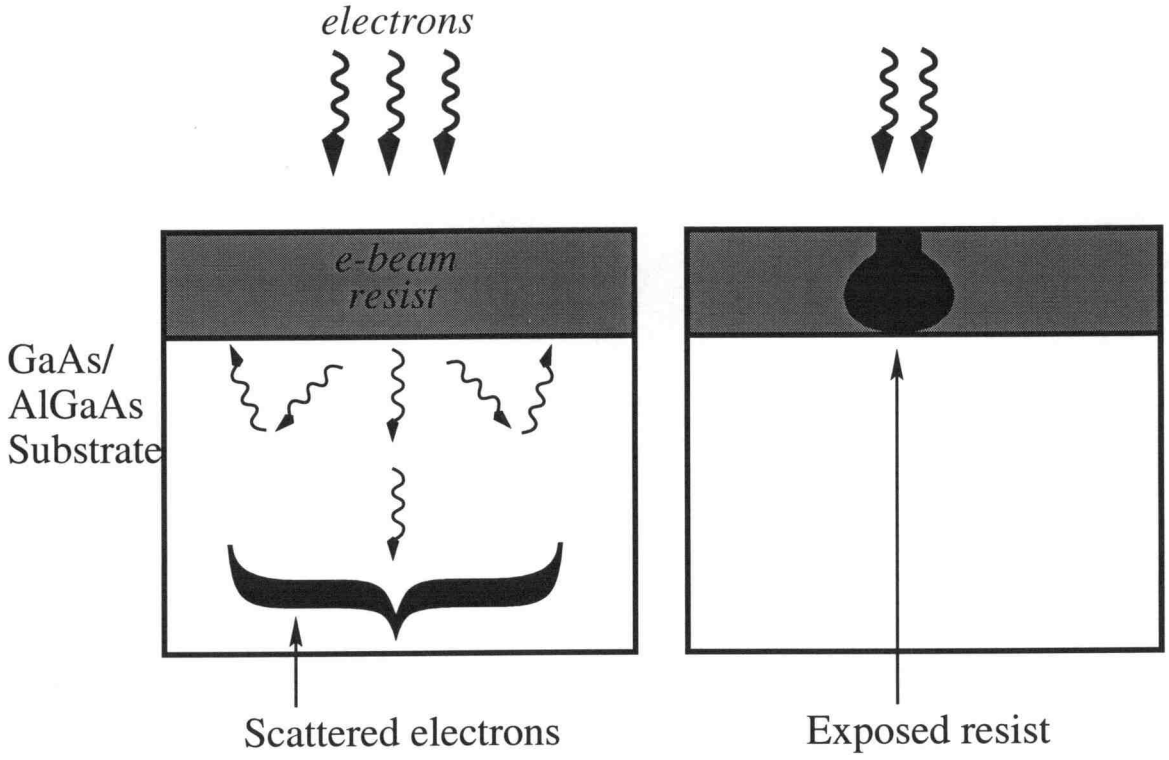

Figure 3.7: Electron backscattering is responsible for exposing the e-beam resist.

through the resist, which contributes significantly to the exposures [90]–[92]. Since the backscattering is substrate dependent, the exposure must be adjusted for each substrate. Devices were made on three different types of material. The initial test exposures and practice devices were done on a bare GaAs chip. Then actual devices were made on high mobility MOCVD and MBE material from Sandia.

During electron beam lithography the device was connected to the optical lithography on the surface of the material by intermediate leads. The challenge in this stage was to obtain an even exposure and thus a clean lift off across an area of approximately 100 μm^2 while maintaining the delicate 100 nm features in the center of the device. The proximity effect (Fig. 3.8) will give an additional low level exposure around the area intended to be exposed [90, 91, 92]. The unintended additional exposure will occur in a radius of approximately 1 μm. Usually the

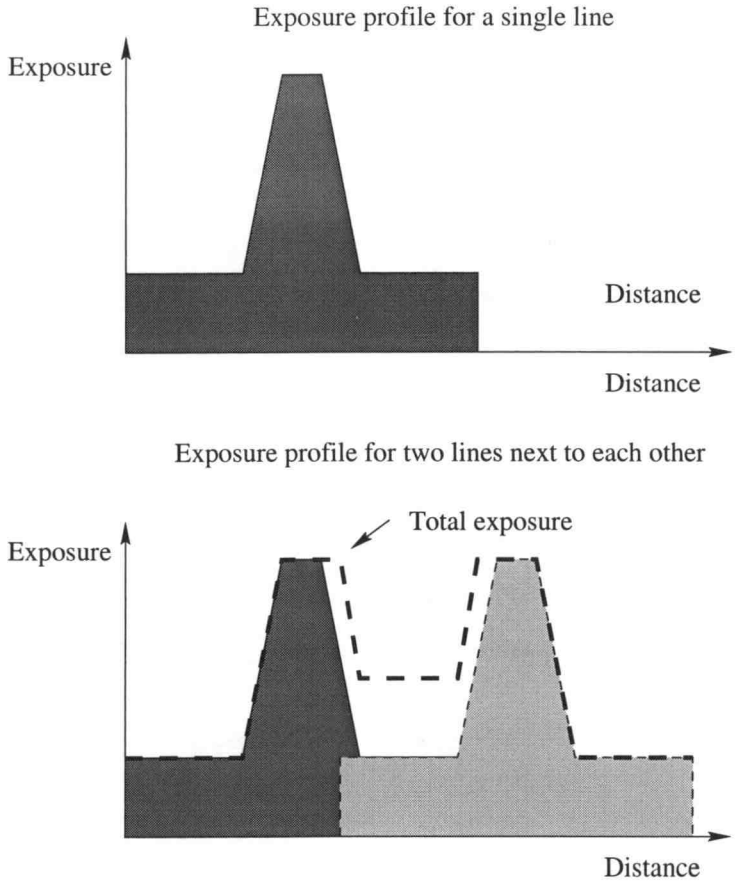

Figure 3.8: Exposure profiles for a single line and two lines together.

proximity effect is undesirable as it can lead to overexposure and a device which is larger than the designed patterned. However, around the delicate 100 nm features the pattern can be drawn smaller than the final size required and the proximity effect can be used to help expose adjacent lines. This effect will not help to expose the adjacent lines of the larger features which span the 100 μm^2 area. The correct exposure settings will then fall in a very narrow range. The patterns for the devices fabricated in this research were written using a 5 pA beam current, an accelerating voltage of 40 kV, and an exposure of approximately 500 $\mu C/cm^2$.

3.3.3 E-beam Processing and Device Design

Polymethylmethacrylate (PMMA) is a positive e-beam resist which gives a high resolution and has a low sensitivity to exposure and is ideal for use in designing structures with small feature sizes [89]. In order to coat the substrate material with the e-beam resist, a 1 cm^2 chip was placed on an Integrated Technologies model P-6204 resist coater and several drops of a 3 percent solution of 950,000 MW PMMA in chlorobenzene were spun at 4000 rpm for 20 s to achieve a resist thickness of 2000 Å. Prior to exposure the resist was baked for several minutes above 160 °C.

The pattern was drawn using Design CAD software, and NPGS software was then used to compile the Design CAD drawing and control the electron beam. A JEOL-840A SEM was used along with the NPGS pattern generator software to expose the resist in the drawn pattern. By trial and error an even exposure was obtained so that the device and leads could be fabricated with a single exposure in one stage of electron beam lithography, avoiding additional NPGS program files and any further alignment steps, and saving time.

Developing was done using a solution of 3:1 Isopropyl Alcohol (IPA):Methyl Isobutyl Ketone (MIBK) for 70 s at 25 °C followed by a rinse in (IPA) and deionized water (DI) water for 20 s each. After developing the exposed resist, 50 Åof Ti and 200 Åof Au were deposited using an Edwards thermal evaporator. The resist was then lifted off in acetone leaving behind the patterned gates directly on the surface of the GaAs layer.

Using the split gate technique, a circuit of two quantum dots in series was developed. A layout of this structure is shown in Fig. 3.9. The dots are formed by applying negative voltages to the barrier gates, common gate, and plunger gates to to deplete electrons underneath them and isolate puddles of electrons. The common gate and the sensor gates together form 1D channels or ideally quantum point contacts, discussed in Chapter 2. Fig. 3.10 is an SEM picture of one of the

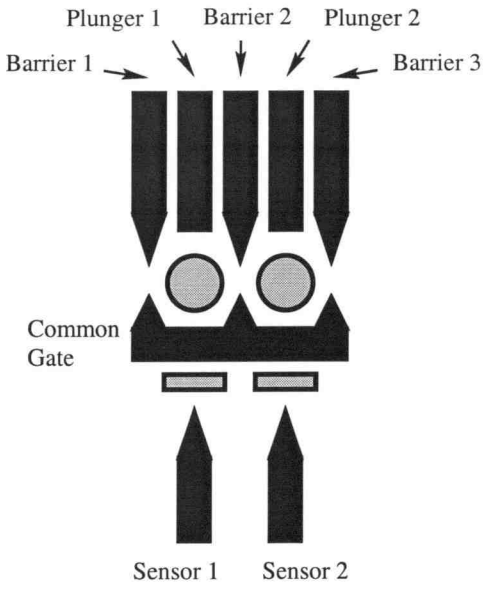

Figure 3.9: Schematic of the double dot device design. The narrow gates are designed to be 100 nm wide and the dots 400 nm^2.

devices. The narrow gates are designed to be approximately 0.1 μm or 100 nm wide and the dots 400 nm across.

3.4 Alternative Fabrication Techniques

Many other methods of fabricating nanometer scale patterns exist. M. B. Stern et al. [94] and H. van Houten et al. [95] have combined electron beam lithography with reactive ion etching (dry etching) to create long narrow channels in the 2DEG of a GaAs/AlGaAs heterostructure material. Damage caused by the ion beam can lead to depletion of carriers in the 2DEG. A. Scherer et al. [96, 97]. have considered this effect and extended the reactive ion etching technique to achieve narrow 75 nm channels in the 2DEG of a GaAs/AlGaAs material. These 75 nm 2DEG channels are approximately the same dimensions as the lithographically defined channels, which is not the case in the split gate technique.

Attempts at nanostructure fabrication have been made with a scanning tun-

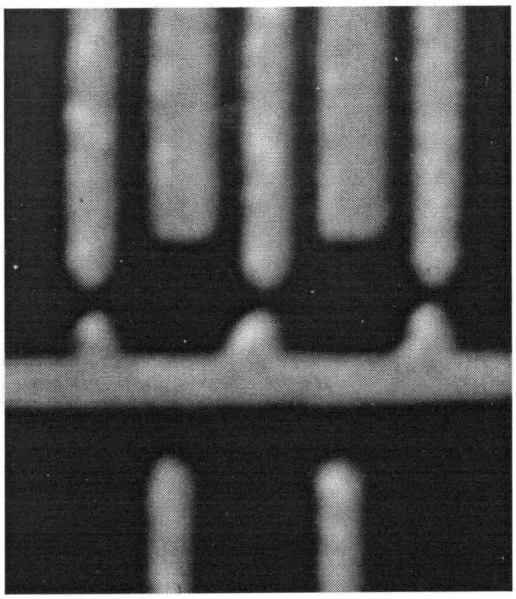

Figure 3.10: SEM micrograph of a double dot device. The dark square regions of the dot are $\sim 400\,nm^2$ and the narrow Au gates are $\sim 100\,nm$ wide.

neling microscope (25 nm linewidths) [98] and using x-ray lithography (30 nm linewidths) [99]. The use of higher accelerating voltages ($> 50\ kV$) and a transmission electron microscope (TEM) rather than an SEM can create smaller minimum linewidths on the order of 5 nm [100]. Many groups have used the Stranski-Krastanow crystal growth mode to grow self-assembled quantum dots in InAs/GaAs as well as other semiconductor material combinations using metal organic vapour phase epitaxy (MOVPE), chemical beam epitaxy (CBE), and MBE. [101]–[103]. These self-assembled growth methods can easily create large systems of quantum dots with small dot size.

Quantum dots and single electron transistors have been made in silicon by combining standard silicon processing techniques with electron beam lithography [104]–[106]. The technological development of Si fabrication techniques far surpasses that of other semiconductors and could be a great advantage in the fabrication of Si dots. In Si the mobility of the electrons in the 2DEG is much lower than in GaAs

due mostly to the interface roughness. Due to this increased scattering, it is difficult to observe some quantum effects.

Tunnel junctions and electron islands have also been made in metallic systems. The Al/AlO_x shadow mask technique can produce small area junctions (< 40 nm^2)[107]. and $Al/AlO_x/Al$ tunnel junctions as small as 5 nm^2 have been fabricated using the self-aligned in-line (SAIL) technique [108]. Tunnel junctions have been created by electron beam lithography of metal wires and atomic force microscope (AFM) machining of gaps in the wires. [109]. Metal tunnel junctions with areas of 2 nm^2 have also been fabricated using high resolution electron beam lithography and an ionized beam deposition technique [110].

Metallic islands of gold nanograins (1-4 nm) have been deposited by a liquid metal ion source and focused ion beam [111, 112, 113]. Solutions containing Au55 nanoclusters have been deposited on various substrates [114] and in some cases passivated with an electron beam [115]. Evidence of Coulomb blockade behavior has been observed in the transport characteristics. These type of techniques in metal systems, like the self-assembled growth techniques in semiconductor systems, allow the fabrication of larger systems of dots with small dot diameters.

3.5 Cryogenic Systems

This section describes the cryogenic systems and instrumentation used to measure the quantum dot devices. Three cryogenic systems, two at the University of Oregon and one and Arizona State University, were employed in the experiments.

3.5.1 Cryogenics Overview

Cryogenic systems [116]–[118] are needed to observe much of the phenomena studied in quantum devices (Coulomb blockade is an exception in very small systems which are 10 nm or less). When matter, in this case a semiconductor crystal, is

cooled to liquid nitrogen (LN_2) temperatures, 77 K, and below, the vibrational motion of the lattice, or the number of phonon modes available, is greatly reduced. Thus scattering of the electrons with the lattice vibrations, or phonons, is suppressed and with a small enough amount of background impurity scattering, the quantum mechanical properties of electron transport can be observed.

Cryogenic temperatures are reached by using liquified gases such as LN_2 and liquid ^{4}He (LHe). The temperature at which ^{4}He liquifies is 4.2 K, so a sample is cooled to 4.2 K by putting it in thermal contact with a LHe bath. In order to go below 4.2 K, the evaporative cooling technique is used. In the evaporative cooling technique, the vapour pressure over a bath of LHe is reduced by pumping on the bath. Below 2.17 K LHe becomes superfluid and the liquid flows very freely, and can climb the walls of its containers. This adds an additional load to the pumping system and makes it difficult to reduce the temperature further unless the flow is restricted. Restricting the flow, however, diminishes the evaporation and thus a balance must be struck between the pumping capacity and the amount of flow. In practice a temperature near 1K is routinely obtained with this technique.

Reaching temperatures below 1K requires the use of a rare isotope of helium, ^{3}He. Liquid ^{3}He systems which use evaporative cooling reach temperatures down to 300 mK. To go below 300 mK a mixture of ^{3}He and ^{4}He must be used in a dilution refrigerator (DR) system. (Liquid ^{3}He/^{4}He mixtures have special properties which can be exploited to reach temperatures on the order of 10 mK. As shown in the phase diagram of liquid ^{3}He/^{4}He (Fig. 3.11, below 860 mK and for concentrations of ^{3}He greater than 6.5 percent, phase separation takes place. The ^{3}He rich (concentrated) phase is less dense than the ^{4}He rich (dilute) phase, and thus the concentrated phase will float on top of the dilute phase.

At temperatures below 860 mK, if liquid ^{3}He is added to pure liquid ^{4}He, the ^{3}He will go into solution. At a certain concentration, designated by the lower left

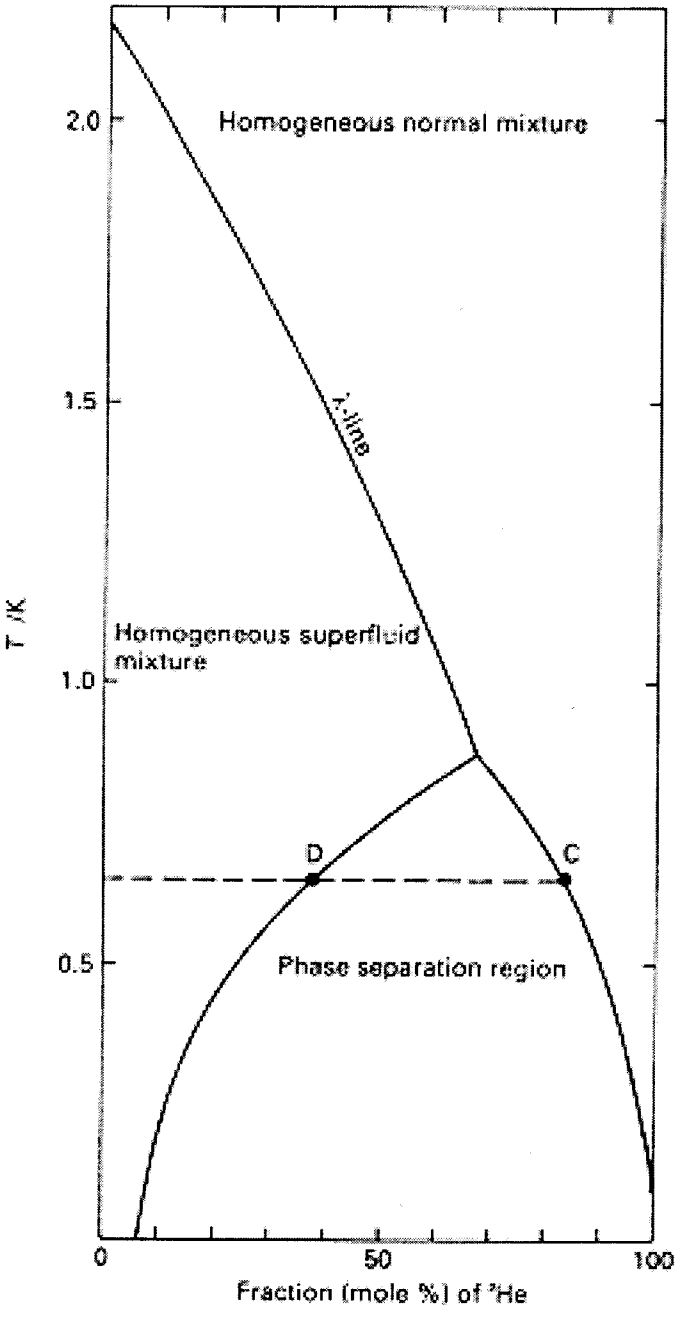

Figure 3.11: The $^3He/^4He$ phase diagram. At temperatures below 860 mK and ^3He concentrations greater than 6.5 percent, phase separation occurs.

curve in the phase diagram, the mixture will separate into the two phases mentioned above. Because ^{3}He obeys Fermi-Dirac statistics and ^{4}He Bose-Einstein statistics, ^{3}He will evaporate preferentially out of the dilute phase at low temperatures. In order to maintain an equilibrium concentration in the dilute phase, ^{3}He crosses the phase boundary from the concentrated phase. The dilute phase has a higher entropy than the concentrated phase, so the migration of ^{3}He across the phase boundary removes energy from the system, providing cooling. Measurements were done in two types of low temperature systems described above, a 1 K ^{4}He unit and two ^{3}He/^{4}He DR units.

3.5.2 The 1 K Transportable Cryostat

A 1 K transportable cryostat was used to do preliminary checks of the gates for pinch off and the ohmic source-drain contacts for stability and linearity. The 1 K transportable system was designed and built at the University of Oregon by J. Wu and B. Wendring and a schematic is shown in Fig. 3.12. The cryostat was designed to be inserted directly into a standard wide mouth 30 l LHe dewar. The copper sample stage was surrounded by a brass vacuum can (IVC) with a tapered grease seal. A 1 K pot with a stainless steel capillary tube leading to the LHe bath was situated directly above the sample stage in the IVC. A calibrated carbon resistor sat on the stage very near the sample to monitor the sample temperature.

Silver paint, which provided a good thermal and electrical contact, was used to mount the sample holder onto the copper stage. Electrical connections from the sample holder to the stage were made by silver painting short pieces of insulated copper wire. Electrical connections from the sample stage to the top of the cryostat consisted of two bundles of twisted pairs of insulated copper wire in order to reduce inductive coupling of stray electromagnetic fields. The wiring was heat sunk at 4.2 K to the insert wall and at the 1 K pot, and was coiled to provide a long thermal

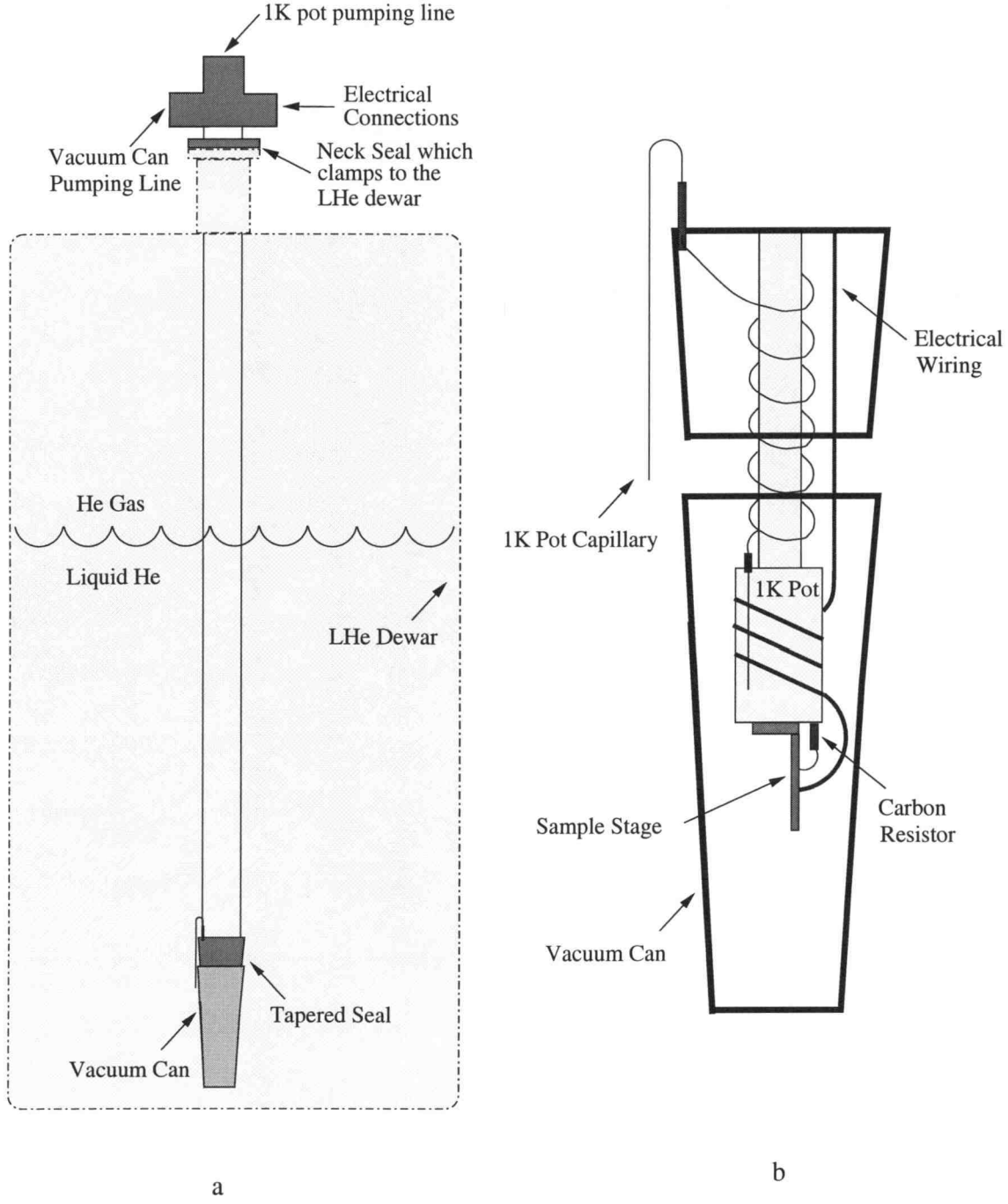

Figure 3.12: The 1 K continuous flow transportable cryostat. (a) View of the entire insert (b) Close up of the low temperature portion

path from the stage to the top of the cryostat (300 K), thus reducing heating of the sample by the leads.

First the IVC was pumped overnight to a pressure of less than 2×10^{-6} Torr in order to purge the system of any contaminants (water, nitrogen) and check it for leaks. If contaminants such as nitrogen or water are present when a system is cooled below their freezing points, they will freeze out, and the thermal mass that they contain will prevent the system from cooling further. After the initial evacuation of the IVC, ^{4}He exchange gas was transferred into it to provide a thermal path to cool the sample to the temperature of the LHe bath, 4.2 K. Between 300 K and 4.2 K the cooling rate of the sample could be controlled by the rate at which the cryostat was lowered into the LHe dewar. Shortly before the sample temperature reached 4.2 K, the IVC was pumped out with a high vacuum diffusion pump to prevent the ^{4}He exchange gas from condensing and prohibiting further cooling. Then a rotary pump was used to pump on the 1 K pot which provided a continuous flow of LHe through the capillary and cooled the sample below 4.2 K. With this system a base temperature of 1.2 K was achieved.

3.5.3 The Oxford Dilution Refrigerators

Two different commercial Oxford Instruments Kelvinox DR systems, one at the University of Oregon (UO) and one at Arizona State University (ASU), were used to do the bulk of the measurements. A schematic of the UO system is shown in Fig. 3.13. The different features of the two systems are listed in Table 3.1. Sample mounting and wiring was similar to that described in the 1 K transportable cryostat, however operation of the DR systems was more complex than that of the simple 1 K system.

Initially, the outer vacuum chamber (OVC) was pumped overnight to approximately 2x10^{-6} Torr. It was important to have a good vacuum in the OVC in order

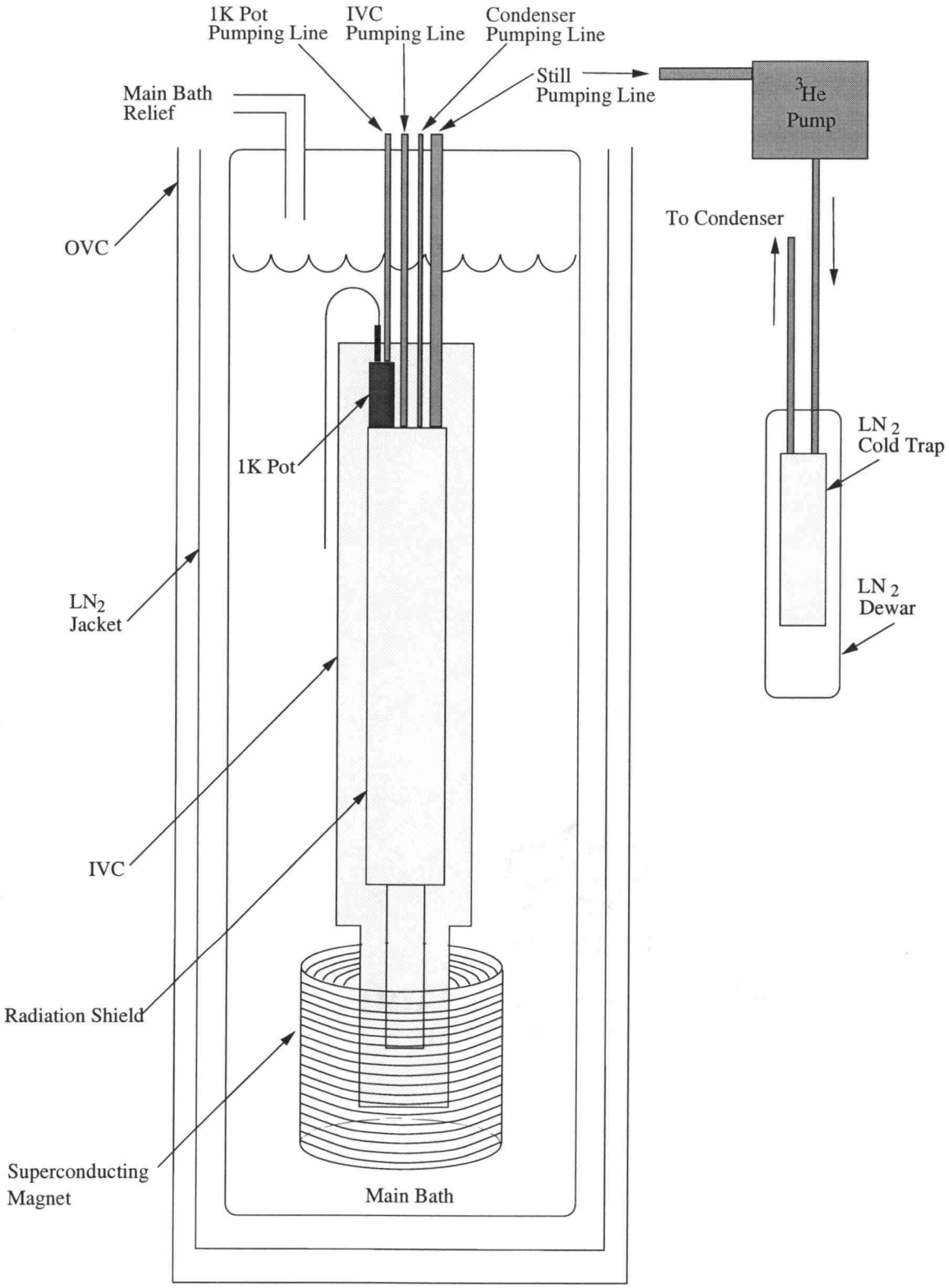

Figure 3.13: Schematic of the University of Oregon dilution refrigerator system.

Table 3.1: Comparison of the ASU and UofO dilution refrigerator systems.

Features	ASU DR	UO DR
Model	Commercial Oxford Instr. DR (1998)	Commercial Oxford Instr. DR (1987)
Ideal Base Temp.	10 mK	20 mK
Mixture Capacity	30l	11l
LHe Usage/Day	25l	11l
Outer Insulator	OVC	OVC
Inner Insulator	Superinsulating Material	LN_2 Jacket
No. of LN_2 Cold Traps	2	1
No. of LHe Cold Traps	1	0

to reduce the rate of evaporation of LHe in the main bath. The IVC was pumped for several hours to $2x10^{-6}$ Torr, leak tested to insure a good vacuum in LHe, and finally filled with a small amount of ^{4}He exchange gas. All pumping lines were evacuated and the cold traps were heated and pumped to remove any contaminants which would freeze at operating temperatures and could potentially block narrow constrictions in the system. The LN_2 cold trap was then filled and the ^{3}He/^{4}He mixture was purged of contaminants by circulating it through the cold trap. The main bath was pumped out, and the throughput between the condenser and the still and from the main bath through the needle valve to the 1 K pot was checked by pressurizing with ^{4}He gas. The main bath was filled with LN_2 and left overnight to cool the system to 77 K.

At 77 K the throughput was checked again. The LN_2 was removed from the main bath and either stored in a 100 l dewar (ASU system) or transferred to the LN_2 jacket (UO system). The main bath was then pumped out to insure that all the nitrogen gas was removed. This process was done very slowly to avoid freezing the gas into a solid. The next step required filling the main bath with LHe. If solid N_2 remained it would boil off any LHe transferred into the main bath and prevent the bath from cooling. Once the system cooled to just above 4.2 K, the IVC was pumped out. After the system reached 4.2 K, the needle valve was opened and the 1 K pot was pumped on to further cool the system. First a small amount of mixture was released into the system and cooled, the ^{3}He closed cycle pump was turned on, and gradually all the mixture was released into the ^{3}He circulation path from the storage vessel. After approximately two hours the system reached a dynamic equilibrium at a base temperature. The entire cool down procedure typically took three days. The system could be kept in this mode for several weeks, limited mainly by the degradation of the OVC vacuum.

3.6 Instrumentation and Circuitry

Measurements were done in the near equilibrium and far from equilibrium regimes. Phenomena such as equilibrium conductance steps in QPCs and Coulomb blockade may be observed in the near equilibrium regime. Hot electron phenomena and transient phenomena may be observed in the far from equilibrium regime. At the UO data acquisition was controlled by C programs over a GPIB bus. LABVIEW programs in tandem with a data acquisition board (DAQ) were used at ASU. Several small discrete circuits were necessary to achieve the desired biasing configurations. Eight voltage dividers were built for the gates and two voltage dividers for the source/drain. An existing current divider was adapted for use with the source/drain.

3.6.1 Equilibrium Setup

To achieve near equilibrium conditions a small source/drain bias must be applied to the device so that the electrons are not heated significantly above the lattice temperature, and the bias is not larger than the energy level separation which is being observed. Under these small biases noise sources can easily obscure the signal. In order to increase the signal to noise ratio, phase sensitive detection was used. With phase sensitive detection an A.C. source signal is output at a certain frequency, and the detected signal is referenced to the source frequency. A lock-in amplifier (LIA) will filter out all frequencies other than the reference frequency when detecting a signal. Usually low frequencies with values of prime numbers are used to avoid coupling of high frequency signals and power line harmonics.

Near equilibrium measurements were done with two Stanford Research SR830 LIAs. At temperatures under 100 mK a source drain bias of approximately 10 μK or less was needed to preserve near equilibrium conditions. This small voltage was obtained by using the A.C. output voltage provided by the SR830 and a 3000x voltage divider. The output had an amplitude range of 4 mV to 2 V with a step size of 2 mV and a frequency range of 0 to 100 kHz with a .001 Hz step size. The voltage divider circuit was accurate when the device resistance was high (high gate bias applied). However, when the device resistance was low (no or small gate bias applied) a current source/divider proved more accurate than the voltage divider. Circuit diagrams of the two types of dividers used are shown in Fig. 3.14. The SR830 detected the current or voltage signal respectively and sent the information to the computer via a GPIB bus or the DAQ. In addition the SR830 had 4 programmable DC output voltage sources which were used as the gate voltage sources. The SR830 DC outputs had a range of +10.5 V to -10.5 V and a minimum step size of 1 mV. Voltage dividers were used to achieve a smaller step size and to further reduce voltage supply noise.

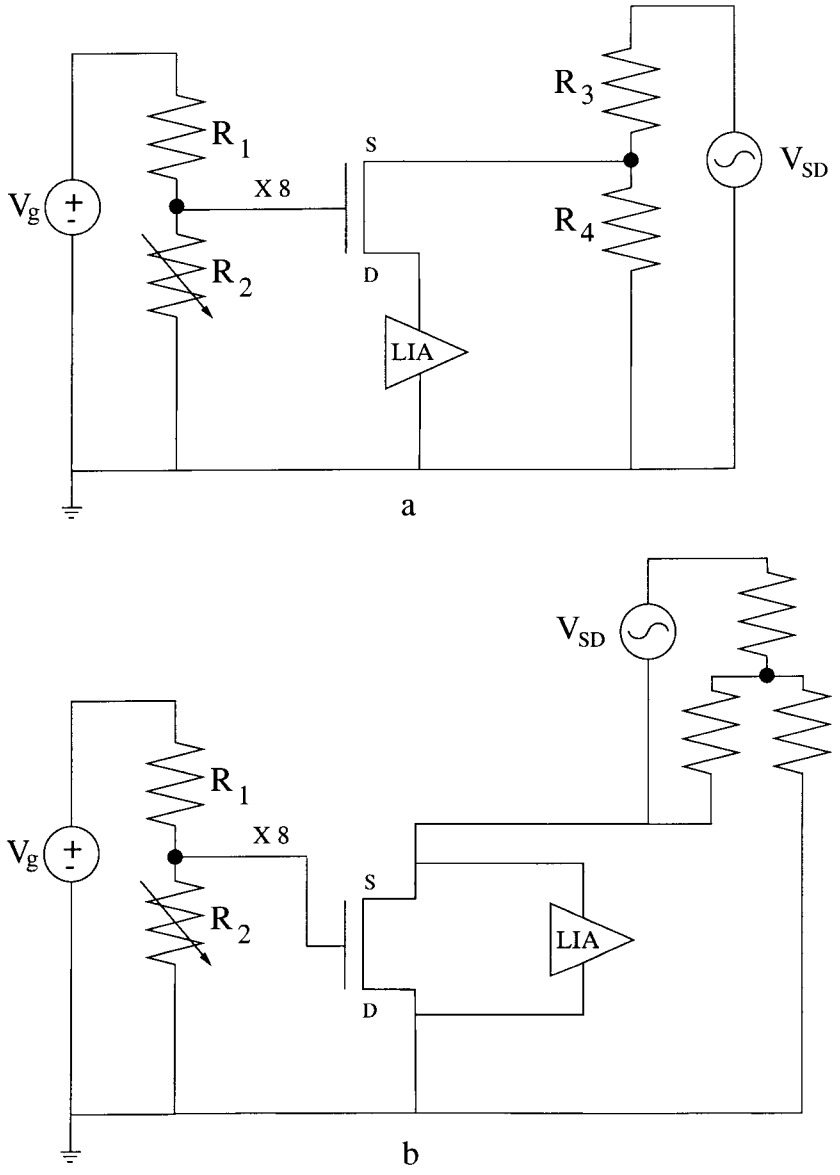

Figure 3.14: Schematic of the equilibrium measurement circuit. (a) A voltage divider for the source and drain. (b) A current divider for the source and drain.

3.6.2 Far from Equilibrium Setup

In the far from equilibrium regime a D.C. source was applied to the source/drain with a Keithley 236 source measurement unit (SMU). The SMU can source a current (voltage) and measures a voltage (current) simultaneously. In the I-V measurements, a current source was applied and a voltage was measured. The SMU had a voltage offset which tended to float over time preventing accurate measurements below approximately 1 mV. The current could be swept linearly with minimum steps of 10 fA or logarithmically with up to 50 points per decade. Ideally the triax cables available on the Keithley can provide excellent noise shielding. However, due to the wiring of the cryostats, the triax cable could not be used and a box had to be built to convert the triax connections to the coax connections on the cryostats. The signals detected in the far from equilibrium regime were large enough that the signal to noise ratio was sufficient. A circuit diagram is shown in Fig. 3.15.

3.6.3 Extra Filtering

In addition to the circuitry described above, filters were used at the top of the cryostats to filter static discharges which occurred when attaching the coaxial cables. At the UO homemade ferrite ring filters were used. A toroidal ring made of nickel-zinc with a permeability of 125 mu and A_L value of 55.3 $mH/1000$ turns was wrapped with copper wire to achieve an inductance of approximately 2 mH. The lead resistance of the cryostat wires was approximately 200Ω. Therefore when the device resistance was low (approximately 2 $k\Omega$) signals above 160 kHz were attenuated and when the device resistance was high (approximately 12 $k\Omega$) signals above 1 MHz were attenuated. Although a signal conditioner was applied to the power supply lines, radio frequency signals in the range of a few hundred kHz were present on the line which created undesirable noise and were a potential source of electron heating.

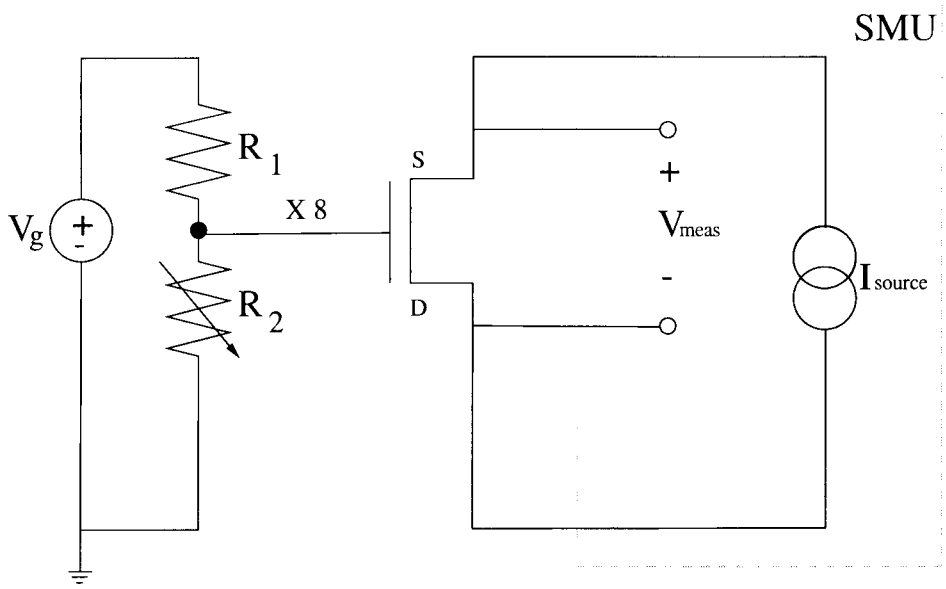

Figure 3.15: Schematic of the circuit used to measure the far from equilibrium I-V characteristics.

At ASU, Π filters provided by Oxford Instruments Inc. were used and filtered out signals above 1 MHz. Line noise was not sufficiently suppressed by a signal conditioner, so the third terminals of all instruments were tied to a copper plate in order to provide additional grounding.

The noise created by other instruments in the laboratory and building can be a danger to device performance and can even destroy devices sensitive to electrostatic discharge. Even with the high frequency filters, a device can be destroyed by a power surge. Usually "isolated" power supply lines are wired up in the laboratory, signal conditioners are used, common grounding is imperative, and then extra filters are used at the top of the cryostats. The ultimate line noise floor will be related to how well the building is grounded to earth, which will depend on the geology of the area. In the case of poor earth grounds (low salinity, dry soil), an artificial chemical ground for the building can be established.

4. NEAR EQUILIBRIUM TRANSPORT IN ALGAAS/GAAS QUANTUM DOTS

This chapter describes the near equilibrium characteristics of the quantum dots and QPCs studied. Samples were initially measured at 1.2 K in the 1 K transportable system, described in Chapter 3, to check for stability in the source and drain contacts and for pinch off of the 2DEG by the surface gates. Then the samples were cooled to millikelvin temperatures in a dilution refrigerator system. Near equilibrium measurements were performed on each gate of every device in order to determine the characteristics of the 1D QPCs, ascertain whether a quantum dot could be formed which showed Coulomb blockade behavior, and establish operating points (gate biases) in order to perform the nonequilibrium measurements described in Chapter 5.

The first section of Chapter 4 will examine the near equilibrium characteristics of the MOCVD material studied. Drift behavior observed in the MOCVD material prevented its use in observing quantum effects and nonequilibrium behavior. For these applications MBE material was employed. The second and third sections will detail the near equilibrium conductance of the QPCs and quantum dots fabricated on MBE material. In these structures clear 1D behavior was observed in the QPCs, and Coulomb blockade behavior was observed in the dots. The last section details magnetoconductance measurements which were performed on a coupled QPC and quantum dot system. Unusual jumps in the conductance of the QPC were observed under certain gate biases and magnetic fields. The self-consistent potential created by the gate biasing and magnetic field may induce charging of a single impurity located in or near the QPC, or switching may be due to tunneling between edge states.

4.1 MOCVD Near Equilibrium Characteristics

An overview of the near equilibrium characteristics of the MOCVD material is given below. First, the 1D conductance of the QPCs is summarized and then the conductance of the quantum dots is discussed.

4.1.1 1D Conductance in the QPCs

A first set of devices was fabricated on MOCVD material from Sandia National Laboratories with the layer structure shown in Fig. 3.2. Two devices survived electrostatic discharge and were cooled below 1.2 K. Results of the near equilibrium measurements were discouraging. The QPC characteristics did not show clear conductance steps in general. The QPC conductance curve which most closely resembled the ideal 1D conductance steps is shown in Fig. 4.1. Although there is a clear distinction between depletion of the 2DEG and the onset of 1D behavior at approximately -.7 V, there are no clear conductance steps. In many of the QPCs there is no clear distinction between the 2D and 1D conductance.

One possible explanation for the poor conductance characteristics involves the geometry of the constriction. Haanappel and van der Marel [119] consider the particle flux incident on the QPC and solve the Hamiltonian using a tight binding method. According to their theoretical calculations there is an optimum ratio of the length, L_{opt}, to the width, W, of the constriction given by

$$L_{opt} = .4W\lambda_F \tag{4.1}$$

where λ_F is the Fermi wave vector. For the MOCVD device,

$$L_{opt} = 20 - 25\, nm. \tag{4.2}$$

It is possible that once the 2DEG (which is at approximately 100 nm below the surface) is depleted, the constriction becomes too short and conductance steps are not observed. However, even in the QPCs with larger spacing, no clear conductance

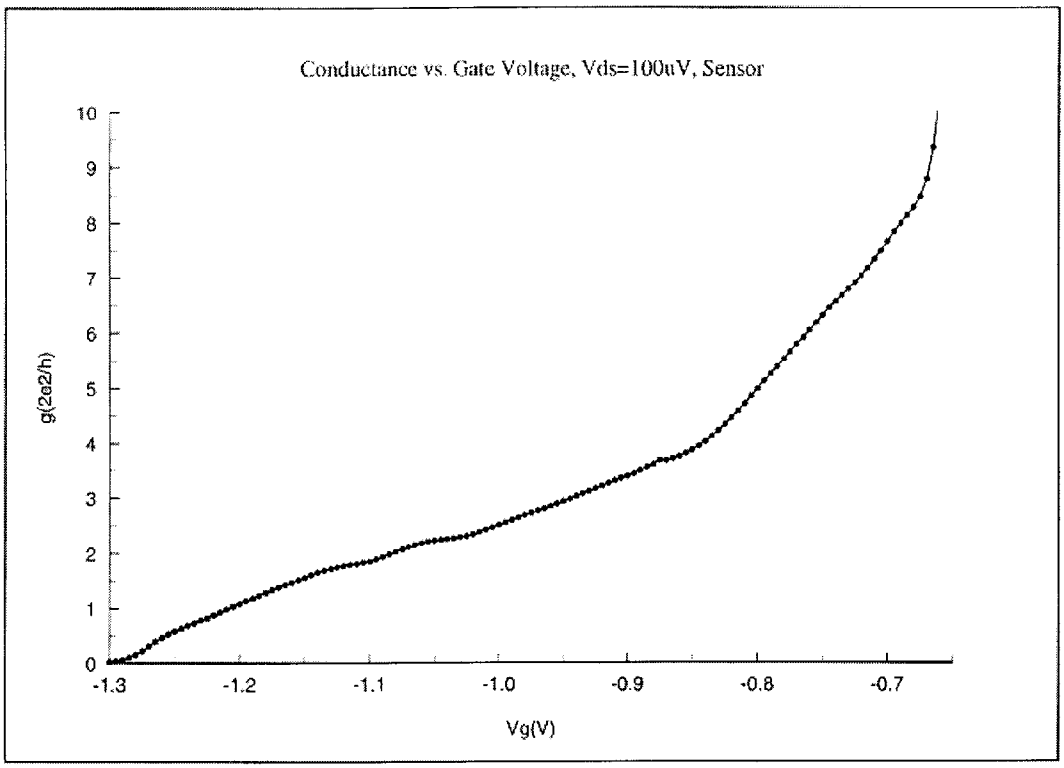

Figure 4.1: Example of the near equilibrium conductance of a QPC vs. gate voltage observed on the MOCVD material.

steps are observed.

Another explanation for the poor characteristics is that impurity scattering in or near the constriction suppresses the conductance plateaus. Haanappel and van der Marel [119], Chu and Sorbello [120] have demonstrated this theoretically by treating the channel as an electron waveguide and the impurity as a scatterer.

4.1.2 Coulomb Blockade in the Quantum Dots

It is not clear that suppression of the 1D conductance plateaus in the characteristics of the QPCs which form the dot will prevent the observation of Coulomb blockade oscillations. However, after systematic and exhaustive searches, no region of gate bias was found to produce Coulomb blockade oscillations. Instead of Coulomb blockade oscillations, an unexpected phenomena was seen. Fig. 4.2 shows

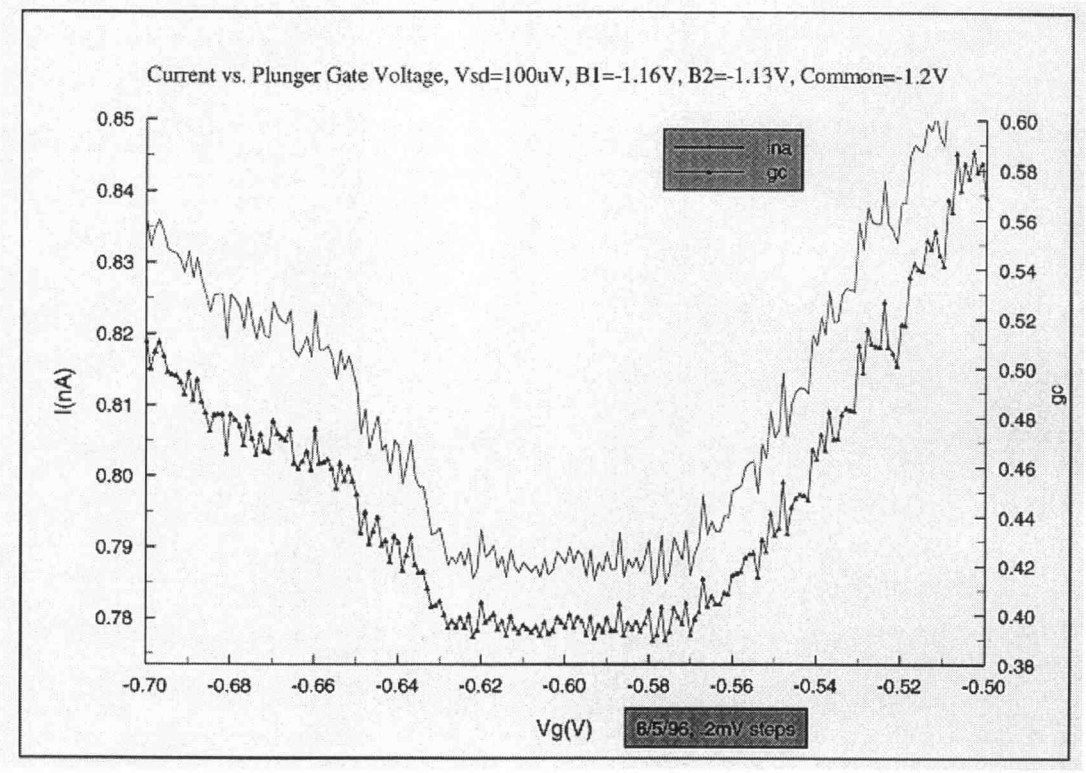

Figure 4.2: Example of near equilibrium conductance in the CB regime on the MOCVD material. The left y axis is current represented by the single line and the right y axis is conductance in units of uS represented by the line with dots. The x axis represents plunger gate voltage.

a typical conductance sweep for a single dot. The gates defining the input and output barriers to the dot were fixed and the plunger gate was swept. As the gate voltage on the plunger was made more negative, the current initially decreased as the dot pinched off, and then it remarkably began to increase! Instead of oscillations, a steady increase in current was seen after the plunger gate bias reached -.62 V. The current appeared to be changing as a function of time, rather than as a function of plunger gate voltage.

The time dependent QPC characteristics were then investigated. The gate bias was fixed and the current through the constriction was sampled over time. The current changed significantly over a period of an hour as shown in Fig. 4.3. This

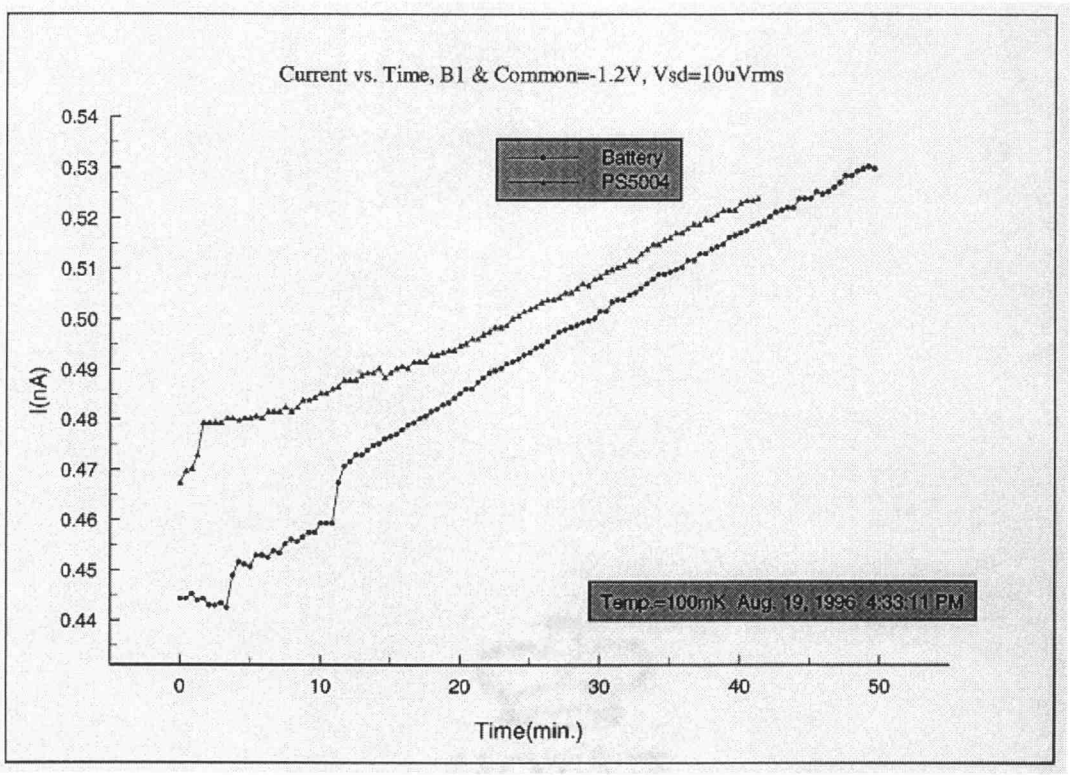

Figure 4.3: Time dependent conductance of the QPCs in the MOCVD material.

behavior was seen in other MOCVD samples and had been seen previously by J. Wu *et al.* [121] and was attributed to impurity charging.

These impurities are expected to be distant from the 2DEG in the z direction (growth direction as defined in Chapter 2) due to the high electron mobility in the 2DEG. Perhaps they are DX centers (see Appendix A) which are spatially separate from the 2DEG. As impurities charge or discharge over time the potential profile in the 2DEG changes. An initial gate bias will produce a field which causes impurity charging. If there are many impurities which are charging and discharging, more time will be required for the potential profile in the 2DEG to reach equilibrium after a gate voltage is applied. Additionally, at low temperatures charging is considerably slower than at room temperature. Thus the conductance characteristics are seen to drift over time as the impurity configuration and applied electric field

reach an equilibrium state. The unusual drift behavior combined with the poor QPC conductance characteristics indicate that impurities have a significant effect on the electron transport of these samples. Coulomb blockade sweeps can take several hours, thus the probability of observing Coulomb blockade behavior or other quantum phenomena was severely diminished. Therefore, no other experiments were attempted on MOCVD material.

4.2 MBE Near Equilibrium Characteristics

An overview of the near equilibrium characteristics of devices on the MBE material is give below. First the 1D conductance of the QPCs and the conductance of the quantum dots is discussed and then the observed experimental behavior is compared to theoretical predictions.s

4.2.1 1D Conductance in the QPCs

Six pieces of MBE material with the layer structure shown in Fig. 3.2 were subsequently obtained from Sandia National Laboratories ,and five devices were successfully fabricated on these chips, one device per chip. Two devices, one on sample G1423B and one on sample G1135B exhibited good near equilibrium behavior. In these samples there was always a clear delineation between 2D and 1D behavior. The 2DEG was seen to deplete between -0.4 V and -0.5 V, and pinch off occurred between -0.6 V and -1.0 V. Conductance steps were clearly observed in the QPCs. Some steps were quite sharp as shown in Fig. 4.4, while others were slightly washed out.

4.2.2 Coulomb Blockade in the Quantum Dots

Once the near equilibrium characteristics of the 1D QPCs are established, the appropriate gate biases needed to observe CB can be determined. Referring to

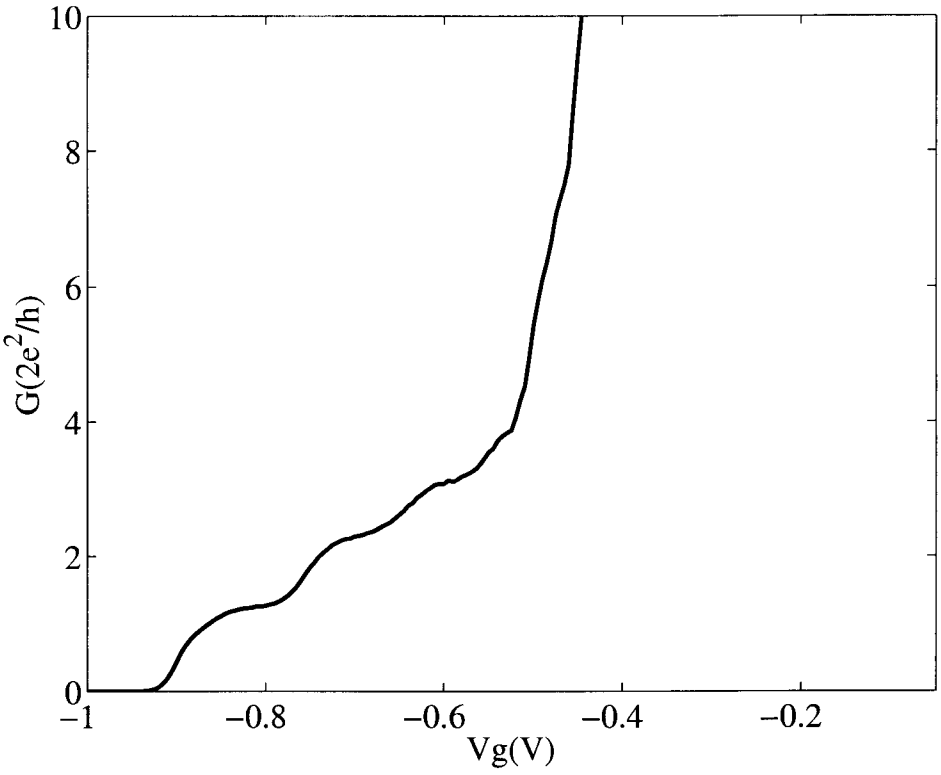

Figure 4.4: Example of the near equilibrium conductance observed in the QPCs of sample G1423B. Four conductance steps are evident.

Fig. 3.9, barriers 1 and 2 together with the common gate comprise the input and output barriers to the dot. The conductance of these QPCs must be much less than e^2/h ($R > 25\ k\Omega$), as discussed in Chapter 2, in order to observe CB oscillations. Once the QPC biases are set, a bias can be applied to the plunger gate in order to form the dot and vary its size (and number of electrons). Due to the small size of the dots (approximately 400 nm^2 as defined lithographically), the plunger gate bias affects the potential, and therefore the conductance, in the QPCs. Thus the conductance of the QPCs was set at approximately $2e^2/h$ with the plunger gate grounded. As the plunger gate was swept from zero to a negative voltage, the dot formed and the conductance of the QPCs fell to well below $e^2/4h$.

One dot in both samples exhibited CB oscillations which are shown in Fig.

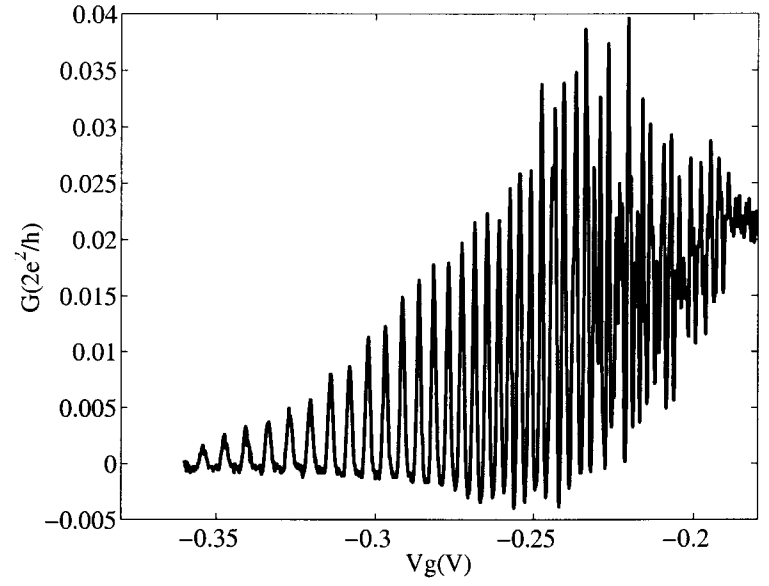

a

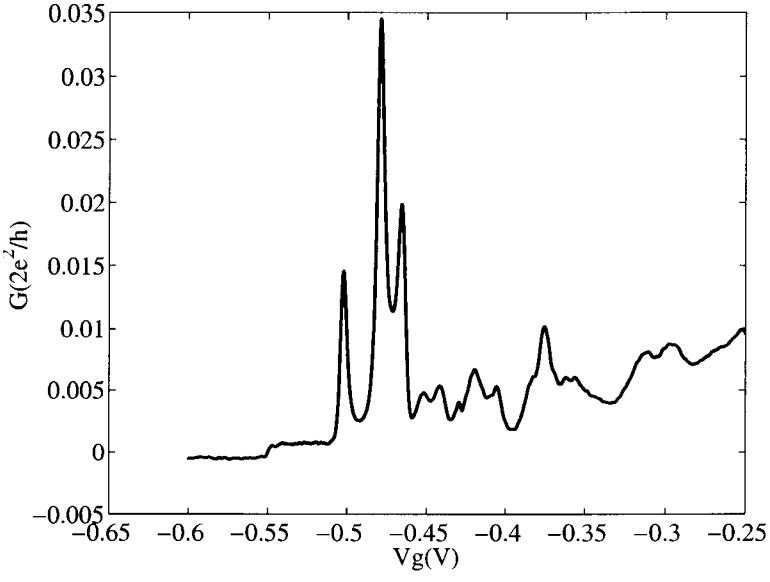

b

Figure 4.5: Coulomb blockade oscillations observed in dot#1 of (a) sample G1423B and (b) sample G1135B.

4.5. The oscillations in sample G1423B are quite periodic with increasing spacing as the gate voltage is made more negative. The peak heights below -0.25 V follow an envelope function. There appears to be a decreasing background conductance at gate voltages above -0.25 V which goes away below -0.25 V so that in between the peaks the conductance goes to zero. In theory the conductance should not be negative as seen at $V_g \sim -0.25\,V$. It is possible that there is some type of offset voltage in the measurement circuit which creates a negative reading.

The oscillations in sample G1135B are not quite as periodic as those in sample G1423B. The peak heights vary dramatically and do not follow an envelope function. Sample G1135B also exhibits a decreasing background conductance which does not go away until -0.55 V at which point no more peaks are visible.

4.2.3 Theory and Analysis of the QPC Conductance Steps

In the Landauer-Büttiker (L-B) formalism referred to in Chapter 2 under finite temperatures the expression for the total current from left to right is the current injected from the left minus the current injected from the right. The incremental current injected from a channel n of incremental energy in one contact to channel n in the other contact (assume no intermode scattering) is [6]

$$I_n dE = \frac{2e}{h} T_n(E)\,[f(E-\mu_l)dE - f(E-\mu_r)dE] \tag{4.3}$$

and the total current is

$$I = \frac{2e}{h} \int_{-\infty}^{\infty} dE \sum n T_n(E)\,[f(E-\mu_l)dE - f(E-\mu_r)dE] \tag{4.4}$$

For cryogenic temperatures we can assume that $T = 0\ K$. Then the Fermi-Dirac distributions become step functions, and the expression for the current can be simplified to,

$$I = \frac{2e}{h} \sum n \int_{0}^{\mu_l} dE T_n(E) - \int_{-eV_{sd}}^{\mu_r} dE T_n(E). \tag{4.5}$$

In the limit of a small applied bias (near equilibrium conditions as discussed in Chapter 2) and unity transmission this reduces to the formula given in Chapter 2,

$$I = \frac{2e}{h} N e V_{sd}. \tag{4.6}$$

Note that the step edges in Fig. 4.4 are not sharp as in the schematic predicted by the simple theory (Fig. 2.2). Assuming impurity scattering does not contribute to the rounding of the step edges, the deviation from the simple theory can be attributed to two factors. One factor is that at finite temperatures the Fermi-Dirac distribution is not a step function. However, the experiments were performed under millikelvin temperatures, and the Fermi-Dirac distribution is not expected to deviate significantly from a step function at these temperatures. A second factor, which is more likely to cause rounding of the step edges, is the actual form of the transmission coefficient, which is not unity.

As mentioned in Chapter 2, the transmission coefficient is a function of the potential profile in the quantum point contact. The potential in a QPC has alternately been treated in the literature as a hard wall potential, a harmonic oscillator potential, and a saddle point potential in theoretical calculations [6]. One model which gives a reasonably accurate representation is a saddle point potential, which is considered here. The transmission coefficient for motion in the x direction has been calculated for a saddle point potential by Fertig and Halperin, Miller, and Connor [122, 123, 124], and employed by Büttiker [125] to describe transport through a QPC.

$$T_{mn}(E) = \delta_{mn} \frac{1}{1 + exp^{-\beta(E - \frac{\hbar}{2\pi}\omega_y(n+\frac{1}{2}) - e\phi_o)}} \tag{4.7}$$

$$\beta = \frac{2}{\hbar\omega_x} \tag{4.8}$$

where ϕ_o is the barrier height of the saddle point potential, $\hbar\omega_y$ is the energy level spacing above the barrier height in the y direction (direction perpendicular to electron transport), and $\hbar\omega_x$ relates to the curvature below the barrier height in the x

direction. A larger value of $\hbar\omega$ corresponds to a narrower constriction or curvature. Under near equilibrium biases the potential profile can be calculated numerically and a value for ϕ_o and $\hbar\omega_y$ can be obtained. A program written by Prof. D. Vasileska of Arizona State University which solves the 3D Poisson and 1D Shrödinger equations self-consistently was used to characterize the near equilibrium potential profile for the devices used in this research. A description of the numerical techniques and physical assumptions made in the program is given in Appendix B. Figure 4.6 displays the results of the simulation for one QPC biased at -0.9 V with approxi-

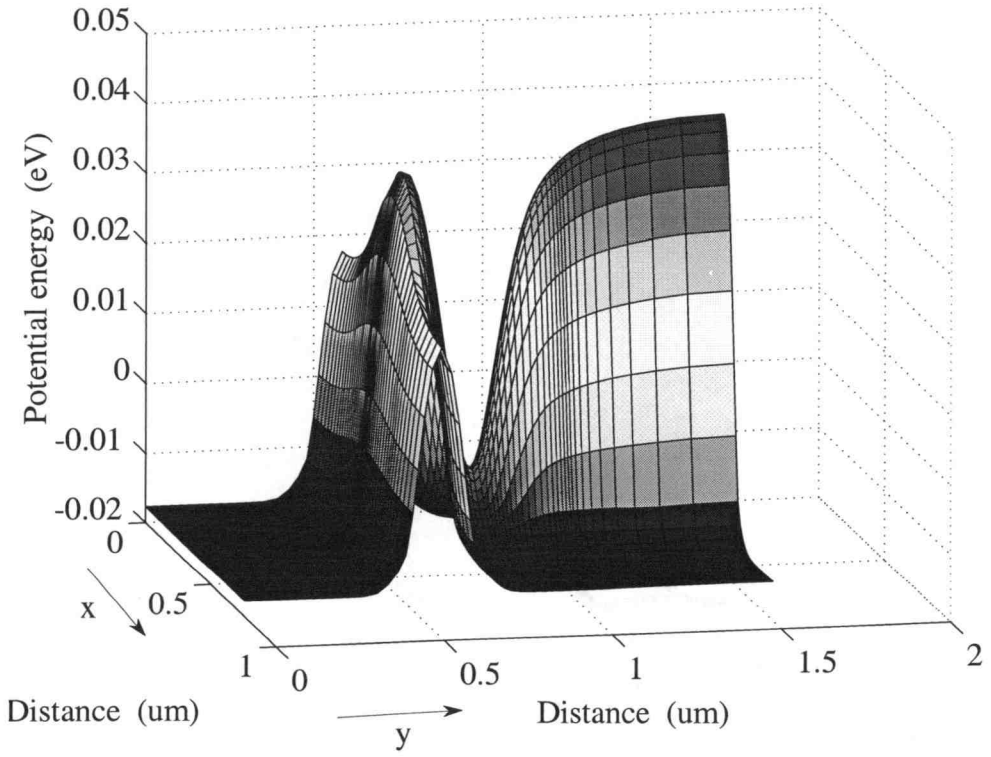

Figure 4.6: Potential profile of the saddle point potential in the QPC constriction.

mately two modes conducting. With this gate biasing, the barrier height is 5 meV below the Fermi energy in the reservoirs and 3 meV above the lowest energy level in the 2DEG, which is 8 meV below the Fermi energy, as calculated with the 1D

Schrödinger-3D Poisson solver. A fit to the parabolic curve of the potential above ϕ_o yields an energy spacing in the constriction of $\hbar\omega_y \sim 2meV$. Therefore, two modes are below the Fermi energy in the reservoirs. In the example shown in Fig. 4.4, the QPC pinched off at -0.9 V which means that no modes are conducting. At -0.7 V in Fig. 4.4, two modes are conducting. This offset of approximately -0.2 V is commonly observed in these simulations [126]. The program does not consider random impurities which may change the background potential and therefore the voltage at which the channel pinches off. The program does model well the gate voltage at which depletion of the 2DEG occurs (see Appendix B). The curvature of the bottom portion of the saddle point potential in the x direction was not fit and in the extended L-B theory (Chapter 5) was used as a fit parameter. However, the curvature in the x direction is much broader than that in the y direction, thus a reasonable choice for $\hbar\omega_x$ must be less than $\hbar\omega_y$.

4.2.4 Analysis of the Periodicity of the CB Oscillations

In Fig. 4.5 the periodicity of the CB peaks of sample G1423B increase as the plunger gate is made more negative. This is because the plunger gate decreases the size of the dot which decreases the capacitance and in turn increases the charging energy. The oscillations in sample G1135B are not quite as periodic which suggests that the energy level structure plays a role in the charging energy of the dot. The peak height variations are theorized to be due to the energy level structure as well [127]. The transmission coefficient varies as the electrons tunnel through different energy levels, thus the peak height changes.

In Fig. 4.5 the oscillations are shown as a function of the plunger gate voltage. The period of the oscillations in gate voltage is proportional to the gate capacitance. Thus an estimate of the total dot capacitance can be determined by varying each gate separately, determining the oscillation period and individual gate capacitances, and

Table 4.1: Estimate of gate capacitances and dot radii from experiment.

Gate	Period (mV)	Capacitance (aF)
G1423B P1	6	27
G1423B B1	8	20
G1423B B2	10	16
G1423B Common	2	80
G1135B P1	15.6	10.25
G1135B B1	9.5	17
G1135B B2	7.6	21
G1135B Common	4	40
Sample	Total Cap. (aF)	Dot Radius (nm)
G1423B	143	155
G1135B	88	95

adding them together. Then an estimate of the dot radius can be made by setting $C_{tot} = 8\epsilon R$ (see Chapter 2). This procedure was done for both samples and the results are shown in Table 4.1.

An estimate using the lithographic dimensions of the dot and including a depletion width of approximately 0.1 μm [128] around the gates for sample G1423B gives a dot with a radius of 150 nm. This value is in good agreement with the radius derived from the experiment, 155 nm. In sample G1135B the dot is slightly smaller lithographically. In addition the plunger gate must be made more negative to observe the CB oscillations, so the depletion width should be larger. For a depletion width of 0.2 μm and lithographic dimensions of 350×400 nm^2 the dot

radius would be 110 nm. Again this is in close agreement with the estimate of 95 nm from experiment.

4.2.5 Theory of the Line Shape of CB Peaks

Theoretical analysis of the shape of CB peaks have been made by Beenakker [32] and Meir, Wingreen, and Lee [129]. Solving a kinetic equation for the distribution functions including tunneling rates, Beenakker derived a generalized conductance given below,

$$G = \frac{e^2}{k_B T} \sum_{p=1}^{\infty} \sum_{N=1}^{\infty} \frac{\Gamma_p^l \Gamma_p^r}{\Gamma_p^l + \Gamma_p^r} P_{eq}\left(N, n_p = 1\right) \times \left[1 - f\left(E_p + U(N) - U(N-1) - E_F\right)\right]. \tag{4.9}$$

P_{eq} is the equilibrium probability distribution (Gibbs distribution) in the grand canonical ensemble, $f(E)$ is the Fermi-Dirac distribution, Γ_p^l and Γ_p^r are the tunnel rates from level p in the dot to the left and right reservoirs respectively, E_F and E_p are the Fermi energies in the reservoirs and dot respectively, N is the number of electrons in the dot, $U(N) = (Ne)^2/2C_{dot}$ is the electrostatic energy, n_p is the occupation number of level p in the dot, and T is the electron temperature. The conductance is for near equilibrium current through a quantum dot represented by the circuit diagram of Fig. 2.8. It has been assumed in this derivation that the energy level spacing and thermal energy are much larger than the uncertainty in the energy levels, $\Delta E, k_B T \gg h\Gamma$. This implies that $G \ll e^2/h$ which is the case in the experimental setup as discussed previously.

For the case of the classical regime where a continuum of energy levels is assumed in the dot, $\Delta E \ll k_B T \ll e^2/C$, and the generalized conductance can be simplified to the formula,

$$G/G_{max} = cosh^{-2}\left(\frac{\Delta_{min}}{2.5 k_B T}\right), \tag{4.10}$$

where

$$\Delta_{min} = e(C_g/C_{eq})(V_g^{res} - V_g). \tag{4.11}$$

C_g and V_g are the capacitance and voltage respectively of the gate which is being varied, C_{eq} is the total capacitance of the dot, and V_g^{res} is the resonant gate voltage.

In sample G1423B with a dot radius of 155 nm, the number of electrons in the dot is approximately 150. With a Fermi energy $E_F = 7.1\ meV$, the energy level spacing is $E_F/N = 47\ \mu eV$. For $T = 50\ mK$, $k_BT = 21\ \mu eV$ and $e^2/C_{eq} \gg \Delta E$. Using the simplified Beenakker formula to fit the experimental data allows a theoretical determination of the electron temperature. An example of fitting to the CB peaks of samples G1423B and G1135B using the formula for the classical regime is shown in Fig. 4.7. The background conductance has been subtracted off of the data from sample G1135B to make the fitting possible.

The electron temperatures obtained are T=980 mK and T=1.2 K for G1423B and G1135B respectively. However, it is unlikely that the electron temperature was truly around 1 K. Temperatures of 50 mK and 10 mK respectively were measured during the experiments by precision calibrated resistors on the dilution refrigerators which are connected to the sample via a copper heat sink. In addition, sufficient time was given for the substrate and electron gas to come to an equilibrium. Perhaps the fact that ΔE is on the same order of magnitude as the sample temperature means that these formulas can not be used and a more general formula, not derived by Beenakker in Ref. [32], must be used. However, other groups have made experiments on AlGaAs/GaAs quantum dots with similar sizes and energy level spacings and have obtained good fits with reasonable electron temperatures, generally $T_e \sim 100$ mK [73]. A more likely explanation for the discrepancy between the theory and the experiment is that the uncertainty in the energy levels in the dot, $h\Gamma$, is NOT much less than k_BT due to scattering in the dot (from impurities) as discussed in Ref. [32]. In metallic systems inelastic tunneling through virtual states have

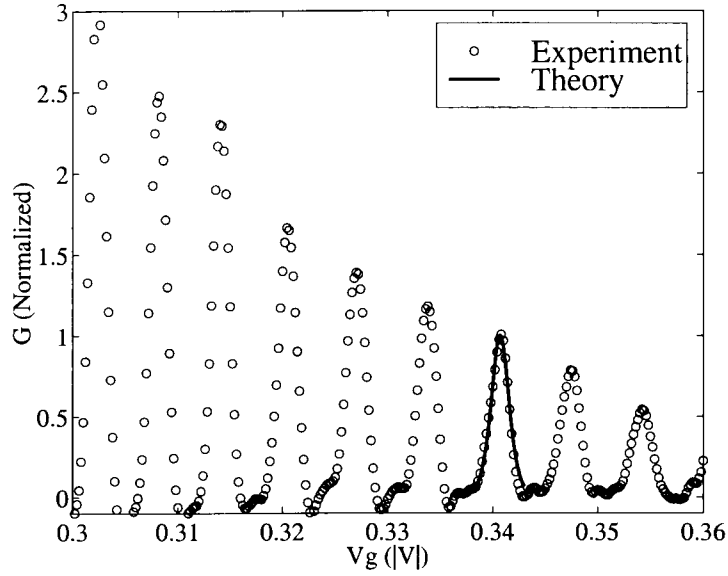

a

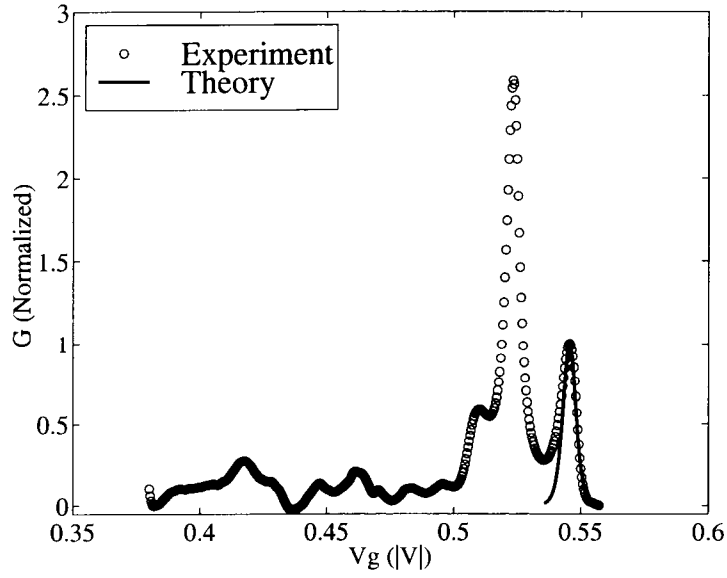

b

Figure 4.7: Theoretical fit using the formula developed by Beenakker (a) Dot1of sample G1423B (b) Dot# 1 of sample G1135B.

been demonstrated theoretically. Calculations show that at T=0 K and under CB conditions, residual conductivity will be present [130, 131]. These inelastic processes are most likely the cause of the broadening of the CB peaks, and therefore the simplified Beenakker formulas can not be applied to describe the line shape of the CB peaks observed in samples G1423B and G1135B.

Another attempt to fit the line shape of these CB peaks was made by using a Lorentzian fit in the form of a Breit-Wigner formula [6]. The Breit-Wigner formula has its roots in nuclear theory and was derived in connection with the decay of resonant states [132, 133]. The transmission through the resonant energy level is,

$$T(E) = \frac{{\Gamma_n}^2/4}{{\Gamma_n}^2/4 + (E - E_n)^2} \tag{4.12}$$

Where Γ_n is the full width at half maximum of the height (FWHM) and

$$(E - E_n)^2 = \left[\left(\frac{eC_g}{C_{eq}}\right)\left(V_f^{res} - V_g\right)\right]^2 \tag{4.13}$$

Fig. 4.8 shows the fit with the Breit-Wigner formula used for sample G1135B. From this theoretical fit a phase coherence time indicating the time between inelastic scattering events can be obtained and will be further discussed in Chapter 5.

4.2.6 Shifting Characteristics

Even in the MBE samples impurity charging affected the near equilibrium characteristics as evidenced by the shape of the CB peaks as well as repeated measurements of the Coulomb blockade peaks. After several hours the characteristics in sample G1423B changed suddenly as depicted in Fig. 4.9a. Figure 4.9b is an overlay of the characteristics before and after the sudden change and shows that oscillations still exist, but a background current appears to wash out the peaks. There seems to be an extra conduction path which creates the increased current. Possible sources are gate leakage, or parallel conduction through the substrate or surface.

A check for gate leakage was performed by connecting a large resistance (10

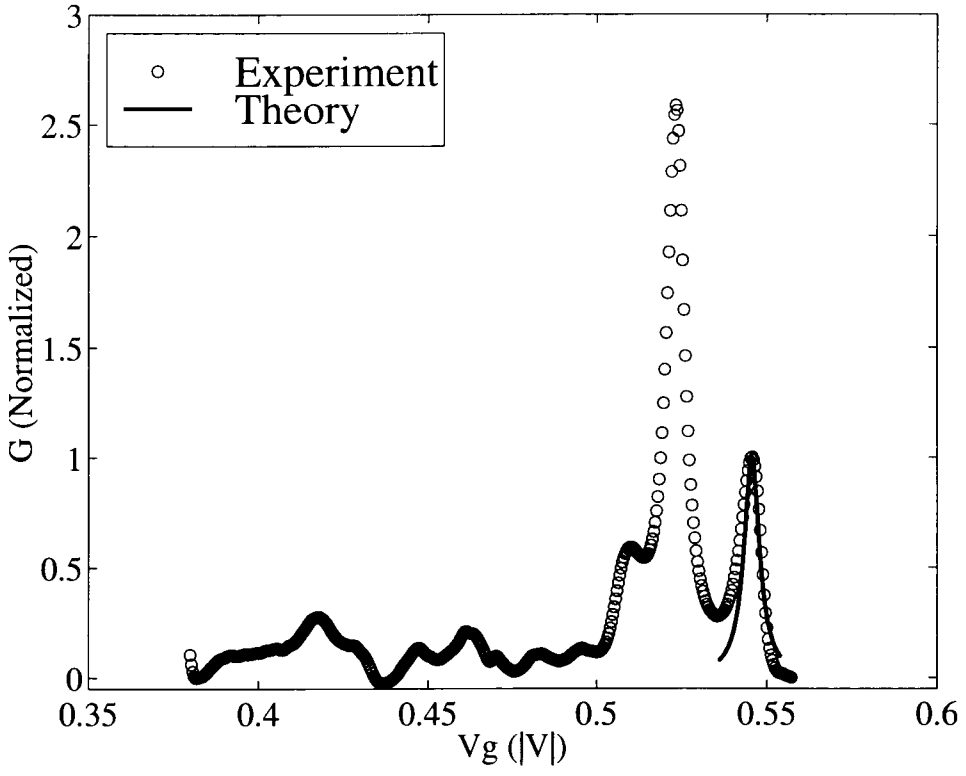

Figure 4.8: Theoretical fit using the Breit-Wigner formula on dot# 1 of sample G1135B.

$M\Omega$) in series with the gate, applying a voltage to the gate, and measuring any current flow by sensing a voltage across the large resistor. No gate leakage was observed, and all signals were much less than 1 pA, which corresponds to a conductance of $\sim .01e^2/h$. Increased substrate conduction should increase the gate voltage needed to pinch off the current. Since the gates still pinched off at approximately the same gate voltage before and after the CB oscillations changed, substrate conduction is unlikely. Surface conduction is unlikely because carriers in the surface layer should have been frozen out upon the initial slow cooling process. If they had not been, gate leakage would also be expected.

The most probable explanation is that an impurity in or near the dot changed its charge state and caused sufficient disorder in the dot to weaken the CB oscilla-

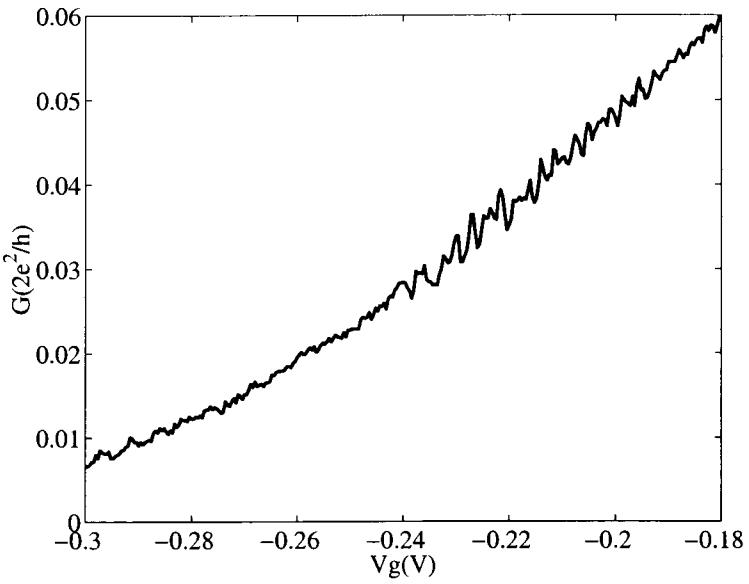

a

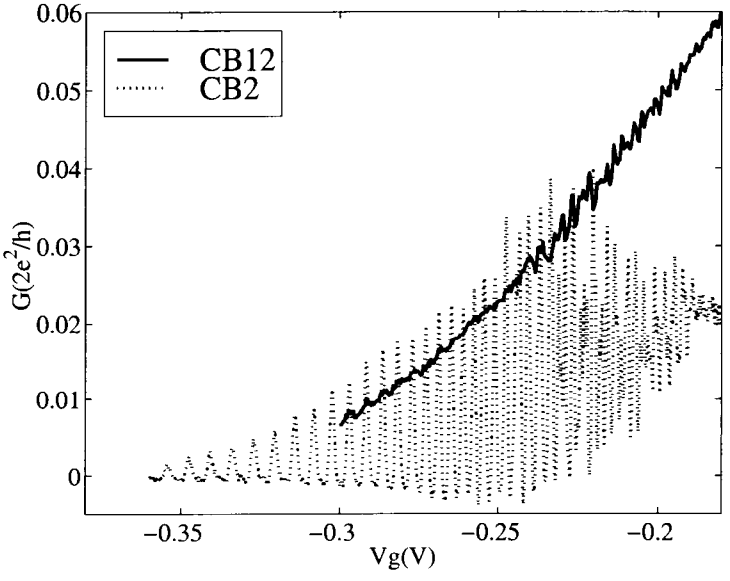

b

Figure 4.9: (a) Change in CB oscillations observed in sample G1423B. (b) Comparison of the CB oscillations observed in dot# 1 of sample G1423B.

tions. Calculations by M. Stopa [127], suggest that a disordered ionic background can break up the energy level structure and therefore wash out CB peaks. While this would limit the ability to do near equilibrium experiments concerning single electron phenomena, it would not necessarily limit nonequilibrium measurements which are not based on single electron charging or quantum interference effects. Remaining measurements on device G1423B were limited to the far from equilibrium regime. CB peaks observed in sample G1135B were stable over time, therefore this sample was used for further near equilibrium as well as nonequilibrium experiments.

4.3 Magnetoconductance of a Quantum Dot and QPC System.

Recently electron transport in open quantum dots where the tunneling to the leads is strong has been studied, and both experiments and theoretical calculations indicate that the discrete energy spectrum of the dots is resolved even in these open configurations [134]–[76]. Interference between the eigenstates of the dot creates spatially nonuniform current flow as predicted in calculations of wave function scarring [134]. In these calculations the electron wave function probability density in the dot takes on a pattern which resembles waves interfering in an agitated water tank. In experimental work under low magnetic fields ($< .5T$) magnetoconductance fluctuations have been observed which have a well defined periodicity [75]. These conductance fluctuations are thought to be correlated with the fluctuations of the electron probability density pattern in the dot. Detection and manipulation of these patterns and oscillations is a precursor to quantum computing.

With the quantum dot and QPC design of the devices studied here, near equilibrium magnetotransport measurements were performed on sample G1135B in an attempt to noninvasively detect these magnetoconductance fluctuations in the dot. First, zero magnetic field measurements were carried out to determine the QPC gate bias which would produce the most sensitive detection of the potential on the

dot.

4.3.1 Zero Field Measurements on a Closed Dot

Initial measurements with **B**= 0 T were performed with the dot biased in the CB regime and the QPC biased at approximately e^2/h or 20 $k\Omega$. In the right range of sensitivity, the QPC can detect the potential change on the dot when an electron is forced out of the dot with the plunger gate. Figure 4.10a shows a plot of the near equilibrium CB oscillations in the dot together with the near equilibrium conductance of the QPC. There are oscillations in the sensor which are of approximately the same periodicity as the oscillations in the dot, $\sim$ 6 mV, as determined by picking the peak positions and averaging over all the peak spacings. Even when oscillations in the dot are not visible, oscillations are still seen in the sensor, for instance at gate voltages above -0.4 V in Fig. 4.10a. In Fig. 4.10b, the conductance of the dot and sensor are shown as a function of the gate voltage on barrier 1. Oscillations in the dot are apparent only above -.53 V, but oscillations are seen in the sensor in the entire sweep range. This tells us we that can use the QPC as a sensitive probe of the potential dot as discussed in section 4.3.3.

4.3.2 Magnetoconductance of an Open Dot

The dot was then biased in an open mode so that tunneling was strong between the 2DEG reservoirs and the dot, the QPC was biased above one conductance step ($2e^2/h$), and the magnetic (**B**) field was swept from 0-5 T. The conductance of the dot and sensor are shown as a function of **B** field in Fig. 4.11a. Under low **B** fields the conductance fluctuations which are shared by the dot and QPC are SdH oscillations (see Chapter 2) due to the Landau levels in the 2DEG reservoirs. Contrary to our expectations no other correlated conductance fluctuations were observed under low **B** fields. It is not understood why.

Above .6 T Aharonov-Bohm (A-B) oscillations were observed with a period $\sim$

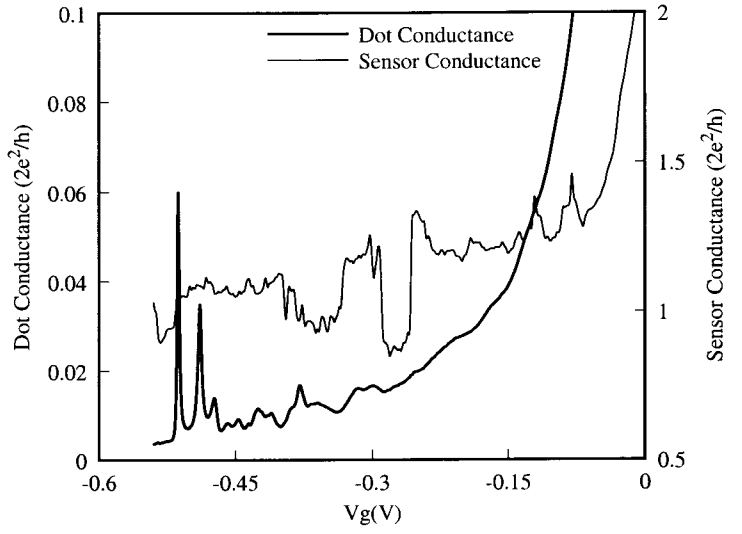

a

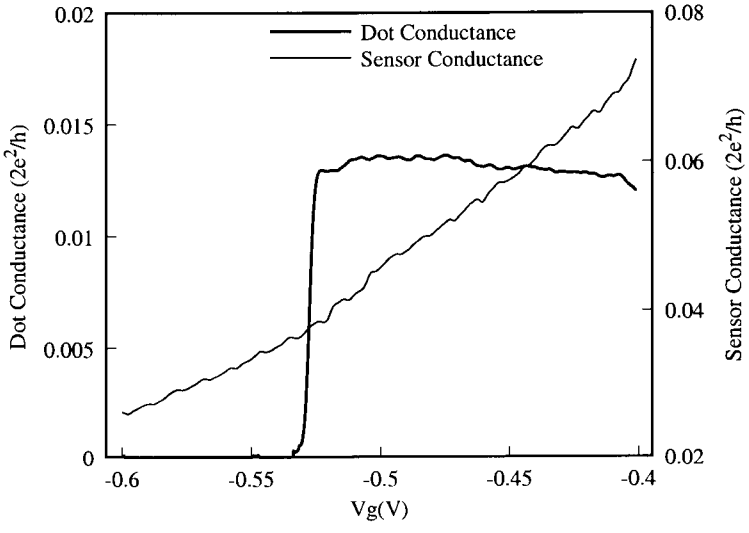

b

Figure 4.10: (a) CB oscillations in the dot and corresponding sensor conductance as a function of plunger gate bias. (b) CB oscillations in the dot and corresponding sensor conductance as a function of barrier 1 gate bias.

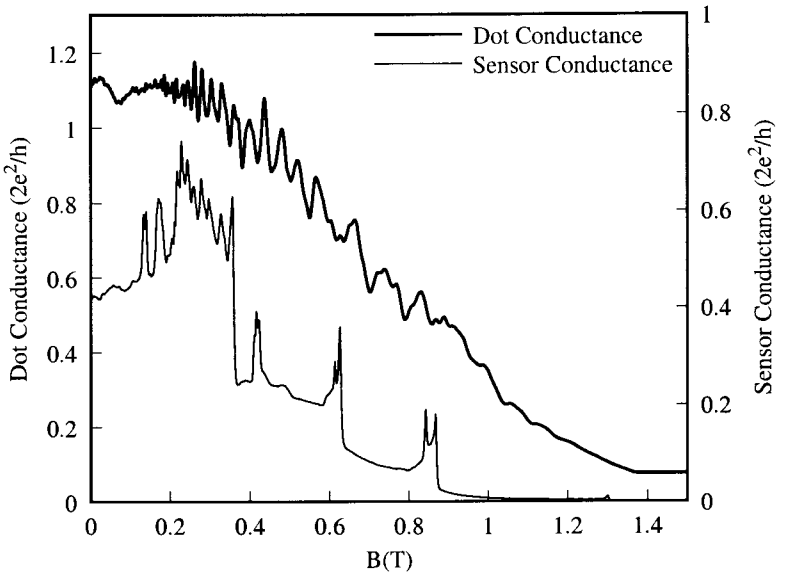

a

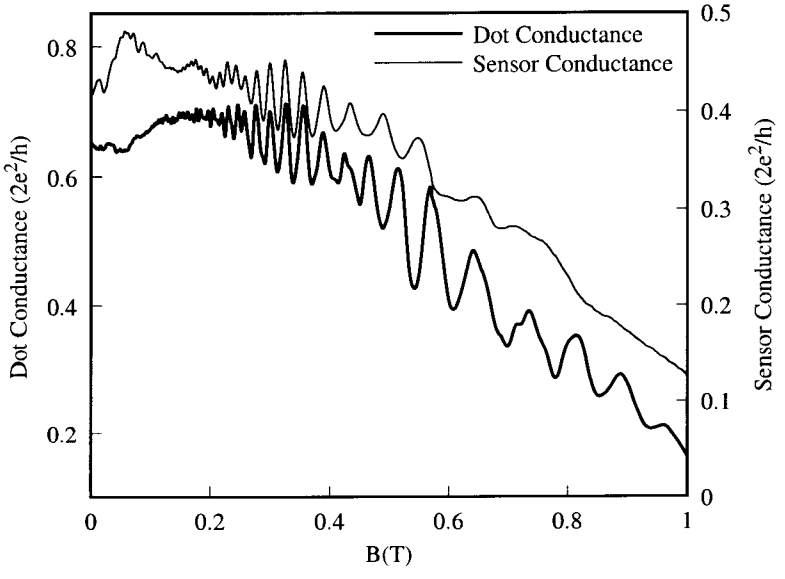

b

Figure 4.11: Magnetoconductance of the dot and sensor for an open dot $\sim e^2/h$ (a) and a closed dot $\sim 2e^2/h$.

40 mT, corresponding to a dot radius $\sim$ 180 nm. As expected, this is larger than the radius estimated from the gate capacitances when the dot was biased in the closed or weak tunneling regime, and is a reasonable estimate for the radius of the open dot. Two other striking features can be noted. Sudden jumps in the conductance of the dot were observed at **B**=.43 T, .63 T, and .85 T. These jumps occurred when the dot conductance was of integer and fractional quantum Hall plateaus ($1e^2/h$, $1.5e^2/h$, and $2e^2/h$). In addition, oscillations were seen in the *sensor* conductance which corresponded to A-B oscillations in the dot conductance. When the dot was closed somewhat by increasing the barrier heights and plunger bias so that the total conductance at zero field was $\sim 20\,k\Omega$ or $2e^2/h$, no switching was seen in this region of magnetic field as shown in Fig. 4.11b.

The sample was illuminated with a red LED in an attempt to increase the carrier density, screen out background potential fluctuations and improve the CB characteristics. The CB peaks did not become sharper, but were still stable. More **B** field measurements were made on the dot and QPC system. In Fig. 4.12, and Fig. 4.13 jumps are seen in the conductance of the QPC (after illumination) under higher magnetic field. This behavior was observed over time with all gate biases and the magnetic field fixed. Fig. 4.14a and Fig. 4.14b show sweeps for two different static magnetic fields. The switching time ranges from a few minutes to hours.

4.3.3 Discussion

The type of oscillations observed in the sensor at zero magnetic field were first observed by M. Field [13] and colleagues and subsequently by E. Buks [55] and coworkers in the "which path detector" circuit. As the potential on the dot changes with plunger bias, the electric field near the sensor changes. The conductance due to tunneling is very sensitive to this change in field and oscillations will appear on the sensor. The oscillations are on top of a background current which diminishes as

the plunger bias increases. This is consistent with the data presented by Field *et. al.* and Buks *et. al.* When the oscillations in the dot can no longer be measured any more due to the small conductance, electrons can still tunnel into and out of the dot and change the potential on the dot. The sensor QPC conductance is high enough to measure the oscillations in the tunneling resistance due to the near by potential change on the dot, and therefore oscillations persist in the sensor. The fact that oscillations are seen in the sensor when they can not be seen in the dot is also consistent with the previously observed data and indicates that the QPC is a very sensitive probe of the potential on the quantum dot.

In magnetic field sweeps performed on sample G1135B, above $.6T$ sensor conductance oscillations correspond to the A-B type oscillations in the dot. To our knowledge this is the first example of A-B oscillations observed with a voltage probe such as the sensor. The peaks and valleys of the A-B oscillations correspond to peaks and valleys in transmission or constructive and destructive interference of the electron waves. The oscillations in the QPC conductance are probably due to the average change in charge density and therefore Coulomb potential on the dot as the transmission oscillates with magnetic field.

Magnetic field sweeps also revealed unusual jumps in the conductance of the sensor at certain dot gate biases and magnetic fields. When observed over time the signal appeared to be a random telegraph signal (RTS) with different average switching times for different magnetic fields. RTS switching has been seen in single point contacts and is generally attributed to trapping by a single impurity [135]–[137],[87]. The time scale between switching or trapping events in these devices is usually on the order of a fraction of a second and in many cases can be observed when the conductance is above one conductance step. It is possible that these jumps are due to impurity charging. Under certain gate biases and magnetic fields a self consistent potential may develop which induces the impurity to change state.

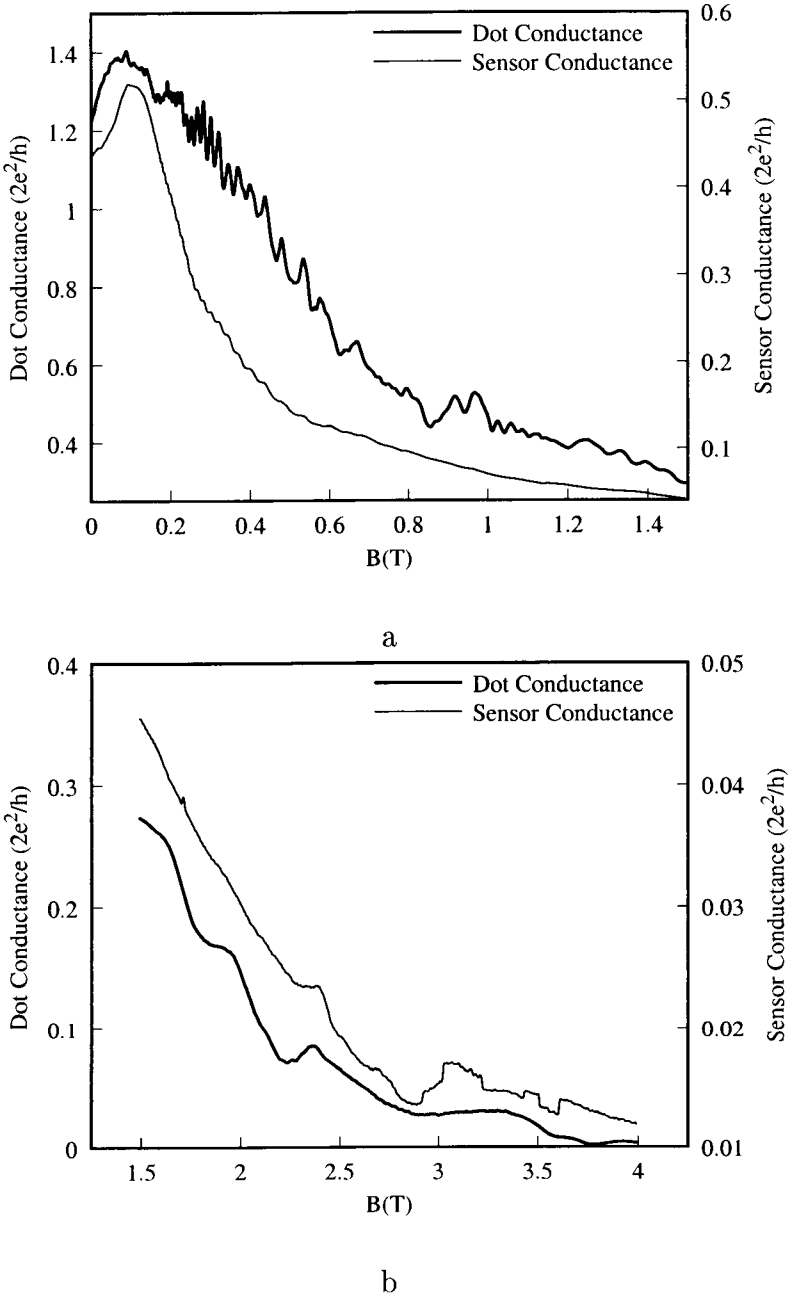

Figure 4.12: Magnetoconductance of the dot and sensor after illumination, dot= 10.5 $k\Omega \sim 2.46e^2/h$ and sensor= 28 $k\Omega \sim .92e^2/h$ at zero **B** field, (a) **B**= 0-1.5 T and (b) **B**= 1.5-4T.

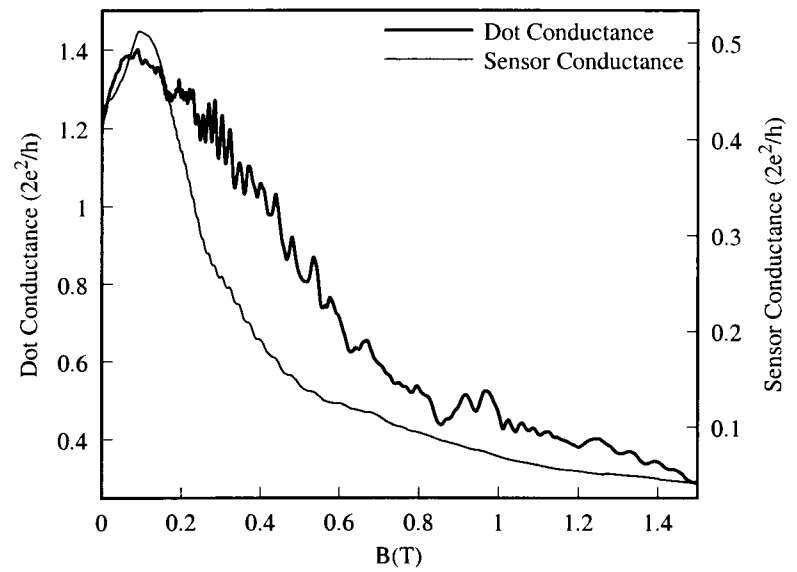

a

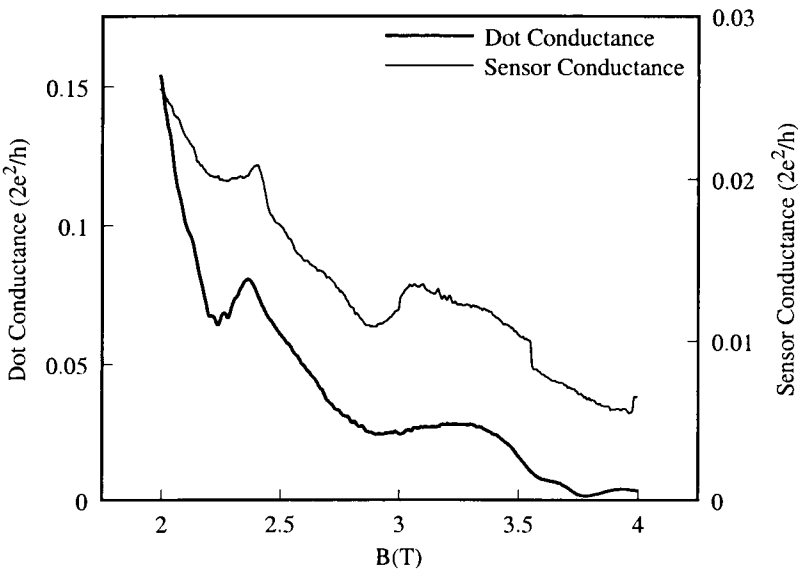

b

Figure 4.13: Magnetoconductance of the dot and sensor after illumination, dot= $10.5\,k\Omega \sim 2.46e^2/h$ and sensor= $30\,k\Omega \sim .86e^2/h$ at zero field, (a) $\mathbf{B}$= 0-2 T and (b) $\mathbf{B}$= 2-4T.

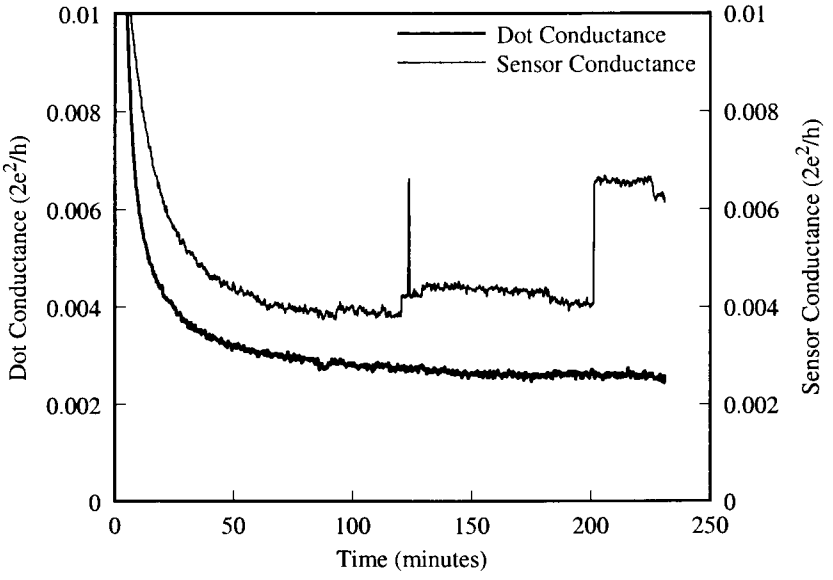

a

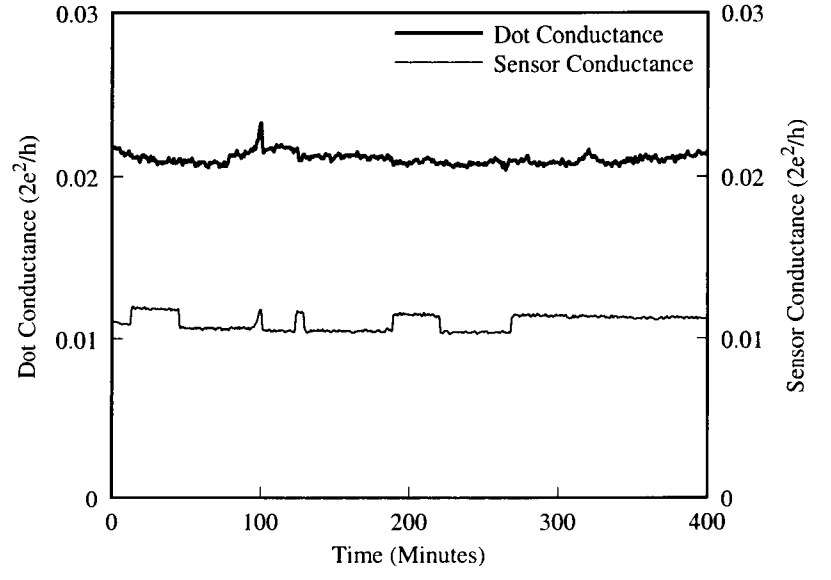

b

Figure 4.14: Magnetoconductance of the dot and sensor after illumination sampled over time, dot= 10.5 $k\Omega$, sensor= 30 $k\Omega$ at zero field, (a) $\mathbf{B}$=4 T and (b) $\mathbf{B}$=3 T.

However, the time scale of the switching seen in these samples is on the order of several minutes or longer and occurs only under higher magnetic fields and gate biasing when the conductance of the dot and sensor are well below a conductance step. Van der Vaart *et. al.* [138] and Bird *et. al.* [139] have published similar results and van der Vaart theorized that the switching is due to single electron tunneling between edge states in the dot. An interesting feature of these jumps is that they tend to occur when the dot conductance reaches certain integer and fractional quantum Hall plateaus. An understanding of this phenomena has not been reached at this time.

4.4 Summary and Conclusions

Impurity charging in the samples fabricated on MOCVD material made it virtually impossible to perform reliable experiments on these samples. All subsequent measurements were made on MBE material. Two devices fabricated on the MBE material showed good 1D conductance in the QPCs and Coulomb blockade behavior in the quantum dots. Impurity charging was still a factor in degradation of the near equilibrium characteristics in sample G1423B, and may have been the cause of sudden jumps seen in the magnetoconductance of the QPC sensor in a coupled quantum dot and QPC system in sample G1135B. However, the time scale of the switching and region of conductance in which it was observed may imply that the effect is due to tunneling between edge states of the dot. Finally, A-B oscillations in the quantum dot of sample G1135B were detected by the coupled QPC sensor. To our knowledge this is the first such experiment reported.

5. NONEQUILIBRIUM MEASUREMENTS ON SINGLE QUANTUM DOTS AND A COUPLED QUANTUM DOT AND QUANTUM POINT CONTACT SYSTEM

This chapter discusses measurements concerning nonequilibrium electron transport in quantum dots and QPC systems. Far from equilibrium measurements on single quantum dots were performed in order to investigate hot electron effects. Section one discusses the knee phenomena observed in the I-V characteristics of two quantum dots. While the I-V characteristics of the QPCs can be modeled with an extended Landauer-Büttiker formalism, the I-V characteristics of the quantum dot can not. An energy balance hot electron model does not accurately model the observed data in certain regions of the curves. Ballistic transport, tunneling current, and confinement above the barriers are not included in the model and may account for the discrepancy.

Next, the effect of nonequilibrium current flow through a QPC on the equilibrium conductance peaks of an adjacent quantum dot was investigated. Peak broadening with an increase in QPC current was observed. A straightforward ballistic phonon model was derived to predict electron heating. In addition, phase breaking times were extrapolated from the data which point to possible momentum transfer between the two systems through a Coulomb interaction.

5.1 Far from Equilibrium Transport in Single Dots

In this section the far from equilibrium I-V characteristics of single quantum dots is studied. The characteristics observed are compared to a Landauer-Büttiker formalism and a hot electron energy balance model proposed by Goodnick *et. al.* [85].

5.1.1 Experimental Background

In 1986 Hess and coworkers observed an S-shaped negative differential conductance (SNDC) in the I-V characteristics of a vertical heterojunction diode [82]. When the device switched from a predominantly tunneling mode to a predominantly thermionic emission mode, the I-V characteristics showed a switching behavior. The behavior was believed to be due to injected electrons thermalizing with cold electrons trapped between heterojunction barriers, and a model which employed an energy balance approach was found to agree qualitatively with the observed experimental data.

Wu *et al.* investigated far from equilibrium transport on an AlGaAs/GaAs quantum dot which was fabricated using the split gate technique, similar to the devices used in this research. A schematic of the gate geometry is shown in Fig. 5.1. In this device gates 1 and 2 and gates 2 and 3 form overlapping input and output barriers to the dot while the plunger varies the size. An SNDC similar to that observed by Hess *et al.* was observed in the I-V characteristics of this laterally defined dot. It was theorized that electrons which are thermionically emitted over the entrance barrier inelastically scatter with electrons in the dot, increasing the energy of carriers in the dot and the ability of those carriers to thermionically emit over the exit barrier. Goodnick *et al.* used an energy balance model similar to that employed by Hess and coworkers to explain the SNDC characteristics of Wu's experiment, they and were able to obtain a theoretical fit to the experimental data using physically reasonable model parameters.

Subsequently Berven *et al.* and Smith *et al.* observed switching behavior in single QPCs which was attributed to either unintentional dot formation due to a disordered background potential [86] or a fluctuating barrier potential due to ionized impurity charging [87]. However, no such behavior in single QPCs was observed in this research, therefore the Wu experiment and succeeding hot electron model is

emphasized here.

The dot measured by Wu *et al.* had an overlapping gate structure as shown in Fig. 5.1. This overlap is thought to eliminate a large component of ballistic transport and contribute to carrier-carrier scattering in the dot, thus enhancing the hot electron effect. However, it was unclear whether or not the overlapping gate structure was necessary in order to observe SNDC. In the Wu experiment the gates forming the input and output barriers to the dot were tied together, so the effect of varying the input and output separately was not explored.

In the research presented here the devices were fabricated on MBE material grown by a different laboratory than the material used by Wu *et al.*, and the gate structure was not overlapping (refer to Fig. 3.10). Measurements were performed under source and drain biases similar to the Wu experiment. A current ranging from 0 to 1 μA was sourced and voltage measured in an attempt to observe SNDC. However, all gates were separately varied so that the effect of biasing individual barriers could be observed. The gates were initially biased in the region where CB was observed under near equilibrium conditions, and were varied around these operating points.

5.1.2 Zero Magnetic Field Experiments

Initially, a check was done of the individual input and output barriers with all other gates grounded. The results are shown in Fig. 5.2. The gates are swept from the point of depletion to past pinch off. The curves appear to be the expected I-V characteristics for QPCs. There is a steady turn on of current as the source-drain bias reaches the barrier height and electron transport goes from the tunneling regime to the thermionic emission regime. These I-V curves can be modeled using an extended Landauer-Büttiker formalism as will be shown in section 5.2. The I-V characteristics for the dot are expected to be the same shape as those for the

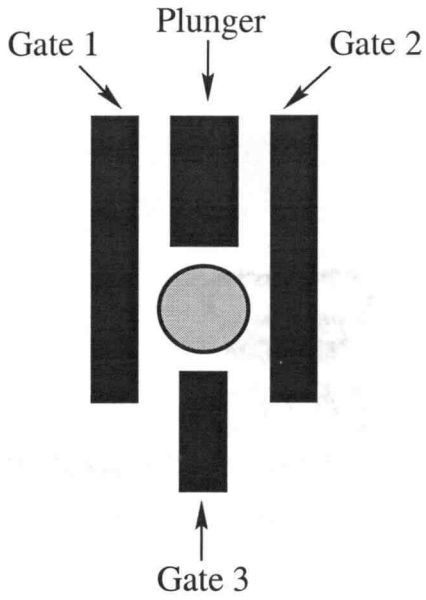

Figure 5.1: Schematic of the device design in the experiments by Wu *et al.*

QPC, and the exact voltage at which turn on occurs should be determined by the dominant barrier height. If the input barrier has a higher gate bias than the output barrier, then the input barrier height will dominate the turn on and vice versa.

The I-V characteristics of the dot structure for sample G1423B are shown in Fig. 5.3. Initially, the input barrier (B1) is just pinched off and the output barrier (B2) is set just above $g = 2e^2/h$, the first conductance step. The plunger bias is then swept from -0.3 V to -0.95 V in -0.05 V steps. While no clear SNDC is observed, a knee, indicated by the circled region, is seen in the I-V curves under certain plunger biases which is not seen in the individual barrier sweeps.[1]

The effect of changing one barrier, while keeping all others fixed, was investigated. In Fig. 5.4 a set of plots is shown for the output barrier fixed at -0.6 V

[1]A less pronounced knee feature is sometimes seen with both input and output barriers biased and the plunger gate grounded. It is possible under these bias conditions that a long narrow dot is formed due to the device design of the e-beam lithography interconnects.

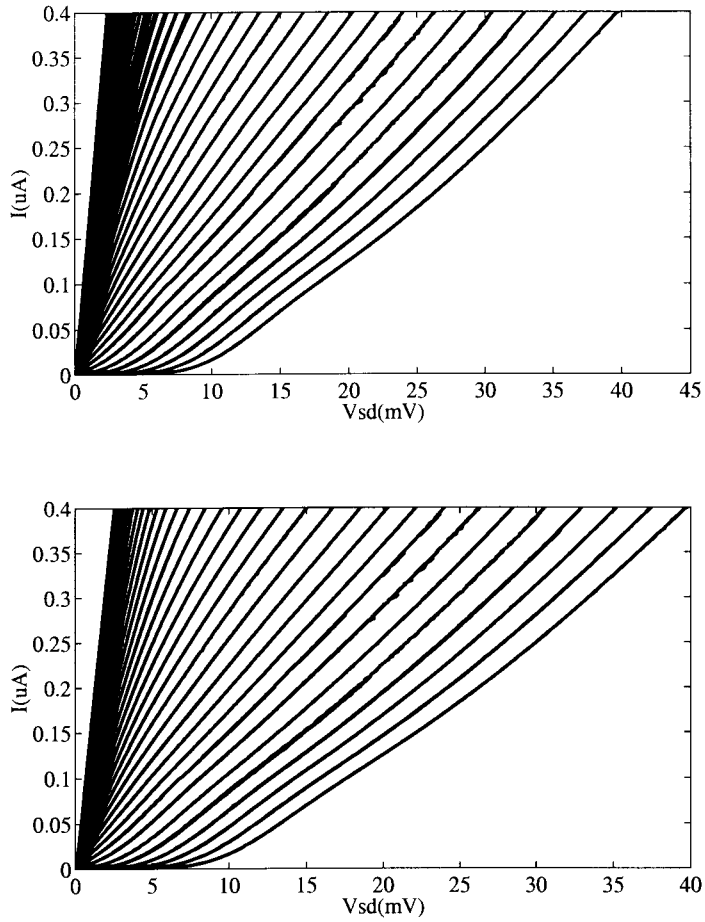

Figure 5.2: I-V characteristics of barrier 1 (top) swept from -0.5 V to -0.95 V, and barrier 2 (bottom) swept from -0.5 V to -0.8 V, dot#1, sample G1423B.

and plunger gate swept . Each successive *frame* corresponds to an *increasing* input barrier (from -0.75 V to -1.0 V in 0.05 V steps, left to right and top to bottom, a-f. A knee does not appear in the I-V curves until a sufficiently high input barrier is reached, B1= -0.85 V. In Fig. 5.5 the input barrier is fixed at -0.9 V, the plunger gate is swept, and each successive *frame* corresponds to a *decreasing* output barrier from -0.8 V to -0.55 V in 0.05 V steps, a-f. The knee does not appear until a sufficiently low output barrier, B2= -0.65 V is reached.

A reverse bias was applied to the dot in order to check the symmetry of the I-V characteristics. The gate biases were fixed so that a knee appears in the I-V

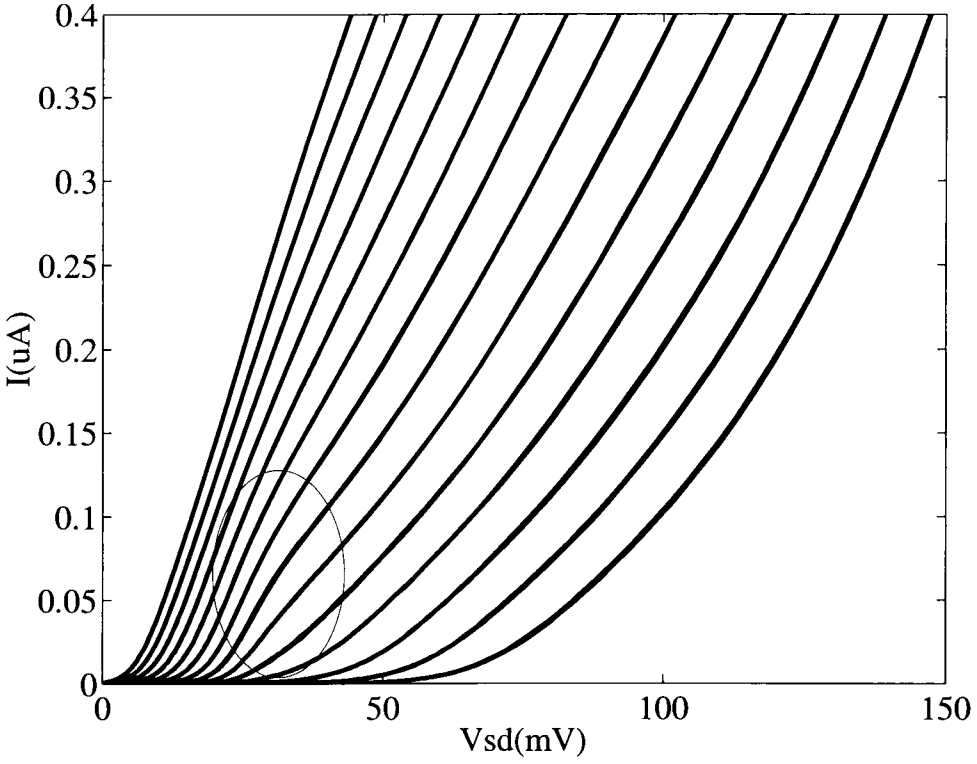

Figure 5.3: The I-V Characteristics of dot#1, sample G1423B with forward source-drain bias, barriers 1 and 2 held constant, and the plunger swept negative.

curves with a forward source-drain bias (Fig. 5.3). Then the source-drain bias is reversed so that electrons are moving in the opposite direction. The I-V curves for a reverse source-drain bias are shown in Fig. 5.6a. Under these bias conditions no knee is observed. If the bias on the *gates* is reversed so that B1 (now the exit barrier) is lower than B2 (now the input barrier), the knee reappears as seen in Fig. 5.6b.

5.1.3 Sample G1135B

One dot on sample G1135B displayed good near equilibrium behavior, and subsequent far from equilibrium measurements were performed on this device. A knee similar to that seen in sample G1423B was observed in the I-V characteristics of the dot. Fig. 5.7 is a plot of the I-V curves for the input barrier pinched off at

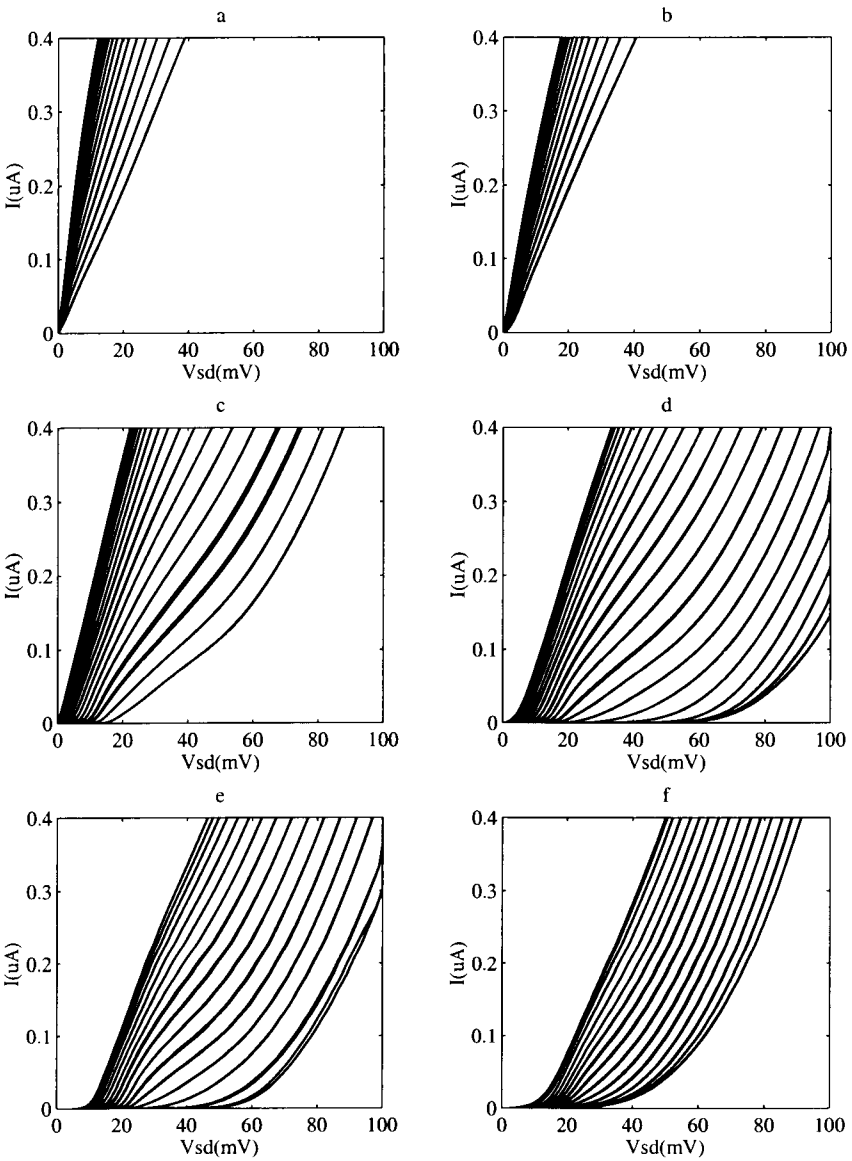

Figure 5.4: The I-V characteristics of dot#1, sample G1423B, with *B1 varied*, B2 kept constant at -0.6 V, and the plunger swept negative. Frame a: B1= -0.75 V b: B1= -0.8 V c: B1= -0.85 V d: B1= -0.9 V e: B1= -0.95 V f: B1= -1.0 V

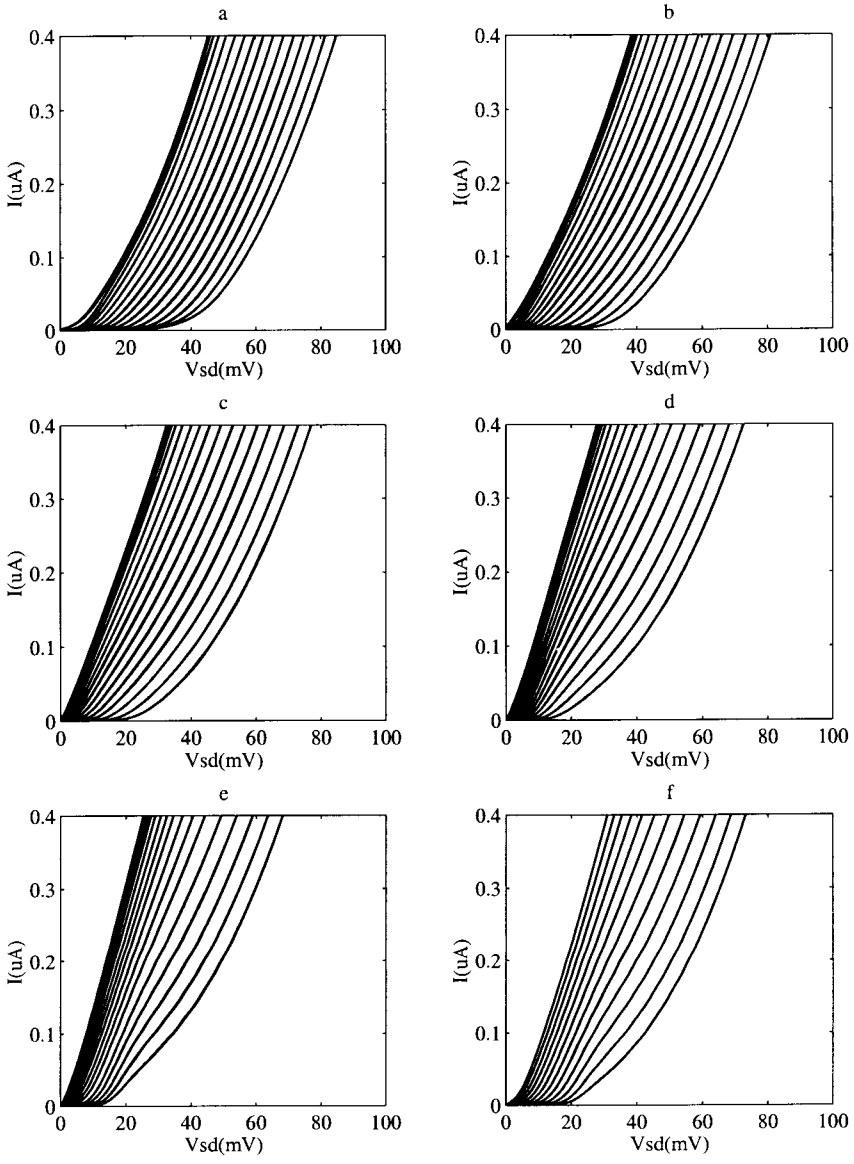

Figure 5.5: The I-V characteristics of dot#1, sample G1423B, with *B2 varied*, B1 kept constant at -0.9 V, and the plunger swept negative. Frame a: B2= -0.8 V b: B2= -0.75 V c: B2= -0.7 V d: B2= -0.65 V e: B2= -0.6 V f: B2= -0.55 V

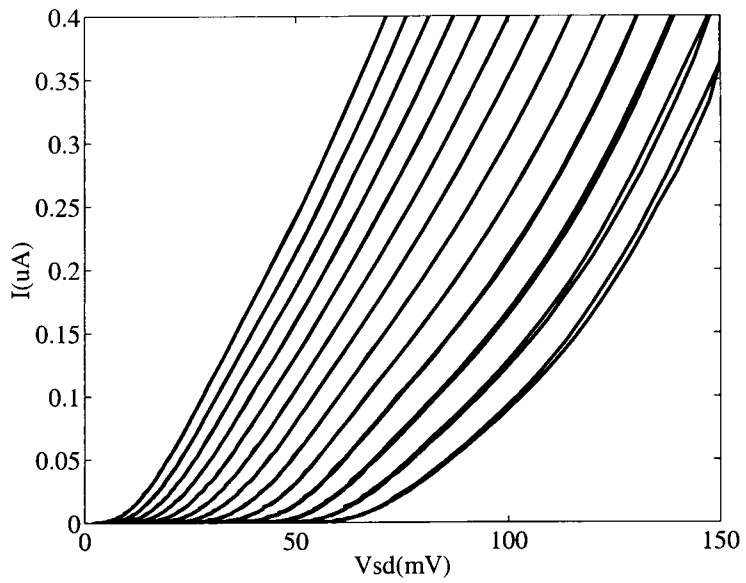

a

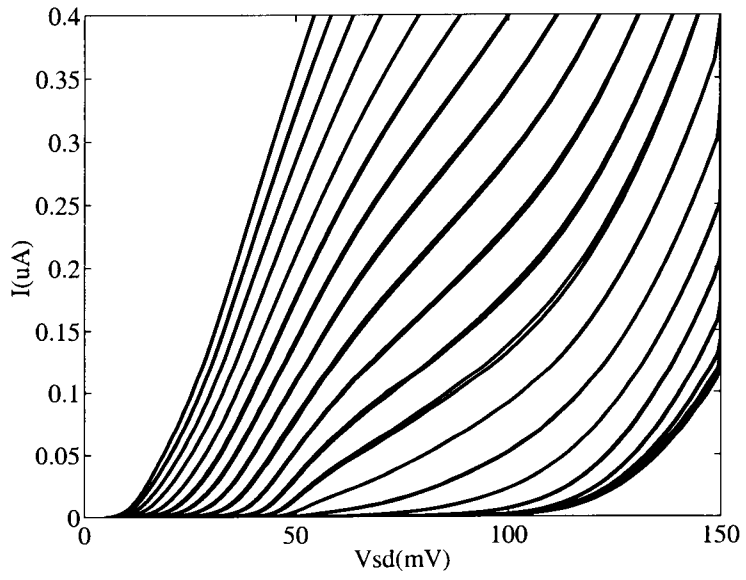

b

Figure 5.6: The I-V characteristics of dot#1, sample G1423B, with a reverse source-drain bias, and (a) gate voltages as in Fig. 5.3 and (b) gate voltages reversed compared to Fig. 5.3.

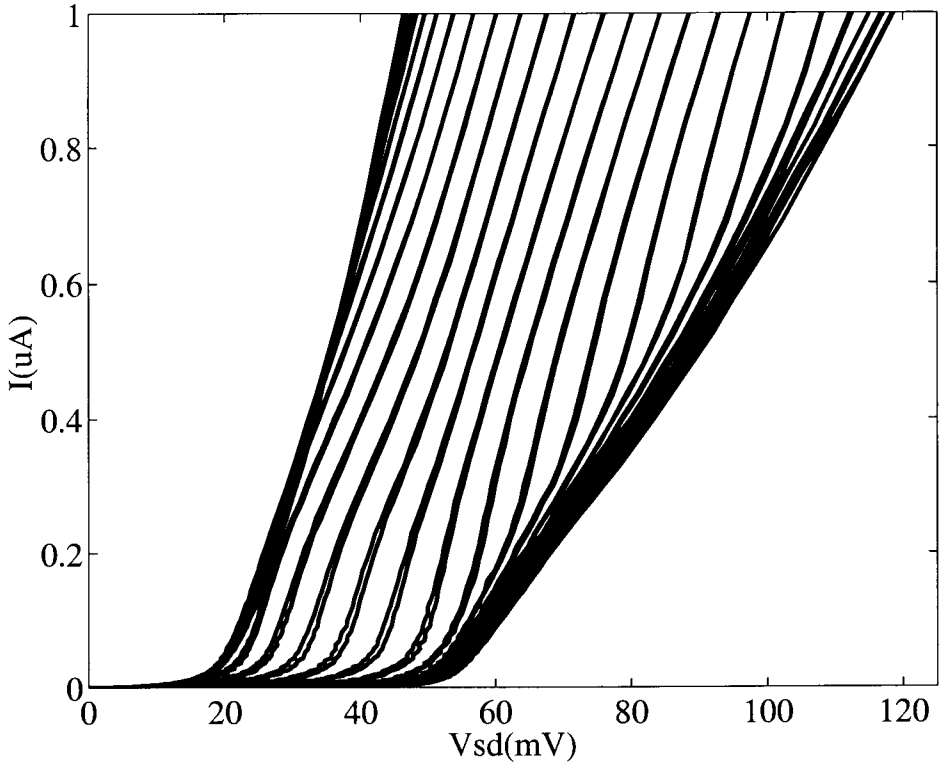

Figure 5.7: The I-V characteristics of dot#1, sample *G1135B*, with a forward source-drain bias.

-0.6 V, the output barrier at approximately one conductance step, -0.4 V, and the plunger swept from -0.5 V to -0.75 V in 0.01 V steps. The knee was observed under similar gate and source drain bias as in sample G1423B. The input barrier had to be higher than the output barrier, and when the source-drain was reversed with the same gate biases, the knee disappeared.

5.1.4 Discussion in Terms of the Hot Electron Picture

Recall from the background discussion at the beginning of the chapter that in the hot electron picture, electrons entering the dot thermalize with the cold electrons in the dot and enhance the thermionic emission out of the dot. The behavior of the knee with changing entrance barrier height can be interpreted in terms of this hot electron picture. The electrons which enter the dot do not have enough energy to

heat the cold electrons in the dot and enable them to thermionically emit over the exit barrier, *until a critical input barrier height is reached.*

A similar interpretation can be given for the behavior of the knee with changing exit barrier. For a given input barrier height, if the output barrier is too high, electrons in the dot will not have enough energy to thermionically emit over the output barrier. Then the input barrier must be raised to see the knee reappear. Fig. 5.8 illustrates this secondary point. In Fig. 5.8a the input barrier was just pinched off at -0.95 V and the output barrier was biased at -0.7 V. A change in slope which is not quite a knee was observed. Then in Fig. 5.8b the output barrier was kept at -0.7 V, the input barrier was increased to -1.0 V, and the knee became slightly more pronounced.

As the input and output barriers were shifted around, the plunger gate bias at which the knee was seen also shifted. This is to be expected since the dot area is so small. At these dimensions the plunger bias not only changes the size of the dot, but also affects the conductance of the input and output barriers to some degree. Thus, for a higher bias on the input and output gate barriers, a lower plunger bias would be required to observe a knee, as seen for example in the successive frames of Fig. 5.5. A knee first appears in frame d when the plunger gate is at -0.6 V (fourth curve in from the right). Then the output barrier is reduced, and in frame f the knee is not observed until the curve corresponding to a plunger gate bias of -0.75 V (third curve in from the right).

The features of the I-V curves seen under reverse source-drain bias can also be explained by the hot electron picture as described above. A set of energy band pictures corresponding to the forward and reverse bias schemes helps to illustrate the physical situation and is given in Fig. 5.9. A knee appeared in the I-V curves when the gates were fixed so that the input barrier to electrons was higher than the output barrier (Fig. 5.9a). When the polarity of the source-drain bias was reversed,

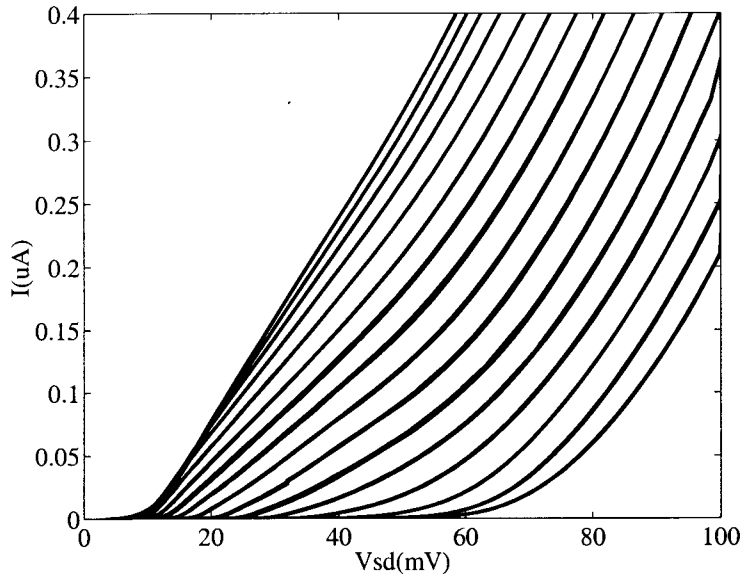

a

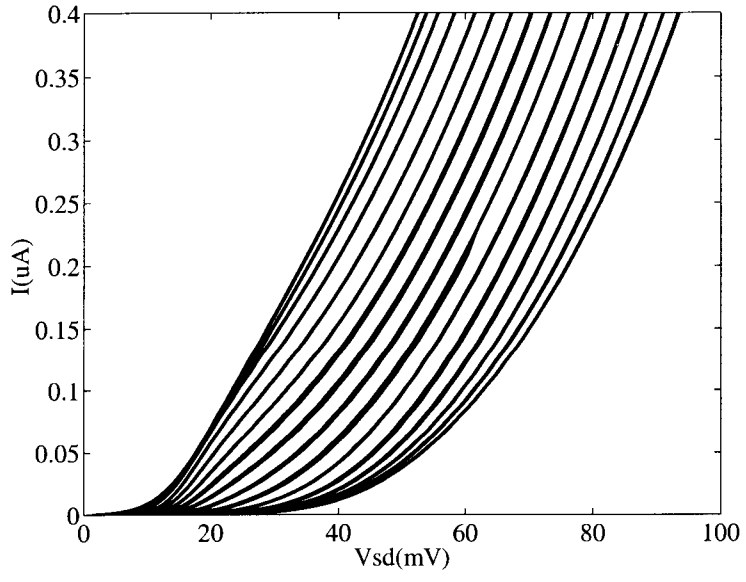

b

Figure 5.8: The I-V characteristics of dot#1, sample G1423B with (a) B1= -0.95 V, B2= -0.7 V and (b) B1= -1.0 V, B2= -0.7 V.

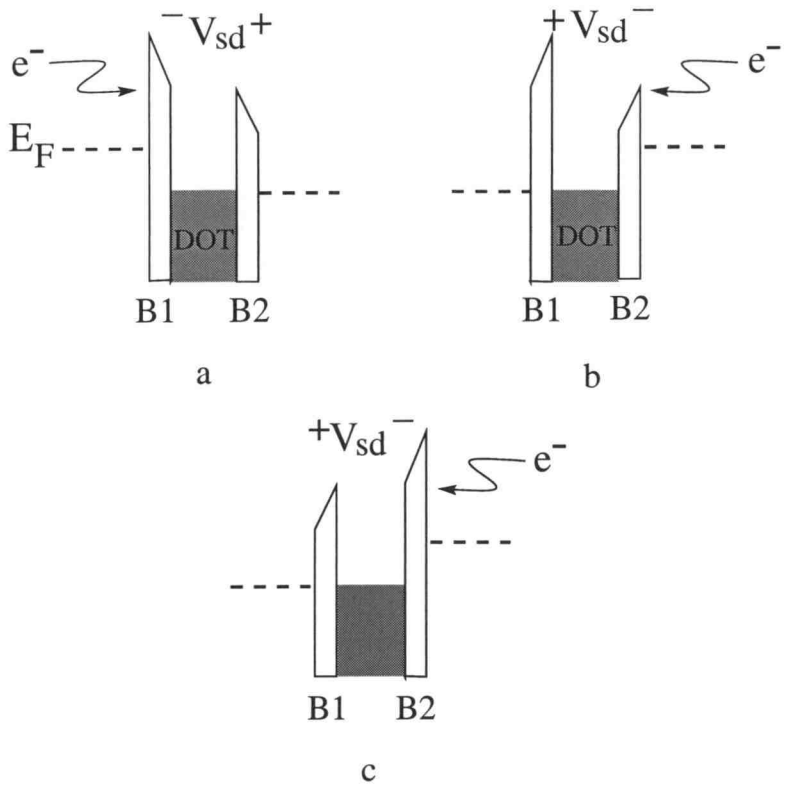

Figure 5.9: Energy band schematics of (a) forward source-drain bias, B1 higher than B2, (b) reverse source-drain bias, B1 higher than B2, (c) reverse source-drain bias, B1 *lower* than B2.

and electrons flowed in the opposite direction under the same gate bias voltages, the input barrier was no longer higher than the output barrier (Fig. 5.9b). Then, electrons coming in to the dot did not have enough energy to transfer to the cold electrons in the dot and cause them to thermionically emit over the output barrier. And coincidentally no knee was observed. When the barrier heights were reversed, the physical situation was symmetric to the initial forward bias case (Fig. 5.9c), and the knee reappeared.

5.1.5 Application of a Magnetic Field

The fact that SNDC due to hot electron bistability was not seen may arise from the lack of sufficient carrier-carrier scattering in the dot. Two dot characteristics

may reduce the carrier-carrier scattering: the small size and low number of electrons in the dot and the geometry of the device which probably induces a large component of ballistic transport. With the given size and geometry of the dot, application of a magnetic (**B**) field perpendicular to the direction of transport may increase the carrier-carrier scattering in the dot. In a semiclassical picture the **B** field would produce a Lorentz force on the electrons traversing through the dot causing them to follow a curved path (cyclotron radius, $r_c = \hbar k_F / 2m^*$) and increasing the chance of carrier-carrier scattering as the cyclotron radius approaches the size of the dot. In the quantum mechanical picture, discrete edge states are formed in the dot which increase the traversal time through the dot and thus increase the probability of scattering.

In Fig. 5.10a a plot is shown of the I-V characteristics for the input barrier just pinched off, -1.0 V, the output barrier set at one conductance step, -0.65 V, and the plunger gate fixed at -0.3 V, similar to the biases in Fig. 5.3. Each curve is for a different **B** field from 0 to 2.6 T. As the field was increased, the knee became sharper. The magnitude of the knee was determined by essentially subtracting a curve fit without the knee that had the same turn on and final slope, from the curve with the knee. An algorithm was used to find the perpendicular line from one curve to another at each data point and calculate the distance (a combination of current and voltage). The maximum distance calculated was considered to be the magnitude of the knee.

Figure 5.10b shows the magnitude of the knee, in terms of the change in V_{sd} from a curve without the knee, as a function of **B** field. The magnitude of the knee clearly increases with increasing **B**. There are two distinct regions of the magnitude of the knee, one below 0.8 T and one above 0.8 T. A line is drawn through the average in the two distinct regions. For an electron with a energy of 40 meV, the cyclotron radius reaches 200 nm at approximately 0.8 T. At this **B** field the electrons

coming into the dot with $\sim 40\ meV$ would encounter increased scattering due to their cyclotron radius approaching the radius of the dot. Thus the enhanced knee may be due to an increase in scattering in the dot. However, it is expected that at higher and higher **B** field, the energy landscape will be altered significantly enough to eliminate this effect. Landau levels in the 2DEG reservoir will be depopulated creating a higher magnetoresistance and edge states will also be depopulated leaving fewer electrons in the dot.

5.1.6 Magnetic Field Applied to Sample G1135B

In contrast to the I-V curves of sample G1423B, when a **B** field is applied, the magnetoresistance dominates the transport and washes out all other features as shown in Fig. 5.11. Since the dot in this device is smaller than the dot of sample G1423B as determined from capacitance measurements, the **B** field at which the cyclotron radius approaches the size of the dot is higher and at these higher fields the dot may be depopulated enough so that the carrier-carrier scattering would not be significant.

5.1.7 Temperature Dependence

With all the gate biases kept constant the I-V curves of sample G1135B were measured as a function of temperature. Fig. 5.12 displays the data for each temperature. At approximately 4.2 K the knee disappears. Experimentally, Wu *et al.* observed the disappearance of the SNDC at higher temperatures for higher gate biases. This same dependence is seen for the knee behavior observed in this research. For instance in frame e of Fig. 5.12 the knee is washed out in the I-V curves with the lower plunger gate bias (left most curves), but remains in the I-V curves with the higher plunger gate bias (right most curves).

In the hot electron picture, current is dominated by thermionic emission (see Section 5.3). Since the process of thermionic emission increases exponentially with

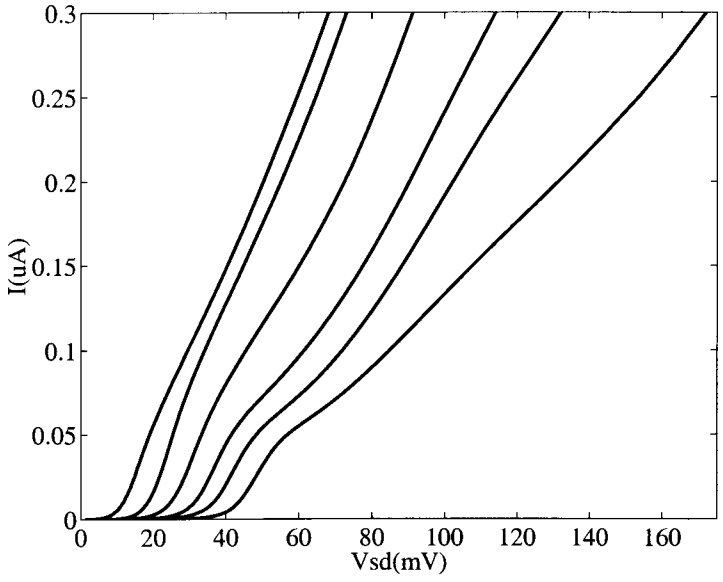

a

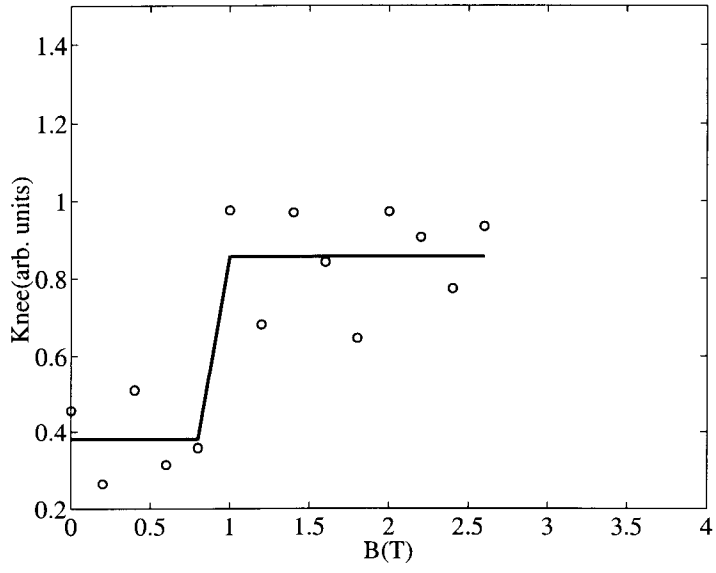

b

Figure 5.10: (a) I-V characteristics of dot#1, sample G1423B. B1, B2, and the plunger gate are held constant and each successive plot corresponds to an increasing **B** field 0, 0.6, 1.0, 1.6, 2.0, and 2.6 T (plots offset for clarity). (b) The magnitude of the knee as a function of **B** field, dot#1, sample G1423B.

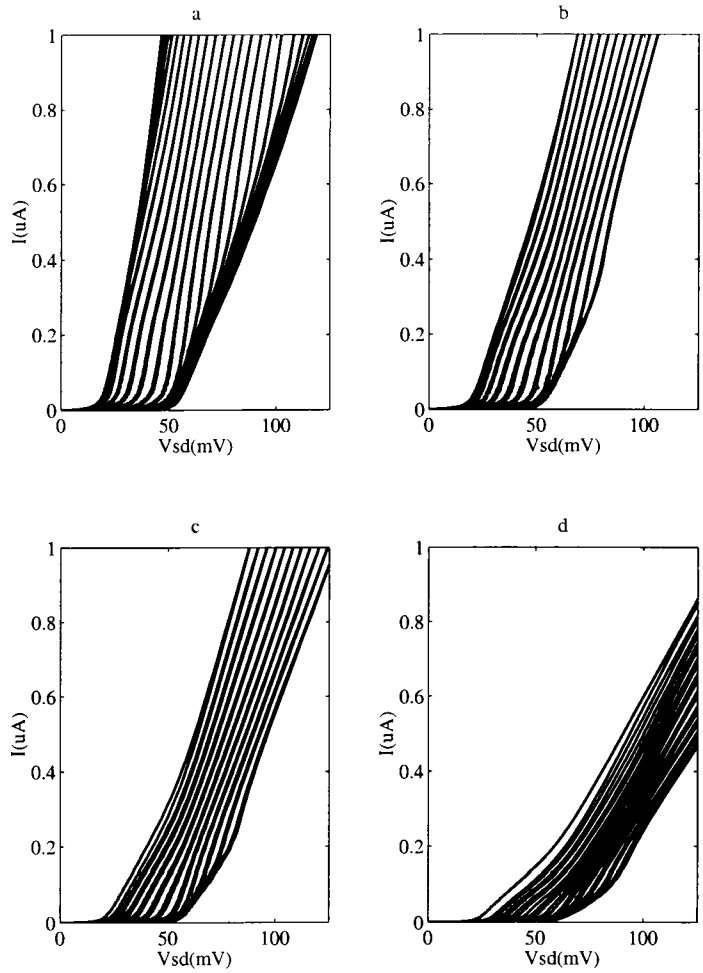

Figure 5.11: I-V characteristics of dot#1, sample G1135B, as the **B** field is increased, (a)**B**=0 T, (b)**B**=.6 T, (c)**B**=1.0 T, (d) **B**=1.6 T.

temperature, at a certain temperature, the electrons in the dot may be able to emit over the exit barrier without additional energy from carrier-carrier scattering. At higher temperatures, higher gate biases are needed to meet the conditions of input barrier height (and therefore energy of entering electrons) and output barrier height (and therefore electron energy necessary to exit the dot) relative to the electron energy in the reservoir which will produce the critical current necessary for switching.

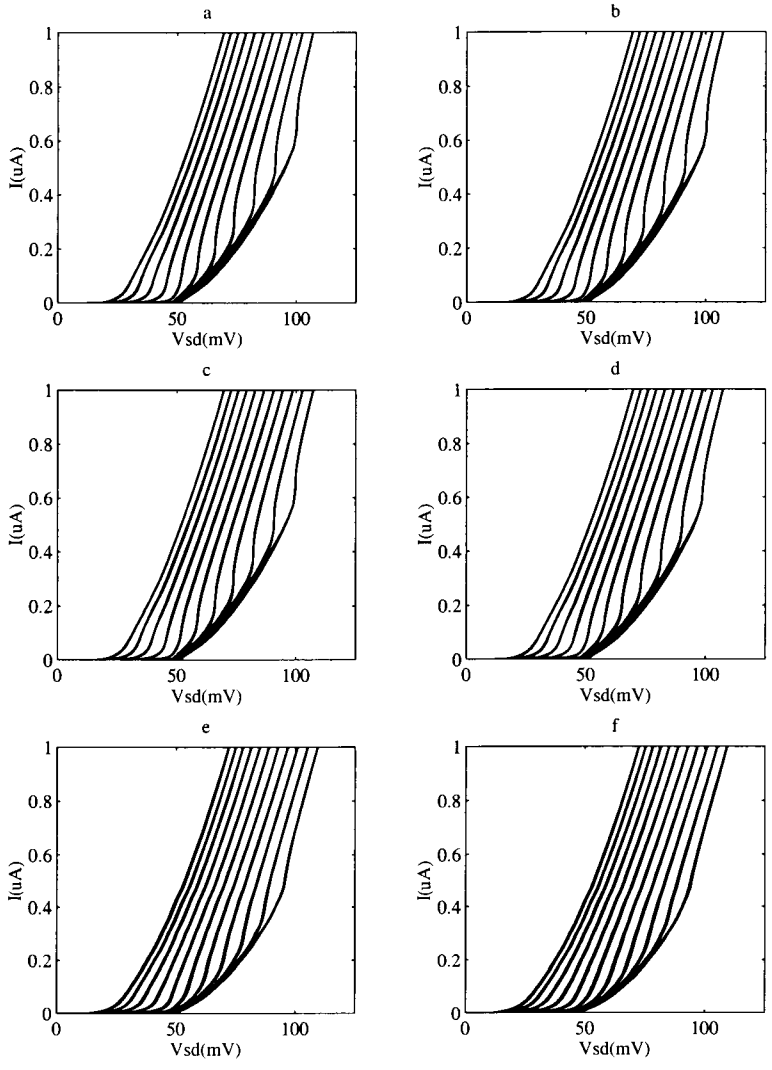

Figure 5.12: I-V characteristics of dot#1, sample G1135B plunger swept, (a)=300 mK, (b)=500 mK, (c)=1.2 K, (d)=2.0 K, (e)=4.2 K, (f)=5.0 K

5.2 Extended Landauer-Büttiker Formalism for a Single QPC

The Landauer-Büttiker (L-B) formalism can be extended to describe a QPC when all conductance plateaus have been pinched off [6]. The model will be described below and then compared to the experimental data of a single QPC on sample G1423B.

5.2.1 Model Description

As described in Chapter 4, in the Landauer-Büttiker formalism under finite temperatures the expression for the total current from left to right is the current injected from the left minus the current injected from the right.

$$I = \frac{2e}{h} \int_{-\infty}^{\infty} dE \sum nT_n(E) \left[f(E - \mu_l) dE - f(E - \mu_r) dE \right] \tag{5.1}$$

For cryogenic temperatures we can assume that T=0 K. Then the Fermi-Dirac distributions become step functions and the expression for the current can be simplified to

$$I = \frac{2e}{h} \sum n \int_{0}^{\mu_l} dE T_n(E) - \int_{-eV_{sd}}^{\mu_r} dE T_n(E) \tag{5.2}$$

As mentioned in Chapter 4, the transmission coefficient is a function of the potential profile in the quantum point contact. For a saddle point potential it is

$$T_{mn}(E) = \delta_{mn} \frac{1}{1 + exp^{-\beta\left(\frac{h}{2\pi}\omega_y(n+\frac{1}{2}) - e\phi\right)}} \tag{5.3}$$

$$\beta = \frac{2}{\hbar\omega_x} \tag{5.4}$$

where ϕ is the barrier height of the saddle point potential. Under nonequilibrium biases ϕ takes the form

$$\phi = \phi_o - \frac{V_{sd}}{\alpha} \tag{5.5}$$

where ϕ_o is the potential barrier under near equilibrium conditions and $1/\alpha$ is the fraction of V_{sd} that is dropped across the barrier.

5.2.2 Comparison With Experimental Data

Figure 5.13 shows a comparison of the L-B theory with experimental data of a single QPC from sample G1423B, with $\hbar\omega_y = 4\ meV$, $\phi_o = 6.5\ meV$ (in close agreement with the calculated values from the 3D Poisson- 1D Schrödinger solver, $\alpha = 5$, and $\hbar\omega_x = .85\ meV$. The turn on can be very accurately modeled. The final slope after turn on is slightly different in theory than in the experimental data. In the extended L-B theory the parameter α is the fraction of V_{sd} that is dropped across the barrier and is treated as a constant. In reality α is a function of the source-drain bias. As V_{sd} increases a smaller fraction may be dropped across the barrier, decreasing the current. Thus for the same V_{sd} the actual current is slightly less than the current expected from the theory.

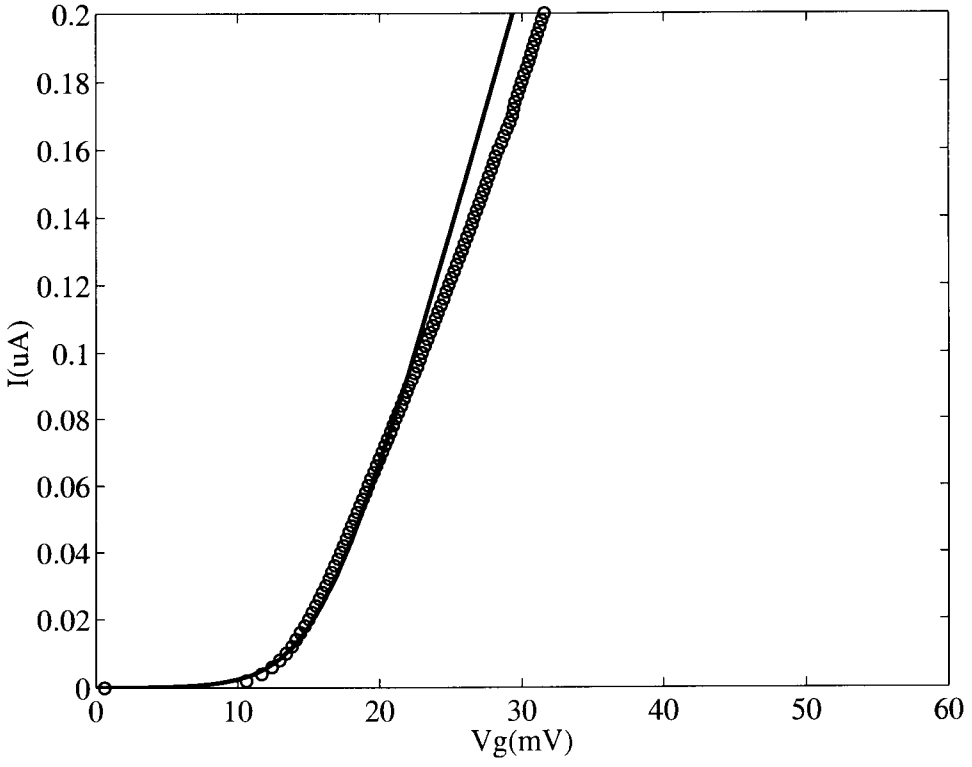

Figure 5.13: Comparison of the I-V characteristics for B1=-.95 V from experiment (circles) and L-B theory (solid line).

5.3 An Energy Balance Hot Electron Model

The extended L-B theory can not be used to fit the knee feature in the I-V curves of the quantum dots. Regardless of which parameters are varied, the model will never produce a knee feature in the I-V characteristics. Instead, an energy balance hot electron model which can produce SNDC features is compared with the experimental data. The model is described below.

5.3.1 Model Description

The potential profile for the dot along the direction of transport is shown in Fig. 5.14. The Fermi energies are given by

$$\frac{1}{e}(E_{F1} - E_{F2}) = \frac{V_{sd}}{2} + \frac{Q}{C} \tag{5.6}$$

$$\frac{1}{e}(E_{F2} - E_{F3}) = \frac{V_{sd}}{2} - \frac{Q}{C}. \tag{5.7}$$

$Q = e(N_o - N)$ is the excess charge on the dot where N_o is the equilibrium number

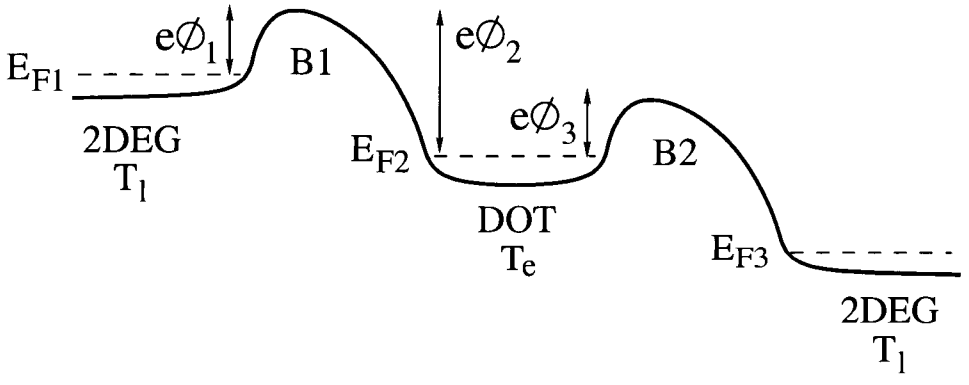

Figure 5.14: Potential profile of the dot with input and output barriers connecting to 2DEG reservoirs.

of electrons on the dot. C is the dot capacitance. The input, ϕ_1, and output, ϕ_2, barriers under an applied source-drain bias are given by,

$$\phi_1 = \phi_o - \left(\frac{V_{sd}}{2} + \frac{Q}{C}\right)/\alpha \tag{5.8}$$

$$\phi_2 = \phi_o - \left(\frac{V_{sd}}{2} - \frac{Q}{C}\right)/\alpha. \tag{5.9}$$

As in the extended L-B theory, ϕ_o is the equilibrium barrier height and α is a parameter indicating how V_{sd} is dropped across the input barrier. The excess potential that the electrons have upon entering the dot is given by

$$\phi_1' = \phi_o + \left(\frac{V_{sd}}{2} + \frac{Q}{C}\right)\left(1 - \frac{1}{\alpha}\right). \tag{5.10}$$

In the model several physical assumptions are made. The dot is assumed to be large so that it can be treated as a finite extent 2DEG. Ballistic transport is considered to by minimal, and tunneling through the barriers is ignored. Current into and out of the dot is limited by thermionic emission. Therefore, the current flowing through the entrance barrier is

$$I = eWv_l kT_l D_o \left(e^{n_s/D_o kT_l} - 1\right) e^{-e\phi_1/kT_l}, \tag{5.11}$$

and through the exit barrier is

$$I = eWv_e kT_e D_o \left(e^{N/AD_o kT_e} - 1\right) e^{-e\phi_2/kT_e}. \tag{5.12}$$

W is the width of the constriction, T_l and T_e are the lattice and electron temperatures (a heated Maxwell-Boltzmann distributions is used for the electron temperature) respectively, $v_l = \sqrt{kT_l/2\pi m^*}$ is the mean velocity of electrons in the 2DEG, $v_e = \sqrt{kT_e/2\pi m^*}$ is the mean velocity of electrons in the dot, $D_o = m^*/\pi\hbar^2$ is the 2D density of states, and n_s is the 2D electron density.

Finally, the energy balance in the dot is represented as

$$I\left(\phi_1' + \frac{kT_l}{e} - \phi_2 - \frac{kT_e}{e}\right) = N\langle\frac{\partial E}{\partial t}\rangle_{coll}. \tag{5.13}$$

The energy loss rate is due to collisions with both acoustic and optical phonons,

$$\langle\frac{\partial E}{\partial t}\rangle_{coll} \approx \frac{\hbar\omega_o}{\tau}_{pop} e^{-\frac{h}{2\pi}\omega_o/kT_e} + \frac{k(T_e - T_l)}{\tau}_{ac}, \tag{5.14}$$

where ω_o is the longitudinal-optical phonon energy, τ_{pop} is the polar-optical emission time, and τ_{ac} is the acoustic-phonon energy relaxation time, all of which can be obtained from the literature. An initial current and lattice temperature is assumed, and then all three current equations as well as the equations for ϕ_1, ϕ_2, and ϕ_1' are solved simultaneously for V_{sd}, Q, and T_e.

5.3.2 Comparison with Experimental Data

Figure 5.15 shows the experimental data for sample G1135B plotted next to the I-V characteristics from the hot electron model of Goodnick *et. al.*. The parameters used are given in Table 5.1 The approximate turn on and final slope of the I-V curve can be fit fairly accurately, but the current at which the knee is observed is not reproduced well by the hot electron model. This may be due to several factors. Two important assumptions in the model most likely do not apply to the devices studied in this research, the neglect of ballistic transport and tunneling current. Tunneling current is the first current observed as the device turns on between $V_{sd} = 20 - 30\,meV$. In the devices studied here, there is probably a significant component of current due to electrons which emit over the entrance barrier and reach the exit barrier without any collisions. Tunneling current could also contribute to an increase in current for a given V_{sd}. Increases in ballistic and tunneling current could obscure the SNDC and only a remnant would be observed.

Another physical assumption of the model is that there is no confinement above the energy barrier, ϕ_o. However in systems with such small dimensions it is likely that the parabolic potential above the barrier height will be narrow enough to create quantization of energy levels which may play a significant role in the transport. Inclusion of confinement above the barriers may shift the region in which the knee is observed. In addition, the number of electrons in the dot is assumed large enough so that a heated Maxwell-Boltzmann distribution can be used. In reality

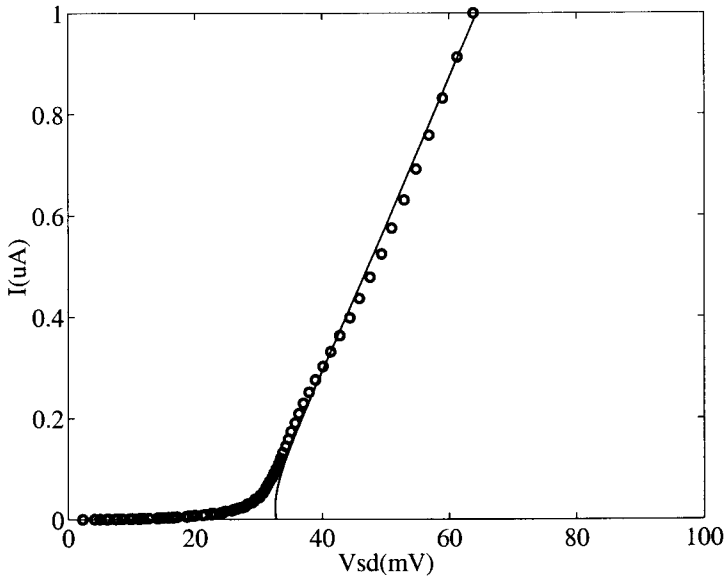

Figure 5.15: Comparison of the I-V characteristics of the dot from experiment (circles) and hot electron theory (solid line).

Table 5.1: Parameters used in the hot electron model.

Parameter	Value
α	0.5
ϕ_o	$38\ meV$
W	$150\ nm$
C_{dot}	$143\ aF$
N	150
τ_{ac}	$80\ pS$
τ_{pop}	$1.5\ pS$
T_l	$.1\ K$
n_s	$1.5 \times 10^{11}\ cm^{-2}$

the number of electrons in the dot is on the order of 100. This number is probably too small to use a classical or even a statistical Fermi-Dirac distribution and large enough to make a quantum mechanical many body calculation very difficult. Clearly, modifications to this model must be made in order to more accurately compare the I-V characteristics of these devices with a hot electron model.

5.3.3 Larger Dots

It has been hypothesized that a critical number of electrons is needed to observe SNDC [140]. The hot electron model predicts the opposite. When all other parameters are held constant and the number of electrons is reduced, the SNDC is more apparent (see Fig. 5.16).

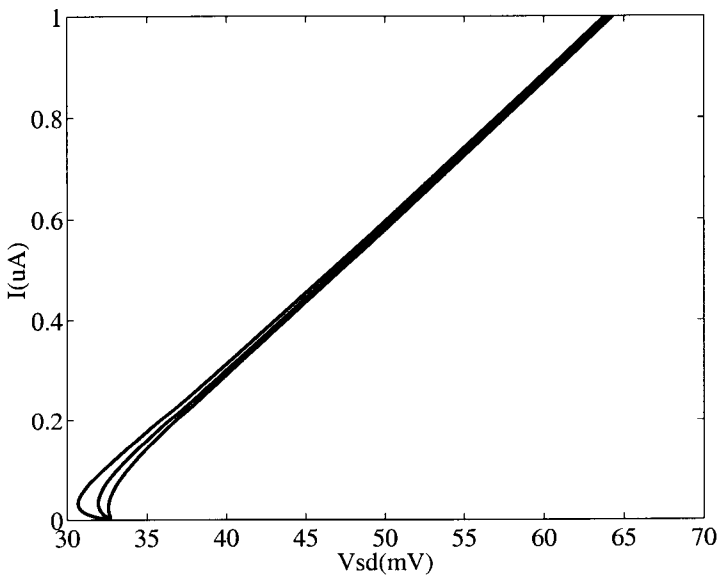

Figure 5.16: Comparison of the I-V characteristics of the dot from hot electron theory. The left curve is for 10 electrons in the dot, middle for 50, and the right curve for 100 electrons. All other parameters are the same.

A comparison to larger dots with a larger number of electrons would give insight into this discrepancy. In addition, a different geometry of input and output

barriers may increase carrier- carrier scattering (as in the device fabricated by Wu *et. al.*). Due to the limited number of samples available, these two aspects were combined by fabricating larger dots with offset input and output barriers as shown in Fig. 5.17. However, these devices did not exhibit good near equilibrium behavior. An apparent parallel conduction was observed in these samples, and no other measurements were attempted.

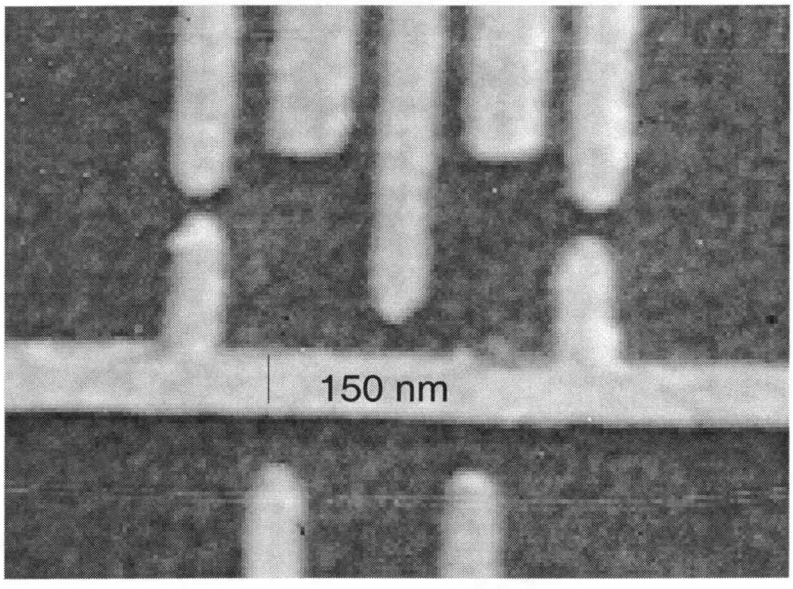

Figure 5.17: SEM micrograph of a larger double dot structure with offset input and output barriers, fabricated on MBE material.

5.4 Dot Heating Due to Nonlinear Transport in an Adjacent QPC

In this section the effect of nonequilibrium current through a QPC on the near equilibrium transport of a quantum dot is investigated. The motivation was to attempt the first observation of Coulomb drag (kinetic energy transfer via intercarrier scattering) between a 1D and 0D system.

5.4.1 Background

The influence of one electronic system on another under nonequilibrium conditions has been of interest for a number of years. Experimental evidence of Coulomb drag was first presented by Solomon *et al.* [141] for a two-dimensional electron gas (2DEG) coupled to a three-dimensional electron gas and by Gramila *et al.* [142] for two coupled 2DEGs. In the experiments by Gramila *et al.*, current flow in one 2DEG induced a voltage of opposite sign in the neighboring 2DEG approximately 20 *nm* away. This drag voltage was attributed to a momentum transfer between the 2DEG systems. A schematic of the experiment is shown in Fig. 5.18.

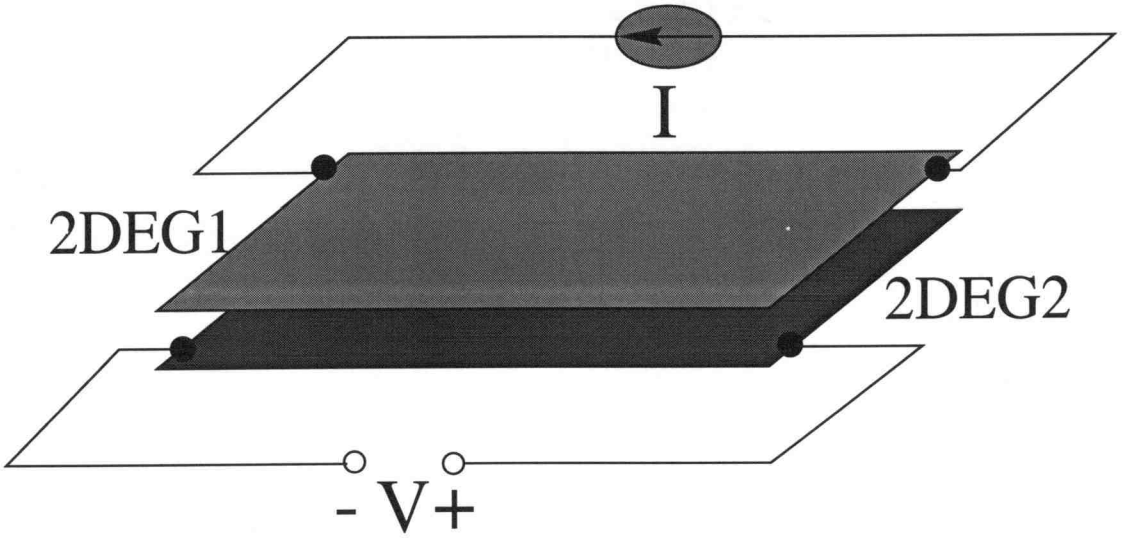

Figure 5.18: Conceptual picture of the 2D Coulomb drag experiment by Gramila *et. al.*

In the measurements presented here we investigate the influence of current flow through a 1D channel on the near equilibrium transport characteristics of an adjacent quantum dot. The same dot and QPC coupled system, sample G1135B, was used as in the near equilibrium measurements presented in Chapter 4. Recall the gate pattern used as shown in the micrograph in the inset of Fig. 5.19. The 1D

channel is approximately 200 nm from a quantum dot with lithographic dimensions of 400 nm x 350 nm and an actual diameter of approximately 200 nm.

5.4.2 Experiment

All measurements were performed in a dilution refrigerator system at a base temperature of 10 mK. In the QPC, 1D behavior was observed over a range of four conductance steps. The 1D channel was biased in the middle of this range so that 1D behavior was assured even if the source-drain bias changed the gate bias to some degree. Therefore, two modes were conducting in the constriction, and a DC current was applied through the constriction in order to study the influence of transport in the 1D system on the conductance of the quantum dot. The quantum dot was biased in the Coulomb blockade (CB) regime, where the peak structure for dot#1 on sample G1135B was shown in Chapter 4, Fig. 4.5b, and is displayed again in Fig. 5.19a with varying 1D channel current and background current subtracted. As the DC current in the 1D channel was increased from 0 nA to 100 nA, changes in the height and position of the conductance peaks of the quantum dot were observed which are shown by the successive curves in Fig. 5.19a. Some peak maxima decrease while others increase and the peak to valley ratios systematically decrease with increasing 1D channel current as shown in Fig. 5.19b. The peak to valley ratios were determined by taking the derivative of the curves, finding the successive zeroes from a peak to it's valley on the right (higher gate voltage), and taking the ratio of the conductance at these zeroes. When the current is turned off the peaks are restored to their original heights and positions.

5.4.3 Discussion of Results

The broadening of the conductance peaks is suggestive of a heating effect in the electrons in the quantum dot system due to current flow in the 1D channel. The changes are reminiscent of the temperature effects observed in the CB peaks

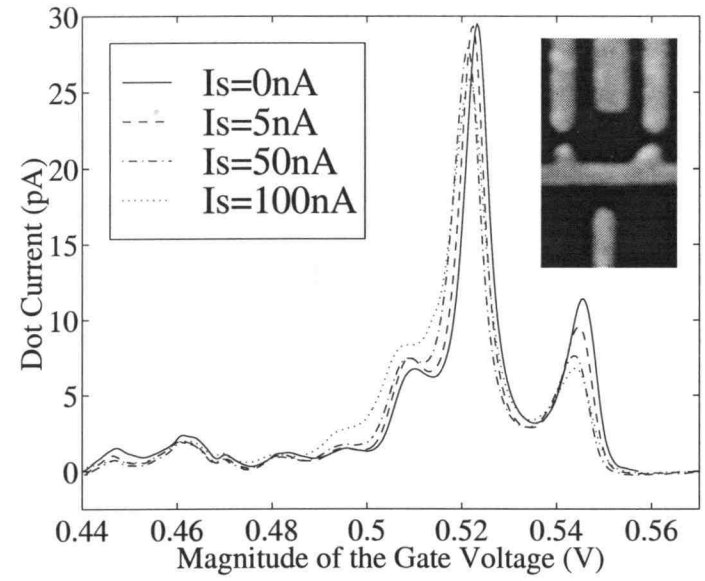

a

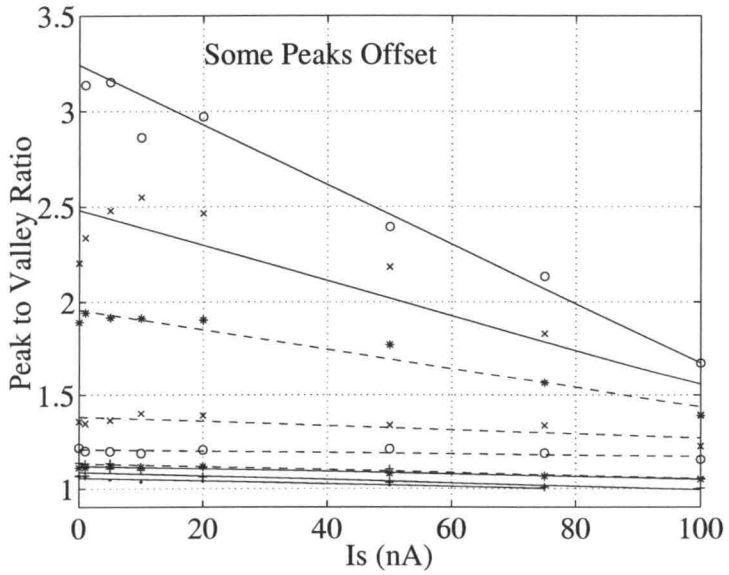

b

Figure 5.19: (a) Conductance peaks of the quantum dot for various 1D channel currents (Is). Inset: Micrograph of the quantum dot and adjacent QPC. (b)Peak to valley ratio vs 1D channel current for different peaks.

of a quantum dot by Scott-Thomas *et al.* [46] and Meirav *et al.* [47] and explained theoretically by Meir *et al.* [129]. In the data shown in Fig. 5.19, the peak positions with respect to gate voltage shift in a complicated way as the 1D channel current is increased. The peaks themselves are not regular in terms of their peak heights which is suggestive of a strong interaction of the level structure and Coulomb charging in these structures close to pinch-off, as discussed in Chapter 4.

Possible explanations of the peak broadening of the conductance peaks with 1D channel current include heating through electron-electron interactions, and heating through electron-phonon interactions due to the energy dissipation in the contact regions. The transfer of momentum due to electron-electron scattering between the 1D channel and the quantum dot is analogous to the Coulomb drag effect observed between two quantum wells. Here the separation between the 1D channel and the dot (approximately 200 nm) is larger than typical dimensions used in 2D-2D drag experiments where the spacing is several hundred angstroms. This reduction in the drag effect due to distance is expected to be compensated by the much more sensitive nature of charge transport in the Coulomb blockade regime where tunneling is the transport mechanism.

Another type of broadening could occur if the transport through the dot is dominated by resonant tunneling due to the dot level structure or impurities, rather than simple Coulomb blockade. The broadening could then be associated with a reduction of the phase breaking time, τ_ϕ, due to inelastic scattering between the dot electrons and the 1D channel. Such an interaction could increase the amount of off resonant current leading to a decrease in peak to valley ratio in the conductance peaks.

Finally, heating of the dot electrons could arise due to phonon emission as carriers relax in the contact regions adjacent to the point contact under an applied bias. Based on the bulk thermal conductivity of GaAs at low temperature, the

expected rise in temperature in the dot due to the power dissipation from the 1D channel is estimated to be quite small, on the order of 1 μK. However, it is well known that the ballistic mean free path of phonons at such temperatures in undoped material is on the order of the sample size itself. Hence, diffusive heat transport is invalid, and electrons in the dot may couple directly to the acoustic phonons emitted as injected carriers from the 1D channel relax in the neutral regions close to the quantum point contact. These phonons can transport ballistically to the region under the dot, couple with the electrons in the dot, and cause a general heating which is observed as peak broadening. Indirect phonon coupling has also been predicted in explanations of Coulomb drag in coupled 2D quantum well systems. Detailed calculations of both the Coulomb interaction between the electrons in the 1D channel and in the quantum dot and the electron-phonon coupling are necessary to elucidate the proper explanation of the observed behavior.

5.4.4 Theoretical Modeling

An estimate can be made of lattice heating under the dot due to ballistic phonons. It is assumed that all the power is dissipated in the 2DEG reservoir (near the barriers) to the lattice via emission of acoustics phonons and that the phonons radiate outward without scattering.

The average distance radially between emitted phonons is given by

$$\Delta r = \tau_q v_o \tag{5.15}$$

where v_o is the phonon velocity, and $\Gamma_q = 1/\tau_q$ is the emission rate of phonons of wave vector q. The number of phonons of with wave vector q per unit radial distance is therefore

$$N = \frac{1}{v_o}\Gamma_q. \tag{5.16}$$

If one considers a ring in the plane parallel to the interface between r and $r + dr$,

the area of this ring is

$$\pi (r + dr)^2 - \pi r^2 = 2\pi r dr \tag{5.17}$$

Therefore, the number of phonons per unit area with a certain wave vector at some radial distance r from the source is given by

$$n_q(r) = \frac{1}{2\pi v_o r}\Gamma_q \tag{5.18}$$

The total power dissipated near the barrier is

$$P = IV = I^2/G = \frac{\partial E}{\partial t} \tag{5.19}$$

Assume the modes are uniformly populated up to some maximum wave vector q_m which is found by equating

$$\hbar\omega_{q_m} = \hbar v_o q_m = E_{fl} - E_{fr} = qV_{sd} \tag{5.20}$$

where E_{fl} and E_{fr} are the Fermi energies on the left and right sides due to the applied bias associated with the current source. Assuming this model, the total power is given by

$$P = \int_0^{q_m} dq \hbar\omega_q \Gamma_q \tag{5.21}$$

If Γ_q is constant up to q_m, then

$$P = \frac{\hbar v_o q_m^2 \Gamma_q}{2} \tag{5.22}$$

or

$$\Gamma_q = \frac{2P}{\hbar v_o q_m^2} \tag{5.23}$$

Using the results from above, assume that the dot center is located a mean distance R from the center of the region where maximum power dissipation occurs in the drain of the QPC. Assume that the phonon population across the dot is roughly equal to the population at this average position. The average acoustic phonon density in the dot is therefore

$$\overline{n}_q(R) = \frac{1}{2\pi v_o R}\Gamma_q = \frac{1}{2\pi v_o R}\frac{2P}{\hbar v_o q_m^2} = \frac{P}{\pi \hbar v_o^2 R q_m^2} \tag{5.24}$$

Since this is the average number of phonons per unit area in the dot, the total number of phonons is just the dot area times this quantity, $A_d\overline{n}_q(R)$. The average energy due to these additional phonons is therefore

$$\langle E\rangle = A\int_0^{q_m} dq\hbar\omega_q\overline{n}_q(R) = \frac{A_dP}{\pi\hbar v_o^2 Rq_m^2}\frac{\hbar v_o q_m^2}{2} = \frac{A_dP}{2\pi v_o R} \tag{5.25}$$

The average energy associated with a Bose-Einstein distribution of phonons at a characteristic temperature T is

$$\langle E\rangle_{eq} = \frac{(k_bT)^4\,3\xi\,(4)}{\pi^2\hbar^3v_o^3}V_d \tag{5.26}$$

in which $V_d = A_d\overline{x}$ is the volume of the dot, where $\overline{x}$ is the average thickness of the 2DEG. Equating Eq. 11 with Eq. 12 and solving for T

$$\frac{A_dP}{2\pi v_oR} = \frac{(k_bT)^4\,3\xi\,(4)}{\pi^2\hbar^3v_o^3}V_d \tag{5.27}$$

$$k_bT = \left(\frac{A_dP}{2\pi v_oR}\frac{\pi^2\hbar^3v_o^3}{3\xi\,(4)}\right)^{1/4} = \left(\frac{A_dP}{2\pi v_oR}\frac{\pi^2\hbar^3v_o^3}{3\xi\,(4)\,V_d}\right)^{1/4} \tag{5.28}$$

or

$$k_bT = \left(\frac{P\pi\hbar^3v_o^2}{6\xi\,(4)\,\overline{x}R}\right)^{1/4} \tag{5.29}$$

Using this model approximate effective temperatures can be calculated for the lattice under the dot. A plot of the effective phonon temperature under the dot as a function of 1D channel current is shown in Fig. 5.20 The lattice temperatures calculated above could certainly produce peak broadening as evidenced from other experiments in the literature (see Ref. [46, 47]). The theory derived above may overestimate the heating under the dot due to the assumptions that all energy is dissipated to the lattice near the dot in the 2DEG and flows uniformly in every direction. In fact, the quantization in the z direction (growth direction as discussed in Chapter 2) will reduce the dissipation in the 2DEG. [143], and there is experimental work on phonon focusing which indicates that the phonons to not radiate uniformly through the lattice [144].

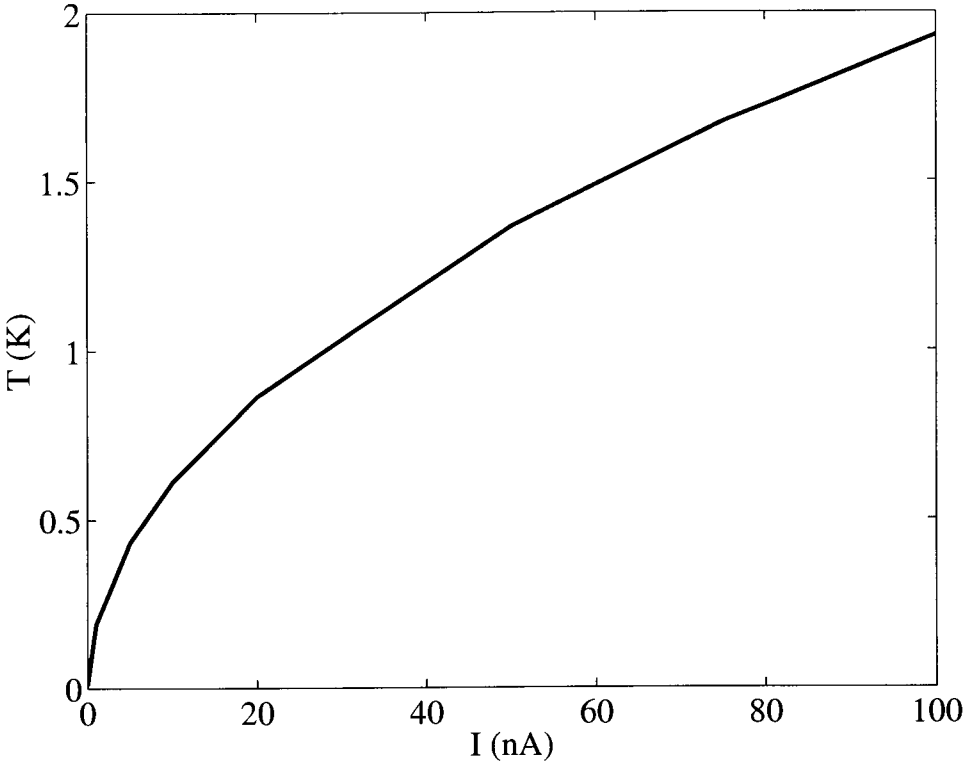

Figure 5.20: Estimated lattice temperature under the dot as a function of 1D channel current

5.4.5 Estimate of Inelastic Scattering Time

An inelastic scattering time (the time over which an electron wave retains its phase coherence) can be estimated by fitting the Coulomb blockade peaks with a Breit-Wigner formula. In Chapter 4, an example of a fit for one peak was given. If inelastic scattering is included, the expression for the transmission becomes,

$$T(E) = \frac{\Gamma_n}{\Gamma_T} \frac{{\Gamma_T}^2/4}{{\Gamma_T}^2/4 + (E - E_n)^2}, \tag{5.30}$$

where $\Gamma_T = \Gamma_n + \Gamma_i$. Γ_{in} is related to the inelastic lifetime or phase breaking time, $\Gamma_{in} = \hbar/\tau_{in}$. A plot of the inelastic scattering time obtained using this formula to fit the CB peaks is shown in Fig. 5.21. These times are in a reasonable range for phase breaking times compared to other experimental estimates in the literature [145]–[147]. In the literature, phase breaking times estimated from experiments vary

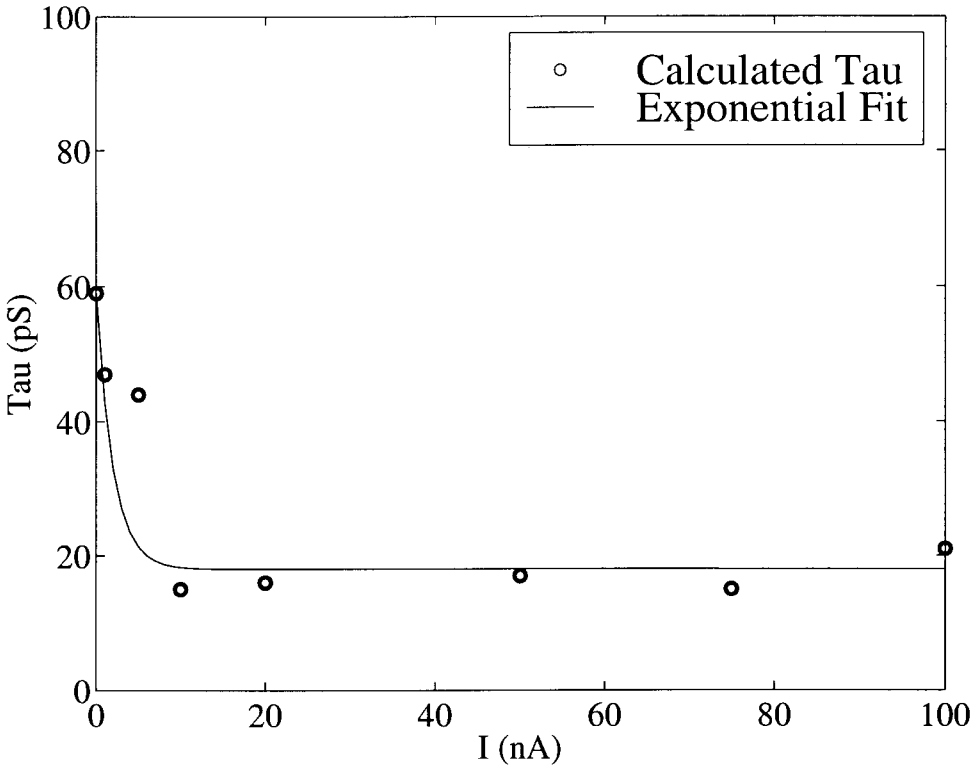

Figure 5.21: Estimated inelastic scattering time as a function of 1D channel current.

linearly with the inverse of the temperature in the range 100 mK to 1 K. In the data presented here, the inelastic scattering time in the dot decays exponentially with current bias in the QPC as,

$$\tau_\phi = A + Bexp^{-I/I_o}, \tag{5.31}$$

where $I_o = 2\,nA$, indicating that the peak broadening may not be due to phonon heating.

5.5 Summary and Conclusions

Nonequilibrium electron transport was explored in single quantum dots and in a coupled QPC and quantum dot system. A knee was observed in the I-V characteristics of the single quantum dots and was controlled by certain gate biasing

which points to electron heating as a physical cause of the knee feature. However, the hot electron model does not fit the experimental data accurately around the knee region. The model does not include ballistic transport, tunneling current, and confinement above the barriers which may account for the discrepancies. Other assumptions in the model may not apply to the devices studied here and a new model is needed to describe the data.

In the coupled QPC and quantum dot system on sample G1135B, the conductance peaks of the quantum dot were broadened as the current was increased in the 1D channel formed by the QPC. A simple ballistic phonon model can account for electron heating in the dot, but may overestimate the actual amount of heating. Inelastic scattering or phase breaking times can be estimated by fitting the peaks with a Breit-Wigner formula. Phase breaking times derived from other experiments in the literature are in the same range and point to a possible Coulomb interaction. More detailed numerical calculations would be needed to ascertain the dominant scattering mechanism.

6. CONCLUSIONS AND FUTURE WORK

6.1 Conclusions

Perhaps the most apparent conclusion from the research pursued in this dissertation is the need for very pure material as the foundation for any experiments into low dimensional AlGaAs/GaAs systems. The material characteristics which successful experiments have in common are high electron mobility ($> 500,000\, cm^2/Vs$), a 2D electron density between 2 and $4 \times 10^{11}\, cm^{-2}$, and a surface to 2DEG distance of less than 1000 Å. In addition, most successful experiments have been performed with MBE grown heterostructure material. The more of these specifications that are met, the more chance the experimentalist has at success. Even when these specifications are met, processing of the material must be done with great care to obtain working devices. Optical lithographically defined S/D contacts must be stable at the millikelvin temperatures required for these experiments, and high resolution e-beam lithography must be used to fabricate the submicron structures. Finally, once the material and processing requirements are met, the chance of obtaining a working device may still be limited by the unique impurity profile of a particular sample or piece of material and any local potential fluctuations near the device due to this unique profile.

The work completed in this research can be divided into two main areas based on the type of transport investigated: near equilibrium and nonequilibrium. The present research covered nonequilibrium transport in single quantum dots and both near equilibrium and nonequilibrium transport in coupled QPC and quantum dot systems.

6.1.1 Near Equilibrium

Near equilibrium magnetotransport experiments on a coupled quantum dot and QPC revealed two novel effects. Aharonov-Bohm oscillations in a quantum dot were detected by the adjacent QPC. As the transmission through the dot varies with magnetic field, the potential on the dot fluctuates, and this potential change can be detected by a change in resistance in the QPC. As far as we know this is the first indirect observation of the A-B oscillations using a quantum dot and a QPC system. In addition, unusual switching behavior was observed in the QPC detector under certain dot gate bias and magnetic fields. Time dependent observations revealed a random telegraph type of signal which is commonly believed to be due to charging of a single impurity in or near the device. It was hypothesized that at a certain self-consistent potential produced by both gate biasing and magnetic field, the charging of an impurity is induced. Switching seems to occur at certain hall plateaus. This phenomena may be due to the fact that on a hall plateau only localized states are available for transport, and an impurity becomes a dominant mechanism of transport through its charging and discharging. Alternately, switching may be due to tunneling between edge states.

6.1.2 Nonequilibrium

Nonequilibrium measurements on single dots were performed to investigate effects of electron heating on the I-V characteristics. SNDC seen previously by Wu *et al.* in a quantum dot with an overlapping gate structure was not seen in the dots studied here which did *not* have an overlapping gate structure. Deviations from the nonlinear behavior predicted by the Landauer-Büttikker theory for a QPC were seen in the I-V characteristics of the dots. The observations of a knee feature in the I-V curves was controlled by gate biasing and in one dot was enhanced by a magnetic field. The energy balance hot electron model proposed by Goodnick *et al.*

can model the turn on voltage and final slope if the I-V curves, but not the position in current of the knee feature. This discrepancy may be due to the omission of ballistic transport and tunneling current in the model. In addition, other classical assumptions may be inaccurate in these small devices with only 100 electrons.

The effect of nonequilibrium transport through a QPC detector on the near equilibrium conductance peaks of an adjacent quantum dot were investigated. To our knowledge, this was the first attempt to observe the Coulomb interaction between a 1D and 0D system. An increase in current through the QPC caused a broadening of the conductance peaks of the quantum dot. A straightforward ballistic phonon theory can account for peak broadening due to thermal effectd. Reduction of the phase coherence time due to a Coulomb interaction may also explain the broadening and can be estimated using a Breit-Wigner fit to the data.

6.2 Future Work

Although much experimental work has been done on near equilibrium transport in single QPC and single quantum dot systems, many possibilities exist for future work on electron transport in coupled systems and under nonequilibrium conditions. It is important to understand electron transport under these regimes if devices are to be used in integrated and high speed applications in the future.

6.2.1 Near Equilibrium

The near equilibrium magnetoconductance experiments may be very difficult to repeat if they are due to a local potential landscape. However, if the impurity effects can be confirmed and arrays of coupled systems could be formed on chips, they may be used to map the impurity potential profile of a piece of material. More investigation is needed on very pure samples to reduce the likelihood of impurity effects and determine whether the switching is due to tunneling between edge states

in the dot. Very recently, a single electron transistor fabricated on the surface of a 2DEG heterostructure was used to probe the edge states of the 2DEG in the quantum Hall regime [155]. Perhaps similar measurements could be made in the coupled quantum dot and QPC system to determine the effect of edge states in the dot on the conductance of the QPC.

6.2.2 Nonequilibrium

Further exploration of hot electron effects would require comparison of dots of different sizes and geometries all fabricated on the same material. In addition, a one to one comparison of the overlapping and nonoverlapping gate structure would be helpful. Modifications to the existing hot electron model or a completely new model based on a different physical mechanism may prove to be a more accurate representation of the I-V characteristics observed. Another possible physical mechanism for the knee feature may be a resonant tunneling phenomena. A resonant tunneling model for a nonequilibrium dot could be adapted from existing theories.

To investigate the mechanism of peak broadening observed in a 1D-0D experiment, a three pronged approach would help to garner the most information: experiments with the existing device geometry, numerical modeling, and experiments with different device geometries. With the existing device geometry a check of the effects of direct lattice heating on the conductance peaks could shed light on the mechanism at work. If the effect is very similar to that observed, this might indicate phonon heating as the cause of peak broadening. Applying a magnetic field should alter the phonon emission rate and may provide additional information. In addition, more accurate numerical modeling is needed to compare the experimental data to the theory. However, what may prove to be even more insightful is to create devices with different spacing between the dot and QPC and to determine the dependence of the effect on distance and lattice direction, as phonon and Coulomb

effects will have different dependences on distance and direction. Finally, better fabrication techniques may be needed in order to produce more closely spaced coupled systems and increase the strength of the Coulomb interaction.

In general there are still many experiments on coupled low dimensional systems in near equilibrium and nonequilibrium transport which remain to be done. No one has observed a 1D-1D Coulomb interaction. Double quantum well (DQW) systems with nanometer split gates provide a new platform for the study of nanometer interacting systems [88]. The promise of clocking electrons one by one through multiple dots and detecting them noninvasively has not yet been realized in GaAs systems. Silicon continues to be the mainstay of the semiconductor industry. However, due to their unique physical properties, GaAs and related tertiary compounds have important niche applications in real world devices, and are the workhorse for the experimentalist to explore the nanoscale world.

BIBLIOGRAPHY

1. R. S. Muller and T. I. Kamins, *Device Electronics for Integrated Circuits*, J. Wiley and Sons, New York (1986).

2. S. M. Sze, *Physics of Semiconductor Devices*, J. Wiley and Sons, New York (1981).

3. S. Wang, *Fundamentals of Semiconductor Theory and Device Physics*, Prentice-Hall, New Jersey (1989).

4. F. Reif, *Fundamentals of Statistical and Thermal Physics*, McGraw-Hill Inc., New York (1965).

5. C. M. Wolfe, N. Holonyak, Jr., and G. E. Stillman, *Physical Properties of Semiconductors*, Prentice Hall, New Jersey (1989).

6. D. K. Ferry, and S. M. Goodnick, *Transport in Nanostructures*, Cambridge University Press, Cambridge, UK (1997).

7. M. A. Reed, in *Semiconductors and Semimetals*, Vol. 35 (ed. R. K. Willardson, A. C. Beer, and E. R. Weber), Academic Press, San Diego (1992).

8. C. Weisbuch and B. Vinter, *Quantum Semiconductor Structures: Fundamentals and Applications*, Academic Press, San Diego (1991).

9. T. F. Gaylord and K. F. Brennan, "Electron wave optics in semiconductors," *J. Appl. Phys.*, vol. 65, 814 (1989).

10. A. Shnirman and F. Schon, "Quantum measurements performed with a single electron transistor," *Phys. Rev. B*, vol. 57, 15400 (1998).

11. U. Meirav, M. A. Kastner, S.J. Wind, "Single-electron charging and periodic conductance resonances in GaAs nanostructures," *Phys. Rev. Lett.*, vol. 65, 771 (1990).

12. L. P. Kouwenhoven, N. C. van der Vaart, A. T. Johnson, W. Kool, C. J. P. M. Harmans, J. G. Williamson, A. A. M. Staring, and C. T. Foxon, "Single electron charging effects in semiconductor quantum dots," *Z. Phys. B.*, vol. 85, 367 (1991).

13. M. Field, C. G. Smith, M. Pepper, D. A. Ritchie, J. E. F. Frost, G. A. C. Jones, and D. G. Hasko, "Measurement of Coulomb blockade with a noninvasive voltage probe," *Phys. Rev. Lett.*, vol. 70, 1311 (1993).

14. W. Porod, "Modeling quantum-dot cellular automata devices and architectures," *23rd International Conference on the Physics of Semiconductors*, vol. 4, 3251 (1996).

15. I. Amlani, A. O. Orlov, G. L. Snider, C. S. Lent, G. H. Bernstein, "External charge state detection of a double-dot system," *Appl. Phys. Lett.*, vol. 71, 1730 (1997).

16. M. W. Keller, J. M. Martinis, N. M. Zimmerman, and A. H. Steinbach, "Accuracy of electron counting using a 7-junction electron pump," *Appl. Phys. Lett.*, vol. 69, 1804 (1996).

17. A. Palevski, C. P. Umbach, M. Heiblum, "High-grain lateral hot-electron device," *Appl. Phys. Lett.*, vol. 55, 1421 (1989).

18. A. Palevski, M Heiblum, C. P. Umbach, "Electron energy spectroscopy and the observation of ballistic transport of hot electrons in the plane of a 2DEG," *IEEE Trans. Electron Devices*, vol. 36, 2619 (1989).

19. J. Wu, Ph.D. Thesis, "Quantum Interference Phenomena and Novel Switching in split Gate High Electron Mobility Transistors," University of Oregon, 1992.

20. L. Pfeiffer, K. W. West, H. L. Stormer, and K. W. Baldwin, "Electron mobilities exceeding 10^7 cm^2/Vs in modulation doped GaAs," *Appl. Phys. Lett.*, vol. 55, 1888 (1989).

21. C. T. Foxon, J. J. Harris, D. Hilton, J. Hewett, and C. Roberts, "Optimisation of (Al,Ga)As/GaAs two-dimensional electron gas structures for low carrier densities and ultra high mobilities at low temperatues," *Semic. Sci. and Technol.*, vol. 4, 582 (1989).

22. H. C. Chui, B.E. Hammons, N. E. Harff, J. A. Simmons, and M. E. Sherwin, "$2x10^6$ cm^2/Vs electron mobility by metalorganic chemical vapor deposition with tertiarybutylarsine," *Appl. Phys. Lett.*, vol. 68, 208 (1995).

23. S. Datta, *Quantum Phenomena*, Addison-Wesley, Massachussetts (1989).

24. T. Ando, A. B. Fowler, and F. Stern, "Electronic properties of two-dimensional systems," *Rev. Mod. Phys.*, vol. 54, 437 (1982).

25. T. J. Thornton, M. Pepper, H. Ahmed, D. Andrews, and G. J. Davies, "One-dimensional conduction in the 2D-electron gas of a GaAs-AlGaAs heterojunction," *Phys. Rev. Lett.* vol. 56, 1198 (1986).

26. H. van Houten, B. J. van Wees, M. G. J. Heijman, J. P. André, "Submicron conducting channels defined by shallow mesa etch in GaAs-AlGaAs heterojunctions," *Appl. Phys. Lett.*, vol. 49, 1781 (1986).

27. T. J. Thornton, "Ballistic transport in GaAs quantum wires-A short history," *Superlattices and Microstructures*, vol. 23, 601 (1998).

28. Y. Imry, "Physics of mesoscopic systems," *Directions in Cond. Matter Phys.* vol. xiv+252, 101 (1986).

29. B. J. van Wees, H. van Houten, C. W. J. Beenakker, J. G. Williamson, L. P. Kouwenoven, D. van der marcel, and c. T. Foxon, "Quantized conductance of point contacts in a two-dimensional electron gas," *Phys. Rev. Lett.*, vol. 60, 848 (1988).

30. D. A. Wharam, T.J. Thornton, R. Newbury, M. Pepper, H. Ahmed, J. E. F. Frost, D. G. Hasko, D. C. Peacock, D. A. Ritchie, and G. A.C. Jones, "One-dimenional transport and the quantisation of the ballistic resistance," *J. Phys. C: Solid State Phys.*, vol. 21, L209 (1988).

31. D. V. Averin, A. N. Korotkov, and K. K. Likharev, "Theory of single-electron charging of quantum wells and dots," *Phys. Rev. B.*, vol. 44, 6199 (1991).

32. C. W. J. Beenakker, "Theory of Coulomb-blockade oscillations in the conductance of a quantum dot," *Phys. Rev. B*, vol. 44, 1646 (1991).

33. J. D. Jackson, *Classical Electrodynamics*, J. Wiley and Sons, New York (1975).

34. W. R. Smythe, *Static and Dynamic Electricity*, Hemisphere Publishing Co., New York

35. C. Cohen-Tannoudji, B. Diu, and F. Laloë, *Quantum Mechanics*, J. Wiley and Sons, New York (1997).

36. R. E. Prange and S. M. Girvin (eds.), *The Quantum Hall Effect*, Springer-Verlag, New York (1987).

37. K. von Klitzing, G. Dorda, M. Pepper, "New method for high-accuracy determination of the fine-structure constant based on quantized Hall resistance," *Phys. Rev. Lett.*, vol. 45, 494 (1980).

38. K. von Klitzing, "The quantized hall effect," *Rev. Mod. Phys.*, vol. 58, 519 (1986).

39. D. C. Cook, *Electrical Characterization of GaAs Materials and Devices*, J. Wiley and Sons, New York (1989).

40. R. A. Webb, S. Washburn, C. P. Umbach, and R. B. Laibowitz, "Observation of h/e Aharonov-Bohm oscillations in normal-metal rings," *Phys. Rev. Lett.*, vol. 54, 2596, 1985.

41. K. Ishibashi, Y. Takagaki, K. Gamo, S. Namba, S. Ishida, K. Murase, Y. Aoyagi, and M. Kawabe, "Observation of Aharonov-Bohm magnetoresistance oscillations in selectively doped GaAs-AlGaAs submicron structures," *Solid State Commun.*, vol. 64, 573 (1987).

42. P. M. Mankiewich, R. E. Behringer, R. E. Howard, A. M. Chang, T. Y. Chang, B. Chelluri, J. Cunningham, and G. Timp, "Observation of Aharonov-Bohm effect in quasi-one-dimensional GaAs/AlGaAs ring," *J. Vac. Sci.*, vol. B6, 131 (1988).

43. C. J. B. Ford, T. J. Thornton, R. Newbury, M. Pepper, H. Ahmed, C. T. Foxon, J. J. Harris, and C. Roberts, "The Aharonov-Bohm effect in electrostatically defined heterojunction rings," *J. Phys. C*, vol. 21, L325 (1988).

44. B. J. van Wees, L. P. Kouwenhoven, C. J. P. M. Harmans, J. G. Williamson, C. E. Timmering, M. E. I. Broekaart, C. T. Foxon, and J. J. Harris, "Observation of the zero-dimensional states in a one-dimensional electron interferometer," *Phys. Rev. Lett.*, vol. 62, 2523 (1989).

45. M. H. Devoret, H. Grabert, "Introduction to single charge tunneling," in *Single Charge Tunneling: Coulomb Blockade Phenomena in Nanostructures, NATO ASI Series B: Physics*, vol.294 (ed. H. Grabert and M. H. Devoret), Plenum Press, New York (1992).

46. J. H. F. Scott-Thomas, S. B. Field, M. A. Kastner, H. I. Smith, and D. A. Antoniadis, "Conductance oscillations periodic in the density of a one-dimensional electron gas," *Phys. Rev. Lett.*, vol. 69, 583 (1989).

47. U. Meirav, M. A. Kastner, and S. J. Wind, "Single-electron charging and periodic conductance resonances in GaAs nanostructures," *Phys. Rev. Lett.*, vol. 65 771 (1990).

48. L. P. Kouwenhoven, "Single electron charging effects in semiconductor quantum dots," *Z. Phys. B*, vol. 85, 367 (1998).

49. A. A. M. Staring, J. G. Williamson, H. van Houten, C. W. J. Beenakker, L. P. Kouwenhoven, and C. T. Foxon, "Coulomb-blockade oscillations in a quantum dot," *Physica B*, vol. 175, 226 (1991).

50. R. C. Ashoori, H. L. Stormer, J S. Weiner, L N. Pfeiffer, K. W. Baldwin, and K. W. West, "N-electron ground state energies of a quantum dot in magnetic field," *Phys. Rev. Lett.*, vol. 71, 613 (1993).

51. U. Meirav, P. L. McEuen, M. A. Kastner, E. B. Foxman, A. Kumar and S. J. Wind, "Conductance oscillations and transport spectroscopy of a quantum dot," *Z. Phys. B Condensed Matter* vol. 85, 357 (1991).

52. P. L. McEuen, E. B. Foxman, U. Meirav, M. A. Kastner, Yigal Meir, Ned. S. Wingreen, and S. J. Wind., "Transport spectroscopy of a Coulomb island in the quantum hall regime," *Phys. Rev. Lett.*, vol. 66, 1926 (1991).

53. A. T. Johnson, L. P. Kouwenhoven, W. de Jong, N C. van der Vaart, C. J. P. M. Harmans and C. T. Foxon, "Zero-Dimensional States and Single Electron Charging in Quantum Dots," *Phys. Rev. Lett.*, vol. 69, 1592 (1992).

54. E. B. Foxman, P. L. McEuen, U. Meirav, Ned S. Wingreen, Yigal Meir, Paul A. Belk, N. R. Belk, M. A. Kastner, and S. J. Wind, "Effects of quantum levels on transport through a Coulomb island," *Phys. Rev. B*, vol. 47, 10020 (1993).

55. E. Buks, R. Schuster, M. Heiblum, D. Mahalu, V. Umansky, "Dephasing due to which path detector," *Physica B*, vol.249-251, 295 (1998).

56. F. R. Waugh, M. J. Berry, D. J. Mar, R. M. Westervelt, K. L. Campman, and A. C. Gossard, "Single-electron charging in double and triple quantum dots with tunable coupling," *Phys. Rev. Lett.*, vol. 75, 705 (1995).

57. F. R. Waugh, M. J. Berry, C. H. Crouch, C. Livermore, D. J. mar, R. M. Westervelt, K. L. Campman, and A. C. Gossard, "Measuring interactions between tunnel-coupled quantum dots," *Phys. Rev. B* vol. 53, 1413 (1996).

58. L. W. Molenkamp, K. Flensberg, and M. Kemerink, "Scaling of the Coulomb energy due to quantum fluctuations in the charge on a quantum dot," *Phys. Rev. Lett.*, vol. 75, 4282 (1995).

59. N. C. van der Vaart, S. F. Godijn, Y. V. Nazarov, C. J. P. M. Harmans, J. E. Mooij, L. W. Molenkamp, and C. T. Foxon, "Resonant tunneling through two discrete energy states," *Phys. Rev. Lett.*, vol. 74, 4702 (1995).

60. F. Hofmann, T. Heinzel, D. A. Wharam, J. P. Kotthaus, G. Bohm, W. Klein, G. Trankle, and G. Wiemann, "Single electron switching in a parallel quantum dot," *Phys. Rev. B*, vol. 51, 13872 (1995).

61. R. H. Blick, R. J. Haug, J. Weis, D. Pfannkuche, K. von Klitzing, and K. Eberl, "Single electron tunneling through a double quantum dot: the artificial molecule," *Phys. Rev. B*, vol. 53, 7899 (1996).

62. L. P. Kouwenhoven, F. W. J. Hekking, B. J. van Wees, C. J. P. M Harmans, C. E. Timmering, and C. T. Foxon, "Transport through a finite one-dimensional crystal," *Phys. Rev. Lett.*, vol. 65, 361 (1990).

63. R. J. Haug, J. M. Hong, and K. Y. Lee, "Electron transport through one quantum dot and through a string of quantum dots," *Surface Science*, vol. 263, 415 (1992).

64. C. H. Crouch, C. Livermore, R. M. Westervelt, K. L. Campman, and A. C. Gossard, "Coulomb oscillations in partially open quantum dots", *Superlattics and Microstructures*, vol. 20, 377 (1996).

65. N. C. van der Vaart, A. T. Johson, L. P. Kouwenhoven, D. J. Maas, W. de Jong, M. P. de Ruyter van Steveninck, A. van der Enden, C. J. P. M Harmans, and C. T. Foxon, "Charging effects in quantum dots in high magnetic fields," *Physica B*, vol. 189, 99 (1993).

66. C. Pasquier, U. Meirav, F. I. B. Williams, D. C. Glattli, Y. Jin, and B. Etienne, "Quantum limitation on Coulomb blockade observed in a 2D electron system," *Phys. Rev. Lett.*, vol. 70, 69 (1993).

67. A. S. Adourian C. Livermore, R. M. Westervelt, K. L. Campman, and A. C. Gossard, "Single electron charging in parallel coupled quantum dots," *Superlattics and Microstructures*, vol. 20, 411 (1996).

68. C. H. Crouch, C. Livermore, F. R. Waugh, R. M. Westervelt, K. L. Campman, and A. C. Gossard, "Coulomb gap of coupled quantum dots with adjustable interdot tunneling," *Surface-Science*, vol. 361-362, 631 (1996).

69. C. Livermore, C. H. Crouch, R. M. Westervelt, K. L. Campman, and A. C. Gossard, "Conductance peak splittin gin charge polarized coupled quantum dots," *Superlattices and Microstructures*, vol. 20, 633 (1996).

70. C. Livermore, C. H. Crouch, R. M. Westervelt, K. L. Campman, and A. C. Gossard, "The Coulomb blockade in coupled quantum dots," *Science*, vol. 274, 1332 (1996).

71. S. Tarucha, D. G. Austing, T. Honda, R. van der Hage, and L. P. Kouwenhoven, "Atomic-Like Properties of Semiconductor Quantum Dots," *Jpn. J. of Appl. Phys.*, vol. 36, 3917 (1997).

72. L. P. Kouwenhoven, T. H. Oosterkamp, M. W. S. Danoesastro, M. Eto, D. G. Austing, T. Honda, S. Tarucha, "Excitation spectra of circular few-electron quantum dots," *Science*, vol. 278, 1788 (1997).

73. D. R. Stewart, D. Sprinzak, C. M. Marcus, C. I. Duruöz, and J. S. Harris Jr., "Correlations between ground and excited state spectra of a quantum dot," *Science*, vol. 278, 1784 (1997).

74. P. L. McEuen, "Artificial atoms: new boxes for electrons," *Science*, vol. 278, 1729 (1997).

75. J. P. Bird, A. P. Micolich, R. Akis, D. K. Ferry, R. Newbury, R. P. Taylor, D. M. Olatona, R. Wirtz, Y. Ochiai, K. Ishibashi, Y. Aoyagi, and T. Sugano, "The role of electron phase coherence in quantum transport through open ballistic cavities," *Jpn. J. of Appl. Phys*, vol. 36, 3968 (1997).

76. D. K. Ferry, J. P. Bird, R. Akis, D. P. Pivin, Jr., K. M. Connolly, K. Ishibashi, Y. Aoyagi, T. Sugano, and Y. Ochiai, "Quantum transport in single and multiple quantum dots," *Jpn. J. Appl. Phys.*, vol. 36, 3944 (1997).

77. Y. Ochiai, A. W. Widjaja, N. Sasaki, K. Yamamoto, J. P. Bird, K. Ishibashi, Y. Aoyagi, T. Sugano, D. K. Ferry, "Phase breaking of coherent electron waves in dot array systems," *Jpn. J. of Appl. Phys.*, vol. 36, 3971 (1997).

78. H. Linke, J. P. Bird, J. Cooper, P. Omling, Y. Aoyagi, and T. Sugano, "Phase breaking of nonequilibrium electrons in a ballistic quantum dot," *Phys. Rev. B*, vol. 56, 14397 (1997).

79. L. P. Kouwenhoven, N. C. van der Vaart, A. T. Johnson, W. Kool, C. J. P. M. Harmans, J. G. Williamson, A. A. M. Staring, and C. T. Foxon, "Single electron charging effects in semiconductor quantum dots," *Z. Phys. B- Condensed Matter*, vol. 85, 367 (1991).

80. L. P. Kouwenhoven, A. T. Johnson, N. C. van der Vaart, A. van der Enden, C. J. P. M. Harmans, C. T. Foxon, "Quantized current in a quantum dot turnstile," *Z. Phys. B-Condensed Matter*, vol. 85, 381 (1991).

81. D. Dixon, L. P. Kouwenhoven, P. L. McEuen, Y. Nagamune, J. Motohisa, and N. Sakaki, "Influence of energy level alignment on tunneling between coupled quantum dots," *Phys. Rev. B*, vol. 53, 12625 (1996).

82. K. Hess, T. K. Higman, M¿ A. Emanuel, and J. J. Coleman, "New ultrafast switching mechanism in semiconductor heterostructures," *J. Appl. Phys.*, vol. 60, 3775 (1986).

83. A. Palevski, M. Heiblum, C. P. Umbach, C. M. Knoedler, A. N. Broers, and R. H. Koch, "Lateral tunneling, ballistic transport, and spectroscopy in a two-dimensional electron gas," *Phys. Rev. Lett.*, vol. 62, 1776 (1989).

84. J. C. Wu, M. N. Wybourne, C. Berven, S. M. Goodnick, and Doran D. Smith, "Negative differential conductance observed in a lateral double constriction device," *Appl. Phys. Lett.*, vol. 61, 2425 (1992).

85. S. M. Goodnick, J. C. Wu, M. N. Wybourne, and Doran D. Smith, "Hot electron bistability in quantum dot structures," *Phys. Rev. B*, vol. 48, 9150 (1993).

86. C. Berven, "Current controlled negative differential conductance in electron waveguide structures," *Ph. D. Thesis*, University of Oregon (1995).

87. J. C. Smith, "Conductance instabilities in quantum point contacts," *Ph. D. Thesis*, University of Oregon (1997).

88. N. E. Harff, "Electron transport in coupled double quantum wells and wires," *Ph.D. Thesis*, Oregon State University (1997).

89. U. S. Tandon, W. S. Khokle, *Patterning material layers in submicron region*, J. Wiley, New York (1993).

90. L. D. Jackel, R. E. Howard, P. M. Mankiewich, H. G. Craighead, R. W. Epworth, "Beam energy effects in electron beam lithography: The range and intensity of backscattered exposure," *Appl. Phys. lett.*, vol. 45, 698 (1984).

91. K. A. Valiev, *The Physics of Submicron Lithography*, Plenum Press, New York (1992).

92. G. R. Brewer, J. P. Ballantyne, *Electron-beam Technology in Microelectronic Fabrication*, Academic Press, New York (1980).

93. D. Chescoe and P. J. Goodhew, *The Operation of Transmission and Scanning Electron Microscopes: Royal Microscopical Society - Microscopy Handbook*, vol. 20, Oxford University Press, Oxford (1990).

94. M. B. Stern, H. G. Craighead, P. F. Liao, and P. M. Mankiewich, "Fabrication of 20-nm structures in GaAs," *Appl. Phys. Lett.*, vol. 45, 410 (1984).

95. H. van Houten, B. J. van Wees, M. G. J. Heijman, and J. P. Andre, "Submicron conducting channels defined by shallow mesa etch in GaAs-AlGaAs heterojunctions," *Appl. Phys. Lett.*, vol. 49, 1781 (1986).

96. A. Scherer, in *Nanostructure Physics and Fabrication* (ed. M. A. Reed and W. P. Kirk), Academic Press, Boston (1981).

97. A. Scherer, M. L. Roukes, H. G. Craighead, R. M. Ruthen, E. D. Beebe, and J. P. Harbison, "Ultranarrow conducting channels defined in GaAs-AlGaAs by low-energy ion damage," *Appl. Phys. Lett.*, vol. 51, 2133 (1987).

98. E. E. Ehrichs, A. L. de Lozanne in, *Nanostructure Physics and Fabrication* (eds. M. A. Reed and W. P. Kirk), Academic Press, Boston (1981).

99. H. L. Simith, K. Ismail, W. Chu, A Yen, Y. C. Ku, M. L. Schattenburg, and D. A. Antoniadis in, *Nanostructure Physics and Fabrication* (eds. M. A. Reed and W. P. Kirk), Academic Press, Boston (1981).

100. A. N. Broers in, *Nanostructure Physics and Fabrication* (eds. M. A. Reed and W. P. Kirk), Academic Press, Boston (1981).

101. W. Seifert, N. Carlsson, M. Miller, M. E. Pistol, L. Samuelson, L. R. Wallenberg, "In-situ growth of quantum dot structures by the Stranski-Krastanow growth mode," *Progress in Crystal Growth and Characterization of Materials*, vol. 33, 423 (1996).

102. B. R. Bennett, B. V. Shanabrook, P. M. Thibado, L. J. Whitman, R. Magno, "Stranski-krastanov growth of InSb, GaSb, and AlSb on GaAs: structure of wetting layers," *J. Cryst. Growth*, vol. 175-1762, 888 (1997).

103. K. Yoh, T. Saitoh, T. Nakano, "Self-assembled InAs quantum dots and their applications to nanostructure devices grown on GaAs," *Compound Semiconductors 1996*, 829 (1997).

104. M. Tabe, Y. Takahashi, K. Murase, "Fabrication and electrical characteristics of silicon quantum dot devices," *Bull. Res. Inst. Electron. Shizuoka Univ. (Japan)*, vol. 30, 13 (1995).

105. E. Leobandung, L. Guo, Y. Yang, and S. Y. Chou, "Single electron and hole quantum dot transistors operating above 110 K," *J. Vac. Sci. and Technol. B*, vol. 13, 2865 (1995).

106. M. Khoury, A. Gunther, D. P. Pivin Jr., M. J. Rack, and D. K. Ferry, "Fabrication of silicon quantum dot in a MOS structure," *Nanotechnology*, in press.

107. G. J. Dolan, "Offset works for lift-off photoprocessing," *Appl. Phys. Lett.*, vol. 31, 337 (1977).

108. N. Goetz, K. Bluethner, W. Krech, A. Nowack, H. J. Fuchs, E. B. Kley, P. Thieme, T. Wagner, G. Eska, K. Hecker, H. Hegger, "Self-aligned in-line tunnel junctions for single-charge electronics," *Physica B*, vol. 218, 272 (1996).

109. H. Bruckl, R. Rank, H. Vinzelberg, I. Monch, L. Kretz, G. Reiss, "Observation of Coulomb blockade effects in AFM-machined tunnel junctions," *Surf. Interface Anal.*, vol. 25, 611 (1997).

110. W. Chen, H. Ahmed, "Fabrication and physics of 2 nm islands for single electron devices," *J. Vac. Sci. and Technol. B*, vol. 13, 2883 (1995).

111. R. G. Woodham, and H. Ahmed, "Fabrication of atomic-scale metallic microstructures by retarding-field focused ion beams," *J. Vac. Sci. Technol. B*, vol. 12, 3280 (1994).

112. C. Vieu, J. Gierak, Y. Lagadec, A. Bourlange, D. Larigaldie, Z. Wang, J. Flicstein, H. Launois, "Gold nanograins deposited form a liquid metal ion source," *Microelectron. Engin.*, vol. 35, 349 (1997).

113. H. Ahmed, "Single atom scale lithography for single electron devices," *Physica B*, vol. 227, 259 (1996).

114. L. Clarke, M. N. Wybourne, M. Yan, S. X. Cai, L. O. Brown, J. Hutchinson, and J. F. W. Keana, "Fabrication and near-room temperature transport of patterned gold cluster structure," *J. Vac. Sci Technol. B*, vol. 15, 2925 (1997).

115. L. Clarke, M. N. Wybourne, M. Yan, S. X. Cai, and J. F. W. Keana, "Transport in gold cluster structures defined by electron-beam lithography," *Appl. Phys. Lett.*, vol. 71, 617 (1997).

116. A. Kent, *Experimental Low-Temperature Physics*, American Institute of Physics, New York (1993).

117. C. A. Bailey, *Advanced Cryogenics*, Plenum Press, New York (1971).

118. D. S. Betts, *An Introduction to Millikelvin Technology*, Cambridge University Press, New York (1989).

119. E. G. Haanappel and D. van der Marel, "Conductance oscillation in two-dimensional Sharvin point contacts," *Phys. Rev. B*, vol. 39, 5484 (1989).

120. C. S. Chu and R. S. Sorbello, "Effect of impurities on the quantized conductance of narrow channels," *Phys. Rev. B*, vol. 40, 5941 (1989).

121. D. D. Smith, M N. Wybourne, J. C. Wu and L. Fotiadis, "A novel technique for the study of defects using quantum wires," *Solid State Comm.*, vol. 91, 313 (1994).

122. H. A. Fertig and B. I. Halperin, "Transmission coefficient of an electron through a saddle-point potential in a magnetic field," *Phys. Rev. B*, vol. 36, 7969 (1987).

123. W. H. Miller, "Semiclassical Treatment of Multiple Turning-Point Problems-Phase Shifts and Eigenvalues," *J. Chem. Phys.*, vol. 48, 1651 (1968).

124. J. N. L. Conner, "On the analytical description of resonance tunnelling reactions," *Mol. Phys.*, vol. 15, 37 (1968).

125. M. Büttiker, "Quantized transmission of a saddle-point constriction," *Phys. Rev. B*, vol. 41, 7906 (1990).

126. D. Vasileska, Personal Communications concerning the 3D Poission and 1D Schrödinger solver, Arizona State University (1998).

127. M. Stopa, "Quantum dot self-consistent electronic structure and the Coulomb blockade," *Phys. Rev. B*, vol. 54, 13767 (1996).

128. J. H. Davies and I. A. Larkin, "Modeling the patterned two-dimensional electron gas: Electrostatics," *J. Appl. Phys.*, vol. 77, 4504 (1995).

129. Y. Meir, N. S. Wingreen, and P. A. Lee, "Transport through a strongly interacting electron system: theory of periodic conductance oscillations," *Phys. Rev. Lett.* vol. 66, 3048 (1991).

130. D. V. Averin, and Y. V. Nazarov, "Virtual diffusion during quantum tunneling of the electric charge," *Phys. Rev. Lett.*, vol. 65, 2446 (1990).

131. L. I. Glazman and K. A. Matveev, "Residual quantum conductivity under Coulomb blockade conditions," *JETP Lett.*, vol. 51, 484 (1990).

132. G. Breit, and E. Wigner, "Capture of slow neutrons," *Phys. Rev.*, vol. 49, 519 (1936).

133. G. García-Calderón and R. E. Peierls, "Resonant states and their uses," *Nucl. Phys. A*, vol. 265, 443 (1976).

134. R. Akis, D. K. Ferry, and J. P. Bird, "Wave function scarring in open ballistic quantum dots," *Jpn. J. Appl. Phys.*, vol. 36, 3981 (1997).

135. C. Dekker, A. J. Scholten, F. Liefrink, R. Eppenga, H. van Houten, and C. T. Foxon, "Spontaneous resistance switching and low-frequency noise in quantum point contacts," *Phys. Rev. Lett.*, vol. 66, 2148 (1991).

136. G. Timp, R. E. Behringer, and J. E. Cunningham, "Suppression of impurity scattering in a one-dimensional wire," *Phys. Rev. B*, vol. 42, 9259 (1990).

137. R. P. Taylor, S. Fortin, A. S. Sachrajda, J. A. Adams, M. Fallahi, M. Davies, P. T. Coleridge, and P. Zawadzki, "Low-frequency noise in multiple-quantum-point-contact systems," *Phys. Rev. B*, vol. 45, 9149 (1992).

138. N. C. van der Vaart, M. P. de Ruyter van Steveninck, L. P. Kouwenhoven, A. T. Johnson, Y. Z. Nazarov, and C. J. P. M. Harmans, "Time-resolved tunneling of single electrons between Landau levels in a quantum dot," *Phys. Rev. Lett.*, vol. 73, 320 (1994).

139. J. P. Bird, K. Ishibashi, M. Stopa, Y. Aoyagi, and T. Sugano, "Coulomb blockade of the Aharonov-Bohm effect in $GaAs/Al_xGa_{1-x}As$ quantum dots," *Phys. Rev. B*, vol. 50, 14983 (1994).

140. S. M. Goodnick, Personal Communications on the Hot Electron Model and Monte Carlo Simulations, Oregon State University and Arizona State University (1998).

141. P. M. Solomon, P. J. Price, D. J. Frank, and D. C. La Tulipe, "New phenomena in coupled transport between 2D and 3D electron-gas layers," *Phys. Rev. Lett.*, vol. 63, 2508 (1989).

142. T. J. Gramila, J. P. Eisenstein, A. H. MacDonald, L. N. Pfeiffer, and L. W. West, "Mutual friction between parallel two-dimensional electron systems," *Phys. Rev. Lett.*, vol. 66, 1216 (1991).

143. B. K. Ridley, *Electrons and phonons in semiconductor multilayers*, Cambridge University Press, Cambridge, UK (1997).

144. H. Karl, W. Dietsche, A. Fischer, and K. Ploog, "Imaging of the phonon-drag effect in GaAs-AlGaAs Heterostructures," *Phys. Rev. Lett.*, vol. 61, 2360 (1988).

145. J. P. Bird, H. Linke, J. Cooper, A. P. Micolich, D. K. Ferry, R. Akis, Y. Ochiai, R. P. Taylor, R. Newbury, P. Omling, Y. Aoyagi, and T. Sugano, "Phase breaking as a probe of the intrinsic level spectrum of open quantum dots," *Phys. Stat. Sol.*, vol. 204, 314 (1997).

146. J. P. Bird, K. Ishibashi, D. K. Ferry, Y. Ochiai, Y. Aoyagi, and T. Sugano, "Phase breaking in ballistic quantum dots: transition from two- to zero-dimensional behavior," *Phys. Rev. B*, vol. 51, R18037, 1995.

147. R. M. Clarke, I. H. Chan, C. M. Marcus, C. I. Duruoz, J. S. Harris, K. Campman, and A. C. Gossard, "Temperature dependence of phase breaking in ballistic quantum dots," *Phys. Rev. B*, vol. 52, 2656 (1995).

148. P. Mooney, "Deep donor levels (DX Centers) in III-V semiconductors," *J. Appl. Phys.*, vol. 67, R1 (1990).

149. D. J. Chadi and K. J. Chang, "Energetics of DX-center formation in GaAs and $Al_xGa_{1-x}As$ alloys," *Phys. Rev. B*, vol. 39, 10063 (1989).

150. D. J. Chadi and K. J. Chang, "Theory of the atomic and electronic structure of DX centers in GaAs and $Al_xGa_{1-x}As$ alloys," *Phys. Rev. Lett.*, vol. 61, 873 (1988).

151. E. F. Schubert, J. Knecht, and K. Ploog, "Transient and persistent photoconductivity in $n-Al_xGa1-xAs$ and selectively doped $n-Al_xGa1-xAs/GaAs$ heterostructures," *J. Phys. C*, vol. 18, L215 (1985).

152. P. Hohenberg, and W. Kohn, "Inhomogeneous electron gas," *Phys. Rev.*, vol. 136, B864 (1964); W. Kohn and L. J. Sham, "Self-consistent equations including exhange and correlation effects," *Phys. Rev.*, vol. 140, A1133, 1965.

153. L. Hedin and B. I. Lundqvist, "Explicit local exchange-correlation potentials." *J. Phys. C: Solid St. Phys.*, vol. 4, 2064 (1971).

154. M. Chen and W. Porod, "Design of gate-confined quantum-dot structures in the few-electron regime," *J. Appl. Phys.*, vol. 78, 1050 (1995).

155. J. Weis, Y. Y. Wei, and K. v. Klitzing, "Single-electron transistor probes two-dimensional electron system in the quantum Hall regime," *Fourth International Symposium on New Phenomena in Mesoscopic Structures*, Kauai, HI (1998).

APPENDICES

A. DX CENTERS IN III-V COMPOUNDS

In III-V compound semiconductors and heterostructures such as n-type doped AlGaAs/GaAs, the dopant atoms (in this case Si) are substitutional donors because they replace a Ga or an As atom in the lattice. Defect formation occurs when either the donor atom or a nearest neighbor is displace along a bond axis. These defects in the lattice cause lattice distortions which create deep donor levels [148]. These defect centers are believed to be highly localized and negatively charged presenting a repulsive barrier to both electron capture and emission [149]. This theory is confirmed by experimental data concerning the dependence of defect formation on the composition, pressure, and dopant concentration [150]. The reaction can be described by the stoichiometry equation,

$$2d^o \rightarrow d^+ + DX^-, \tag{A.1}$$

where d^o is a neutral substitutional donor (e.g. Si) atom and d^+ is the ionized donor which has given up an electron for capture to the DX^- center.

Two main problems exist as a result of DX^- center formation. These defects can be photoionized and release their electrons,

$$DX^- + h\nu \rightarrow 2e + d^o. \tag{A.2}$$

At cryogenic temperatures where many experiments are performed, electrons do not have enough thermal energy to be recaptured, and the increase in carrier concentration can persist for days or weeks with a very small decay rate. This phenomena is known as persistent photoconductivity [151] and can be undesirable.

Another problem arises if the sample is cooled too quickly, and electrons are not able to equilibrate and be captured by the DX^- centers. In a heterostructure device which is cooled rapidly a high electron concentration of will exist in the mate-

rial between the surface and the 2DEG. Gated devices will have poor characteristics because current will be able to leak through the gate and into the 2DEG.

As mentioned in Chapter 2, DX^- centers become a detriment to device behavior when the mole fraction of Al in the the AlGaAs/GaAs heterostructure exceeds 0.3. A balance must be struck between the defect density and the other desired physical characteristics such as confinement of the 2DEG. Finally, care must be taken to create the right experimental conditions to obtain the desired device behavior.

B. DESCRIPTION OF THE 3D POISSON AND 1D SCHRÖDINGER SOLVER

A description of the 3D Poisson and 1D Schrodinger Solver written by Prof. D. Vasileska at Arizona State University is given below. The general analytical equations are given, the iterative technique is described, and the assumptions and numerical techniques used are briefly addressed.

The Schrödinger equation is

$$\frac{-\hbar^2}{2m}\nabla^2\psi(x) + (\phi_H + \phi_{E-C})\psi(x) = 0. \tag{B.1}$$

where ϕ_H is the Hartree potential and is the solution to the Poisson equation,

$$\nabla^2\phi_H = -\rho/\epsilon, \tag{B.2}$$

and ϕ_{E-C} is the exchange correlation potential and is obtained from the interpolation formula developed by Hedin and Lundqvist [153]. The physical sources of the Hartree potential are electron-electron interactions and ionized impurities.

Initially the 2DEG density is calculated by using the self-consistent 1D Poisson-1D Schrödinger solver in the density-functional formalism [152]. The 1D Schrödinger equation is solved for an initial guess of a flat energy (conduction) band. The Schrödinger equation is solved for the charge density, $|\psi^2| = \rho$. The charge density is put back into the Poisson equation and a new value for the Hartree potential is obtained. This iterative process continues until the difference in the Hartree potential between two successive iterations is less than 10^{-5} V. The energy band profile obtained using this solver for the MBE layer structure used in this research is shown in part a of the figure below, and the depletion of the 2D density as a function of gate voltage is shown in part b of the figure. The gate depletion agrees well with the experimental data to within 200 mV as has been observed in simulations of other devices on GaAs material [126].

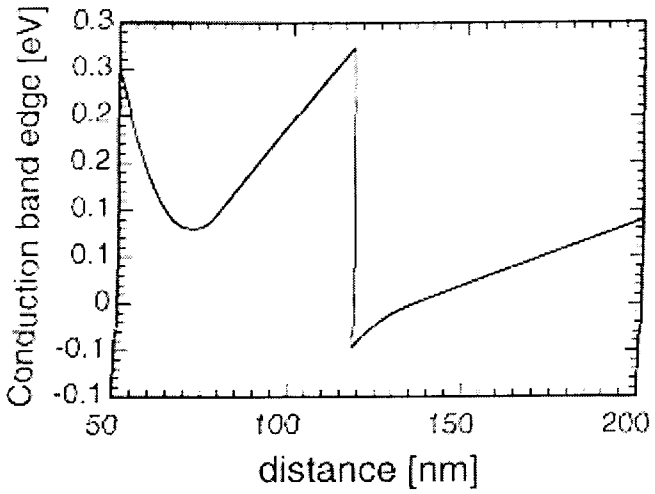
Conduction band edge [eV]
0.3
0.3
0.2
0.2
0.1
0.1
0
-0.1
-0.1
50
100
150
200
distance [nm]

a

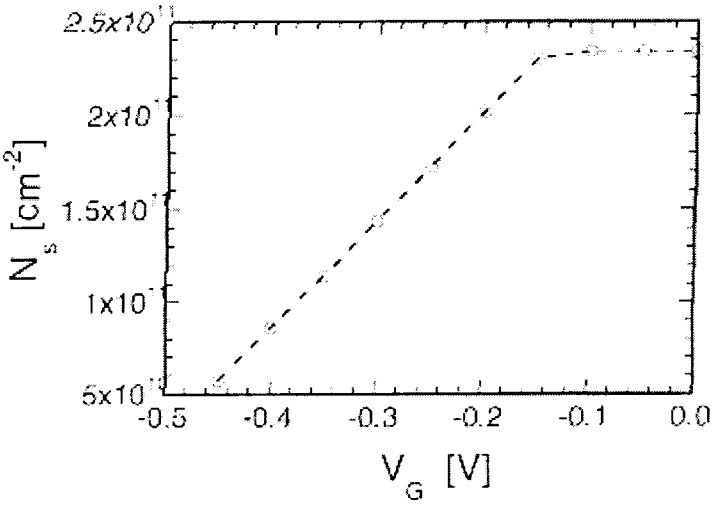
2.5x10
2x10
1.5x10
1x10
5x10
N_s [cm^-2]
-0.5
-0.4
-0.3
-0.2
-0.1
0.0
V_G [V]

b

In the 3D-1D solver there is additional confinement due to the gates. The 3D Poisson equation is discretized, and the 7-point finite difference approximation scheme is used with piecewise constant dielectric constants. The gridding is inhomogeneous to obtain smooth behavior around gate edges and in the QPC constrictions. The boundary conditions used are Dirichlet for the gates and free surface [154] otherwise. In addition, several material parameters must be assumed and are shown in the table below.

Parameter	Value
T	$10\ K$
N_{donors}	$.65 \times 10^{18}\ cm^{-2}$
E_{gap}	$1.4\ eV$
Fraction of Al	.3
Schottky Barrier Height	$.7\ V$
# of occupied subbands	1